Worcester Polytechnic Institute- Department of Chemical Engineering

100 Institute Road, Worcester, MA 01609

Chemical Changes in Hydrothermal Carbon with Reaction Time

A Thesis submitted to the faculty of

WORCESTER POLYTECHNIC INSTITUTE

In partial fulfillment of the requirements for the

Degree of Master of Science in Chemical Engineering

September 7th, 2017

Brendan McKeogh

Professor Michael T. Timko, Ph.D.

Research Advisor

Professor Susan Roberts, Ph.D.

Department Head

Abstract

Hydrochar is the solid product formed from chemical decomposition of organic carbon material in liquid phase water under autogenous pressures, at temperatures of 180-350 °C, over reaction times of several hours. The organic feedstock hydrolyzes, dehydrates, and fragments to form organics, which polymerize and aromatize, forming solid hydrochar as the product. The hydrothermal process is economically appealing for its low-energy requirements and feed-flexibility, accepting a wide variety of low-cost or even waste-stream biomass feedstocks. The process is also appealing for producing relatively benign reaction products. Hydrochar is being actively pursued as a desired product, with possible applications in energy production, soil amendment, and water treatment. While promising, further application of the material is hindered by a fundamental gap in the ability to characterize the structure. Without the ability to characterize the structure, the performance cannot be understood from a chemical standpoint, and any attempts to modify the material will be uninformed and the material cannot be effectively optimized.

The goal of this study was to apply chemical characterization methods to hydrochar to understand the chemical changes with reaction time. These changes with reaction time inform the chemistry of the material and allows for trends in the different characterization techniques to be compared. Ultimately, these methods will be used to connect the chemical characteristics of hydrochar (functional groups, aliphatic content, aromatic content, furan content) to performance in aqueous heavy-metal adsorption. These methods would identify and quantify the chemical characteristics such as carboxylic acid content or aromatic content which are believed to affect aqueous heavy-metal adsorption performance. This would be used in an iterative process of predictively changing the hydrochar processing parameters to give favorable chemical attributes for aqueous heavy-metal adsorption. The hydrochar chemistry would be related to the performance to determine whether the processing conditions created the desired chemical attributes, and whether the desired attributes improved performance

Acknowledgements

As this is an original research project, the vast majority of the work shown was my own, with a few notable exceptions. Measurement of elemental composition of hydrochar via Elemental Analysis was performed by Midwest Microlab Inc. The Gas Sorption measurements of activated carbons were obtained by Avery Brown at WPI (in the Timko Research Group). SEM images were graciously obtained by Dr. Boquan Li at WPI in the Mechanical Engineering Department. AMS data fitting for the generation of mass spectra was done by Dr. Timothy Onasch at Aerodyne Research, Inc. In addition to this, Dr. Onasch designed and assembled the hydrochar aerosol sampling system and the method of operation. The method of operation of was slightly modified to obtain more reliable mass spectra, but the initial methods were developed by Dr. Onasch.

I note here the expertise of others that made this research project possible. Professor Geoffrey Tompsett at WPI (in the Timko Research Group) lent his expertise in the spectroscopic methods, with both the IR and Raman. In the Raman, Prof. Tompsett assisted with the baseline subtraction method and general rules for obtaining good quality spectra. With the Raman Prof. Tompsett provided insight on obtaining reproducible spectra and how to interpret. Dr. Timothy Onasch at Aerodyne Research is an expert on Aerosol mass spectrometry of atmospheric organic aerosols, and is a scientist who helped develop the Soot-Particle Aerosol Mass Spectrometer. He started and configured the instrument when spectra were being collected on a given day, and provided insight into the findings of the study. Professor Michael Timko, the advisor on the project, provided clear assessments on the reproducibility of the data, as well as best practices in data presentation, error analysis, and many other aspects to the project. The Raman fitting assignments were developed by Avery Brown, and he also shared his insight into the Raman effect in carbon materials and what he learned in his literature searches of hydrothermal carbonization and the

Raman of carbon materials. In addition to this, Avery provided feedback on design of experiments and on best organizational habits for the project.

Finally, I'd like to acknowledge the many friends I have made in my time as a graduate student at WPI. The Chemical Engineering Department at WPI is full of hardworking and thoughtful students who were always willing to make time. In no particular order, I'd like to acknowledge my friends Satish Kumar, Behnam Partopour, Lida Namin, Zijan (Jerry) Ma, Yuanpu (Theodore) Wang, Todd Alexander, Lindsay Lozeau, Ivan Ding, Patricia Guerra, Alex Maag, Azadeh Zaker, Maksim Tyufekchiev, and Avery Brown.

Table of Contents

List of Abbreviations and Definitions

5-HMF- 5-Hydroxymethyl Furfural

Adjusted Mass Loading- The mass loading (in ug/m3) attributed to hydrochar in the AMS, that does not include the HO family, the CO ion, and the CO_2 ion.

AMS- Aerosol Mass Spectrometer

EI Ionization- Electron Impact Ionization

IR-ATR- Infrared Attenuated Total Reflectance

DRIFTS- Diffuse Reflectance Infrared Fourier Transform Spectroscopy

DTG- Differential Thermogravimetric Analysis

HR-ToF- High Resolution Time of Flight

HTC- Hydrothermal Carbon

Humins- Hydrothermal carbons prepared with the addition of an acid. Humins are typically prepared from saccharides.

m/z- Mass to Charge Ratio in a ion fragment.

NEXAFS- Near edge X-ray Absorption Fine Structures

SP-AMS- Soot Particle Aerosol Mass Spectrometer

NMR- Nuclear Magnetic Resonance

rBC- Refractory Black Carbon

TGA- Thermogravimetric Analysis

TG-IR- Thermogravimetric Analysis coupled with Infrared Spectroscopy

Total Mass Loading- The mass loading (in $\mu g/m^3$) attributed to hydrochar in the AMS, which is the sum of the Cx, CH, CHO1, CHOgt1, and HO ion family masses.

XPS- X-ray Photoelectron Spectroscopy

List of Figures

List of Tables

Executive Summary

Hydrothermal carbonization offers a new, economical method for synthesis of carbon materials (hydrochars) in high yields. In addition, hydrochar has been shown to have promising performance for a variety of applications, including aqueous heavy-metal adsorption. However, hydrochar is also an amorphous, complex material, hindering reliable characterization using conventional techniques, and creating a reliance on advanced techniques, such as 2D ssNMR. The characterization of hydrochar chemistry is crucial for its development as a material, as development requires intelligent selection of synthesis conditions for optimal application performance. The ability to characterize the chemistry of hydrochar allows for an understanding of the chemical characteristics formed under processing steps and the characteristics that correlate with performance.

In this study, characterization methods were developed for hydrochar and the chemistry of hydrochar was analyzed as a function of reaction time. The characterization methods developed were for IR Spectroscopy, Raman Spectroscopy, and Mass Spectrometry. The methods were also compared against each other to see where they were in agreement and where there were discrepancies. Hydrochars were prepared from a glucose feed (0.41 M aq.) at 180 °C with autogenous pressure, over reaction times of 3-24 hours. Chars were studied ex-situ for all techniques.

For IR Spectroscopy, a careful assessment of the hydrochar, humins, and pyrolysis char literature was conducted to assign IR bands and provide insight into the possible identities for unassignable bands, so they can be identified in the future. The IR spectra of the upper region showed a broad, intense OH stretch, a weak furan C-H stretch, and CH_3 and CH_2 stretches. With reaction time, the CH_3 stretch sharpened.

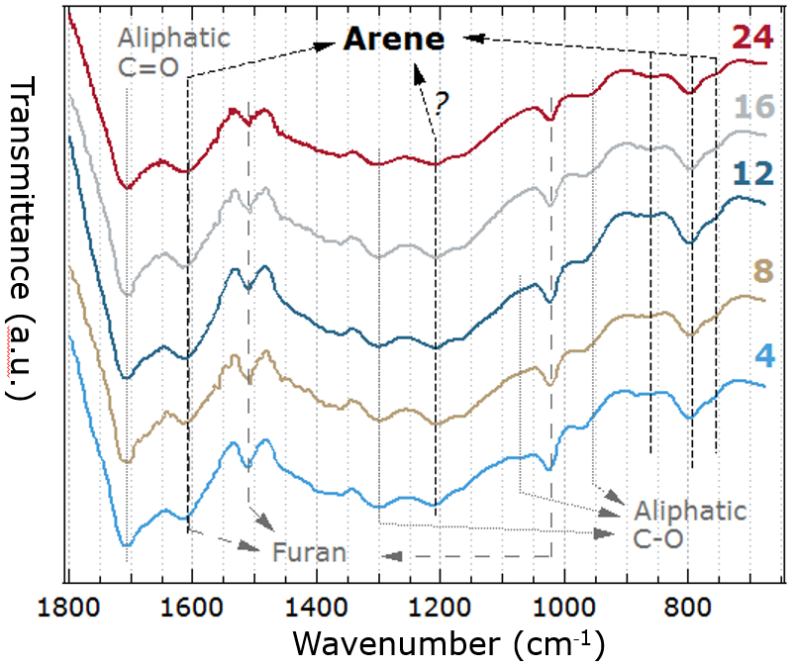

Figure 1. IR spectra of hydrochar with increasing reaction time. IR was obtained via KBr-Transmittance mode. Reaction times (hours) are included next to the corresponding spectra.

The lower IR region 1800-650 cm^{-1} is shown in Figure 1, and identifies aliphatic modes for C-O bonds and the strong C=O stretch at 1700 cm^{-1}. The IR also identifies furan with the peaks at 1520 and 1030 cm^{-1} and arenes with the bands at 875-750 cm^{-1}. The furan modes at 1520 and 1030 cm^{-1} and the C-O mode at 1070 cm^{-1} decrease with reaction time, while the aromatic C=C stretch increases with reaction time along with the aromatic out-of-plane modes increase with reaction time. This indicates an increasing methyl content, increasing aromatic content, and decreasing furan and hydroxyl contents.

Raman Spectroscopy was employed to characterize hydrochar, and a major focus of the study was to obtain high quality, reproducible spectra. Further, the Raman assignments from Brown et al. were applied to the hydrochar spectra and the method was expanded to allow for the tracking of peak positions. The Raman spectra is shown in Figure 2, and the sum of the fit peaks agrees well with the Raman spectra.

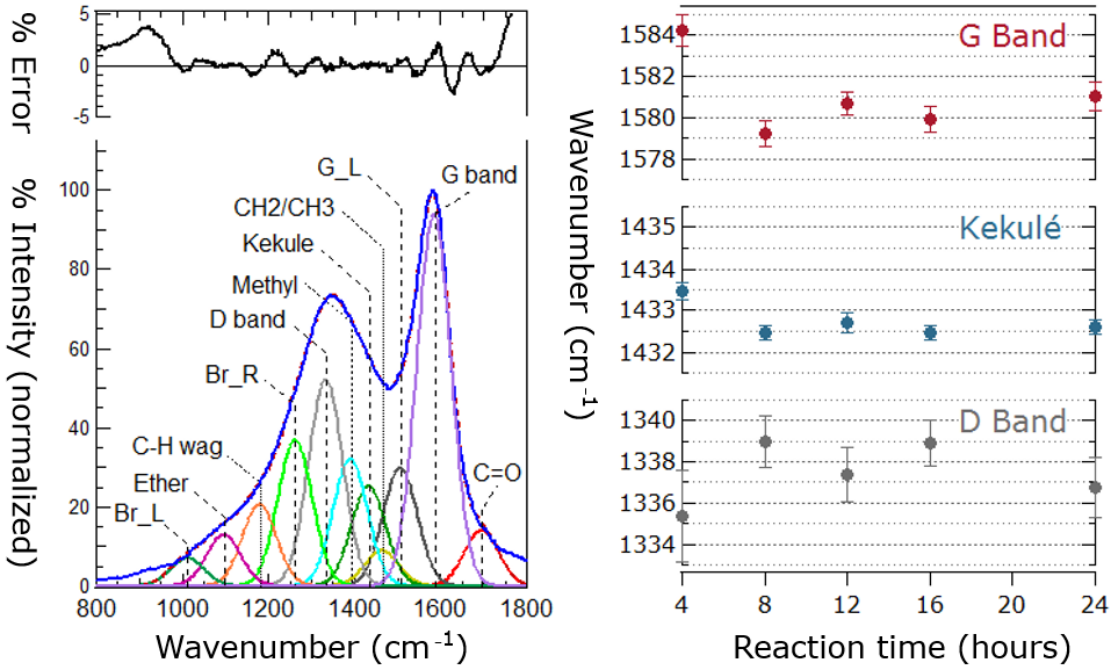

Figure 2. Raman Spectra of hydrochar and changes in parameters with hydrochar synthesis time. Left) Raman spectra of hydrochar, showing fit peaks and the fit spectra (dotted orange line). On the top is the error (difference between the Raman spectra and the fit spectra). Right) Changes in the G band, Kekulé, and D band position with reaction time. Only these three bands were allowed to vary in position when fitting, and were fit one at a time, in that order.

The changes in band positions are also shown in Figure 2, which show decreasing G band and Kekulé position and increasing D band position. Further, the D/G and Kekulé/G fit area ratios were plotted with reaction time. The fit parameters values and trends were analyzed using the molecular modeling of furans and aromatics in the Brown et al. The Raman spectra of hydrochar indicates the presence of aldehyde-functionalized 1-ring and 2-ring arenes, along with some aldehyde-functionalized single-ring furan content. With reaction time, the trends indicate increasing amounts of 2-ring arenes relative to 1-ring arenes.

The Mass Spectrometry technique was applied for the analysis of hydrochars for the first time, using the Soot Particle Aerosol Mass Spectrometer (SP-AMS, Aerodyne Research Inc.) which is designed for studying atmospheric soot particles. A method was developed and established to be reproducible for characterizing changes in the hydrochar mass spectra. The mass spectra of hydrochar is shown in Figure

3. The CH ions (contain carbon and hydrogen) contain peaks for methyl groups and little aliphatic content, olefin chain content, and 1- and 2-ring aromatics. The CHO1 peaks shows alcohol and ketone groups, furan, and benzofuran. CHOgt1 peaks show furans and aromatic. The trends in the compositions with reaction time indicate increasing aromatic content, decreasing furan content, increasing methyl and ethylene content, and decreasing alcohol content.

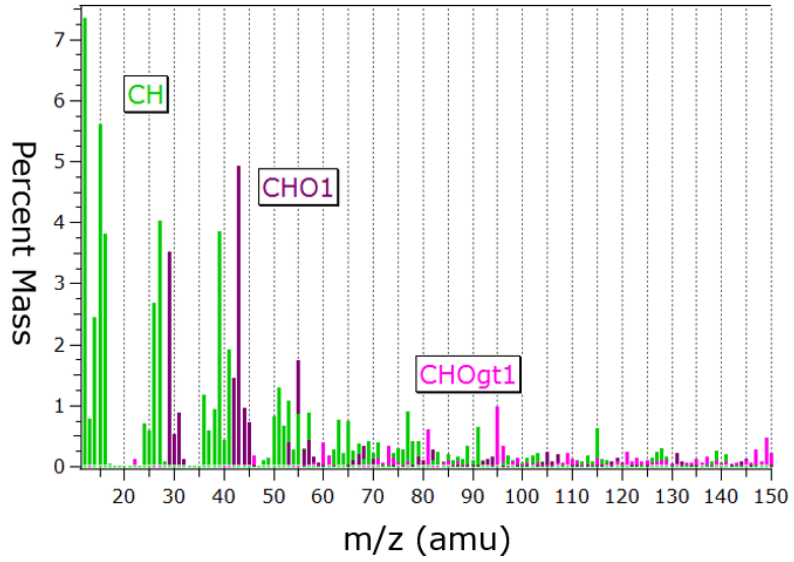

Figure 3. Left) Mass spectra of hydrochar, colored by ion family. Right) Mass ratios of aromatic carbon as a function of reaction time.

The methods developed for the study of hydrochar are consistent with each other, with the IR and Mass Spectrometry techniques showing furans, aromatics, methyl groups, and C-O and C=O functional groups, with the same changes with reaction time. The Mass Spectrometry and Raman Spectroscopy techniques show the same behavior with the increase in aromatic domain size with reaction time. The Mass Spectrometry technique also showed the aromatic content to increase significantly relative to the furan content with reaction time, while the Raman technique did not show such a change.

When combined, these techniques can be used to develop hydrochar for an application, such as heavy metal adsorption. In heavy metal adsorption, the performance depends on the chemical properties of the adsorbent, such as the strength and abundance of acid sites (for binding the metal) and the hydrophilicity

of the material (for allowing the heavy metal to interact with the surface). Acidic functional groups can be assessed with IR and Mass Spectrometry, and the aromatic, furanic, and methyl content can be quantified with Mass Spectrometry to correlate their presence with the adsorption performance and to determine whether intended processing steps gave the desired effect to the chemical composition of the hydrochar.

Introduction

The current environmental problems of climate change, environmental destruction, and population health problems are linked to the ever-increasing consumption of energy on the global scale [1-3]. The main energy sources are coal, natural gas, and petroleum, which release CO_2 gas during coal-fired electricity generation and transportation and industrial consumption [1]. CO_2 is a known greenhouse gas, and contributes to global warming. Climate change, perhaps the most apparent manifestation of energy consumption, threatens ecosystems through the increased frequency and intensity of extreme weather patterns [4] as well as rising global temperatures [2]. Byproducts and pollutants formed during manufacturing processes can also have profound effects on ecosystems as well, with notable cases such as mercury poisoning of ocean fish and birds [5] and BPA exposure to mammals [6]. Through the burning of coal and petroleum, as well as the industrial processes of petroleum processing and chemical production, human health is adversely affected by the proliferation of fine particulate in the atmosphere as well as toxic organics and heavy metals in the drinking water supply [7-10].

The health effects from exposure to industrial waste streams are inherently linked to the feedstocks and the conversion processes in energy generation and chemical synthesis. Coal contains a wide distribution of heavy metals [11] which are known to be harmful to human health [7], while petroleum has toxic organic compounds, among them polycyclic aromatic hydrocarbons [12], thiophenes [13], and benzene [14].

Large-scale processing in power and chemicals productions are also undesirable. These processes rely on large-scale, centralized operations to be profitable, which results in losses associated with the transport of raw materials and finished products alike [15]. Many industrial processes in petrochemical production are highly energy intensive, especially for process heating and separations [16]. Further, petroleum and chemical processes rely on solvents and catalysts, creating additional undesirable chemical waste streams to the environment [17].

A promising approach to addressing these concerns is development and implementation of economical, environmentally friendly, high performance materials. These materials would mitigate the carbon footprint associated with current energy demands, and decrease the proliferation of compounds harmful to the environment and human health. Hydrothermal carbonization of biomass is a promising process for the sustainable production of a carbon material, a material called hydrochar. Hydrothermal carbonization uses liquid phase water at elevated temperatures of about 180-350 °C over time scales of 0.5-48 hours, conditions that cause the feedstock to fragment into smaller compounds which polymerize into the solid product, called hydrochar [18]. The process is appealing for the wide flexibility in the feedstock, such as woody biomass, food processing waste, saccharides and polysaccharides, and manure [19]. Hydrochar is currently being pursued for diverse applications such as energy source [20-21], soil amendment [10, 22], heavy metal absorbent [23-24], bioimaging marker [25], catalyst support material [26-27], gas storage material [28], and electrode [29-31]. The wide variety of applications and reactivity of the hydrochar make it an appealing material for further study and development.

Efforts to fully capitalize on hydrothermal carbon are hindered by a gap in understanding of the chemical composition of hydrochar. The structures and functional groups of the hydrochar determine the applications hydrochar can be used for and they determine how well the material performs. The chemistry of hydrochar and the reactions that occur during hydrochar formation also determine how changes in process conditions affect the final material and its application for a given process. Without knowledge of the structural composition of hydrochar, process conditions for optimal material performance cannot be reasonably pre-determined.

The goal of this project is to develop stronger characterization techniques for hydrochar, with the following objectives:

1. Employ IR Spectroscopy to determine the structures and functionality present in the material. Assign bands based on literature assignments and show how the bands change with reaction time.
2. Develop a method for characterizing hydrochar via Raman Spectroscopy. Establish standards for reproducible Raman spectra collection and application of a Raman fitting method using variable band assignments. Interpret the Raman spectra and the trends in fit parameters with reaction time.
3. Characterize hydrochar with Mass Spectrometry. Establish the reliability of the Soot Particle Aerosol Mass Spectrometer (SP-AMS, Aerodyne Research Inc.) for quantitative analysis of hydrochar. Develop best practices for reliable, reproducible mass spectra from the SP-AMS. Analyze the mass spectra of hydrochar and trends in structurally significant peaks with reaction time.
4. Compare the IR Spectroscopy, Raman Spectroscopy, and Mass Spectrometry results to each other. This informs the sensitivity of the given techniques to certain structural features within the material.

In this study, hydrochars prepared from glucose with varying reaction times are studied by a variety of spectroscopic methods, and these methods are developed to better understand the hydrochar. Glucose, a monosaccharide containing only carbon, hydrogen, and oxygen, is the building block of cellulose, a major component of lignocellulosic biomass and acts a simple model for cellulose. Glucose has been used as a feedstock for hydrochar in previous characterization studies [18, 32-33], and additional studies have been carried out on fructose, its epimer [34-36]. Hydrochars are prepared at 180 °C, a temperature high enough to form hydrochar from glucose [18], but lower than material limits from the Teflon liner. Changes in hydrochar with reaction time are studied ex-situ with reaction times of 3-72 hours. Hydrochars are characterized by Elemental Analysis, IR Spectroscopy, Raman Spectroscopy, and Atomic Mass Spectrometry. Raman

Spectroscopy band assignments from Brown et al.[37] are implemented and a Raman analysis procedure is developed. In addition, Atomic Mass Spectrometry is applied to hydrochar for the first time, and the technique is established in this work and used to analyze the material.

Raman Spectroscopy is a promising technique for hydrochar characterization for its sensitivity to aromatic carbon ordering [38-39]. While Raman Spectroscopy has been used to analyze hydrochar [18, 40-41] the technique is misunderstood, and the Raman spectra has been interpreted with parameters for much more carbonized materials, such as soot or brown coal [42-43]. The Raman spectra of hydrochar and amorphous carbons in the first-order region are dominated by 2 broad overlapping peaks, which are often unfitted or fitted using assignments derived from graphitic materials [43]. Recent work by Brown et al. has offered band assignments for fitting the Raman spectra based of Density Functional Theory calculations of model aromatic and furanic compounds. These assignments are applied to the hydrochar to provide a greater degree of detail on the aromatic character of the material. To complement this technique, IR Spectroscopy is also employed to the hydrochar. IR is sensitive to the oxygen functionality of the material, and can also detect C-H aromatic bonds. Elemental Analysis is applied to hydrochar to quantify the changes in stoichiometry of the hydrochar. Elemental compositions are widely reported in the literature[18, 40, 44-46], and the changes in elemental composition can inform the chemical changes that occur with reaction time.

Mass Spectrometry has a near ubiquitous role in organic chemistry as a method to reliably identify unknown compounds, and is pursued in this study to characterize hydrochar. Mass Spectrometry is a destructive characterization technique that acts by vaporizing and ionizing a chemical sample into molecular ion fragments, then separating the ions by mass to charge ratio (m/z), and measuring the relative masses of the m/z's. The identities, quantities, and relative stoichiometry of the mass to charge peaks indicates the structure and functionality of the hydrochar. This technique has not previously been employed in the study of hydrochar, as most mass spectrometers are not designed to study solids, which require a vaporization as well as ionization. The Soot Particle Aerosol Mass Spectrometer (SP-AMS,

Aerodyne Research Inc.) is one such specialized instrument developed for the characterization of atmospheric carbon particles, with laser and thermal vaporizers that can be run together or separately for the needs of a given carbon type [47]. The AMS is designed for the analysis of atmospheric carbon particles aerosol form before entering the instrument, however hydrochars require aerosolizing before entering the instrument. A self-assembled system was used to aerosolize the hydrochar. This method was established as a reliable method of obtaining reproducible mass spectra.

Mass spectrometry can help to identify the structures present in hydrochar, such as the aromatic and furanic contents and indicate the functional groups present. Further, the technique can be used to quantify changes in ion composition with reaction time, by comparing relative ion compositions of hydrochars prepared at different reaction.

The structure of hydrochar has a clear link to the performance of the material in a real-world application. In adsorption of aqueous heavy-metals, properties such as hydrophilicity affect the ability of adsorbent to interact with the adsorbate, with hydrophobic materials hindering any interaction between the surface and the contaminant. Aromatic carbon is less hydrophobic than aliphatic carbon, for example, and explains why activated carbon is used for heavy-metal adsorption, while a polymer such as polyethylene would be ineffective. Another such chemical attribute may be the presence and density of acidic functional groups, such as carboxylic acids. These groups can interact with the metal ion via charge interactions and bind the metal to the surface. The spectroscopic methods developed in this thesis can identify the chemical composition of hydrochar and quantify changes in the composition for functional groups such as methyl groups (which would decrease the heavy-metal performance), and structures such as aromatics (which would increase the heavy-metal performance).

Background

Hydrothermal Carbon

Hydrothermal Carbonization, as mentioned previously, is a subset of hydrothermal processing, with the reaction conditions set for the formation of a solid product, called hydrochar. The reaction is conducted in liquid phase water under temperatures is the range of 180-350 °C with a reaction time of 4-24 hours, usually under autogenous pressure [18]. The feedstocks tested have been biomass [44, 48-50], biomass subcomponents such as starch, cellulose, hemicellulose, holocellulose, and lignin [45-46, 51-54], and saccharides and sugars such as glucose, xylose, sucrose, etc. [18, 32, 51, 55], and even municipal waste [56-58].

Hydrothermal carbon has been studied to understand how process conditions affect the chemistry and its performance in applications as far reaching and diverse as energy production [20, 59], bioimaging [25], catalyst support [26] , water treatment [23, 50, 60-61], soil amendment [10, 22, 62], gas storage [28], and electrochemistry [29-31]. This is in part owing to hydrochars high oxygen content, which allows it to be functionalized by a wide variety of techniques [63-64]. While promising, the complexity of the hydrochar synthesis mechanism and the difficulty in characterizing the material hinders a robust, predictive approach.

With the complexity of the synthesis mechanism of hydrochar, it is hardly surprising that the chemical and physical properties of hydrochar are highly dependent on the reaction conditions. Hydrothermal carbon chemical and physical properties have been shown to vary with reaction time [40], operating temperature [18], feedstock concentration [18], feedstock [18, 51], pH control [46], salt or acid or base addition [55, 59], pressure [46], and post treatments by microwave assisted treatment [33, 65], heat treatment [24], ball milling [64], or chemical modification [50, 66], to name a few. While this work indicates the versatility of hydrochar properties and hints at the underlying chemistry, ultimately it is the characterization of the hydrochar that informs the versatility of the technique.

Glucose Decomposition

The reactions glucose undergoes at elevated temperatures in liquid phase water can inform the intermediates and the reactions they undergo during hydrochar formation. The reactions seen are isomerizations, fragmentation reactions via retro-aldol reactions, and dehydration reactions via aldol condensation. The isomerization reactions are Lobry de Bruyn–Alberda van Eckenstein (LBAE) transformations, which are transformations between an aldose and a ketose (Lobry de Bruyn & Alberda van Ekenstein, cited in Srokol 2004)[67]. The most significant LBAE transformation in the reaction network shown in Figure 4 is the isomerization of glucose to fructose (Speck, cited in Kabyemela 1999)[35]. The LBAE transformation from glucose to fructose is significant to understanding glucose decompositions, as the reaction to form fructose is much faster than the reverse (Kabyemela et al. 1997, cited in Kabyemela et al. 1999)[35], and fructose is much more reactive than glucose, according to Kuster and Temmink [68].

A significant product of glucose decomposition is 1,6 anhydroglucose, which forms via a dehydration reaction. In a study of glucose decomposition Kabyemela et al. predicted the rate constant for the dehydration reaction of anhydroglucose from glucose based on a reaction network similar to the one shown in Figure 4, and determined the rate constant to be 10% of the isomerization of glucose to fructose.

Glucose, in its aldose (straight-chain) form fragments into erythrose and glycoladehyde via a retro-aldol mechanism[67]. According to Srokol, erythrose can undergo a retro-aldol reaction to form two glycolaldehydes. In the Srokol et al. study, more glycolaldehyde forms from glucose than 5-HMF at 340 °C. Kabyemela et al. determined the rate constant for the formation of erythrose and glycolaldehyde from glucose to be double the isomerization of glucose to fructose (at 300 °C, assuming all first order kinetics)[35]. The reaction that forms glycolaldehyde and erythrose is base-catalyzed, according to Srokol et al (de Bruijn et al., cited in Srokol et al. 2004)[67].

In Figure 4, an intermediate of glucose and fructose transforms to glyceraldehyde or dihydroxyacetone. According to Srokol et al. glucose isomerizes to mannose, which undergoes retro-aldol reaction to form

dihydroxyacetone and glyceraldehyde, which can interconvert via LBAE transformations [67]. The rate constant for the formation of dihydroxyacetone and glyceraldehyde from glucose and fructose is about the same as that for the glucose to fructose epimerization. In the isomerization between dihydroxyacetone and glyceraldehyde, dihydroxyacetone is the preferred form [67]. Dihydroxyacetone or glyceraldehyde can dehydrate to form pyruvaldehyde [67]. Srokol et al. identified the decomposition products of glyceraldehyde to include glycolic acid, acetic acid, formic acid, lactic acid, and acrylic acid [67].

A significant reaction product of glucose is 5-Hydroxymethyl Furfural or 5-HMF. 5-HMF forms from fructose following three dehydration reactions via an acid-catalyzed reaction mechanism [Antal et al., cited in Srokol et al. 2004] [67]. In the study by Srokol et al., 5-HMF was one of the most significant (on a molar basis) products formed from glucose. Under hydrothermal conditions 5-HMF hydrolyzes and forms levulinic acid and formic acid [69]. Horvat et al. proposed a mechanism of levulinic acid and formic acid from 5-HMF via a cyclic hemiacetal intermediate, 4 hydration steps, and 2 dehydration steps[70]. In a study by Karwa et al., levulinic acid was shown not to react under acidic conditions at high temperatures[71].

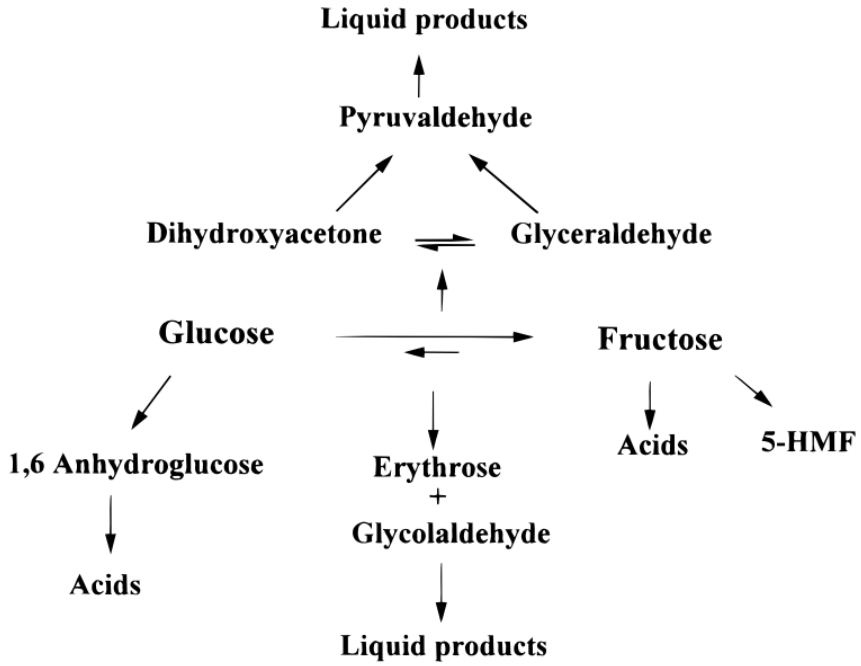

Figure 4. Reaction Network for Glucose, in non-catalyzed subcritical water. Reprinted from Ref. Copyright 1999 American Chemical Society.

HMF is believed to be a major intermediate in the formation of hydrochar and is incorporated into the hydrochar [32, 55, 72-73]. Promdej and Matsumura developed a kinetic model for hydrochar formation and found the rate constant for 5-HMF reaction to hydrochar to be significant under subcritical conditions. Both Latham et al. and Baccile et al. propose that the furan ring from 5-HMF is incorporated into the hydrochar [32, 55].

Patil and Lund suggest that HMF polymerizes and forms hydrochar under acidic conditions by formation of 2,5-dioxo-6-hydroxy-hexanal (DHH), which combines with HMF via aldol addition and aldol condensation reactions. Patil and Lund note that DHH could not be detected and state that this could be due to its high reactivity/low stability. This type of addition would retain the furan ring and the hydroxyl group of the HMF. In addition, there would also be aldol functionality (ketone conjugated with an olefin group).

During the hydrothermal process other furan compounds are reported to form, such as furfural [44, 55, 73-74], 5-methyl furfural[55], ethyl-5-methyl-furan, 2-Furancarboxaldehyde, 5-(hydroxymethyl)-, Furan, 2-(1-pentenyl)-, (E)-, and 2(3H)-Furanone, 5-ethyldihydro-5-methyl[44]. In the Srokol et al. study, furfural was measured to be a significant decomposition product of glucose, and has about half the molar concentration as 5-HMF[67].

Finally, aromatic compounds are reported to form from glucose in particular 1,2,4 benzenetriol [67], which is believed to form from 5-HMF [Luijkx et al., cited in Srokol et al 2004][67]. 1,2,4 benzenetriol has been suggested to have a role in hydrochar formation, in a study by Schuhmacher et al., hydrochar forms when 1,2,4 benzenetriol is used as the feed[46]. Other aromatic compounds have been reported to form in subcritical hydrothermal conditions, including 1,4 benzenediol [41, 74] and other phenol compounds[74].

Under hydrothermal conditions, glucose readily reacts to form fructose, which readily dehydrates to form 5-HMF. Decomposition products such as glycolaldehyde, 1,6 anhydroglucose, dihydroxyketone, and levulinic acid also form through a combination of LBAE transformations and retro-aldol reactions. Dehydration reactions result in 5-HMF, furfural, and 1,2,4 benzenetriol, which react via aldol reactions to form hydrochar. Aromatic and furanic domains are reported in the hydrochar, and early products of glucose show these functionalities.

pH Stability of Hydrochar

The hydrothermal reactions of glucose are dependent on the pH, with acid-catalyzed reactions (such as HMF formation from fructose) and base-catalyzed reactions (such as glycolaldehyde and erythrose formation from glucose) occurring at the same time. The chemical stability of hydrochar is likewise known to be pH dependent. Naisse et al. [75] studied the stability of hydrochar to acid dichromate (an oxidizing agent) and hydrochloric acid (a strong acid). Under strong HCl conditions (6 Molar), the hydrochar retained about 80-85 % of its initial carbon, the same as gasified carbon (prepared at 1200 °C). By contrast, only 3-12 % of the initial carbon from hydrochar remained after dichromate treatment, compared to 72-85% for gasified carbons. Clearly, hydrochar has significant acid stability, and has little aromatic character that is table against an oxidizing agent. A Temmink and Kuster study on acid-catalyzed hydrochar formation from fructose found hydrochar transitions from insoluble to soluble at a pH of 4, which implies that hydrochar is held together because of its acidic character [68].

Hydrochar Characterization

The characterization of hydrochar as a bulk material (as opposed to work understanding the morphology or surface chemistry) is less understood than perhaps the surface of the material or the morphology or porosity. XRD (X-Ray Diffraction) has been applied to the characterization of hydrochar in a variety of studies [51] , with studies showing a single broad peak, indicating hydrochar has an amorphous structure. Several methods were employed to characterize the material: XPS (a surface technique) [18, 55], FT-IR

Spectroscopy [18, 51], Raman Spectroscopy [18], NMR Spectroscopy [32], and NEXAFS (Near-Edge X-Ray Adsorption near Fine Structures) [76]. In addition to these techniques, Elemental Analysis and EDX (Energy Dispersive X-Ray Spectroscopy) can provide additional quantitative insights in the material that spectroscopy techniques cannot do to the same extent.

In a pioneering study of hydrochars, Schuhmacher et al. prepared hydrochars from glucose and similar compounds to glucose, cellulose, lignin, wood, and peat, varying time, concentration, temperature, pressure, and adding acid, base, or salt to the solution, and observed the change in solid yield, CO_2 formation, and elemental (CHO) composition [46]. In this study, hydrochars were prepared and the change in elemental composition was compared against coal species. From conditions of around 220 °C, 3 hour reaction time, and 20 wt. % feed loading, the carbon content increased with reaction temperature, reaction time, and pressure, increasing from lignin to wood to cellulose, and decreased with concentration. The trends in reaction temperature, time, and feedstock complexity were supported in studies by Sevilla and Fuertes on saccharides and cellulose [18, 54].

Table 1. Typical elemental mass compositions of glucose-derived hydrochars.

Conditions	C	H	O	Ref
Feed: Glucose, T=170 °C, t=4.5 hr	64.9	4.2	30.9	[18]
Feed: Glucose, T=180 °C, t=12 hr	64.5	4.7	30.8	[77]
Feed: Glucose, T=180 °C, t=24 hr	63.7	4.3	32	[24]
Feed: Cellulose, T=225 °C, t=3 hr	71.3	4.6	24.1	[46]
Feed: Sucrose, T=200 °C, t=4 hr	65.73	4.8	28.9	[55]

Energy Dispersive X-Ray Spectroscopy (EDX) is another technique available to measure atomic compositions of both the surface and the bulk. Chen et al. [24] analyzed hydrochar (prepared from glucose at 180 °C) via EDX, obtaining a bulk O/C ratio of 0.32 (technique did not analyze the hydrogen content). This is a lower O/C ratio than Falco et al. [78], who determined a ratio of 0.36 by elemental analysis of glucose derived hydrochar (also prepared at 180 °C), but from a less concentrated sugar solution, so perhaps the results are not so easily comparable, as a less concentrated solution gives a higher carbon content [46 18].

The structure and functionality of hydrochar has been studied in a variety of studies, and it is crucial in the pursuit of better performing materials from the hydrothermal process and from post-processing of the material. Hydrochar chemical characterization techniques have been employed in a variety of spectroscopic tools and from these different conclusions have been drawn about the "structure" of the material [32, 41, 54, 76]. These models identify the types of carbon-backbone structures present (arenic, furanic, aromatic, aliphatic, branched vs. straight chain) and the types of oxygen functionalities and their locations relative to the structure (phenols, lactones, furans, ethers, etc.). These model structures are shown in Figure 5.

In Figure 5a., the structural model of Baccile et al. [32] (here we will refer to as the Titirici and Antonietti model) is shown, which depicts furanic domains, separated by ketone-containing alkyl connecting functions, and with levulinic acid embedded in the structure. The furans are connected by both α-carbons (connected to the oxygen) by methylene bridges, with some functionalities on the β-carbons as well. The Titirici and Antonietti model comes from a study of hydrochar by solid state ^{13}C NMR. Hydrochars were prepared from glucose at 180 °C with a 24 hour reaction time. The NMR spectra detected 2 significant sp^2 peaks at 150 and 110-130 ppm, which were attributed to O-**C**=C and O-C=**C** carbon respectively. This indicates the presence of a furan ring which contains α (O-**C**=C) and β (O-C=**C**) carbon. INEPT (Insensitive nuclei enhanced by polarization transfer) sequence, which is sensitive to protonated carbon, identified

protonated carbon as O-C=**C**, but no protonated O-**C**=C carbon. The α-carbons would therefore not be protonated,

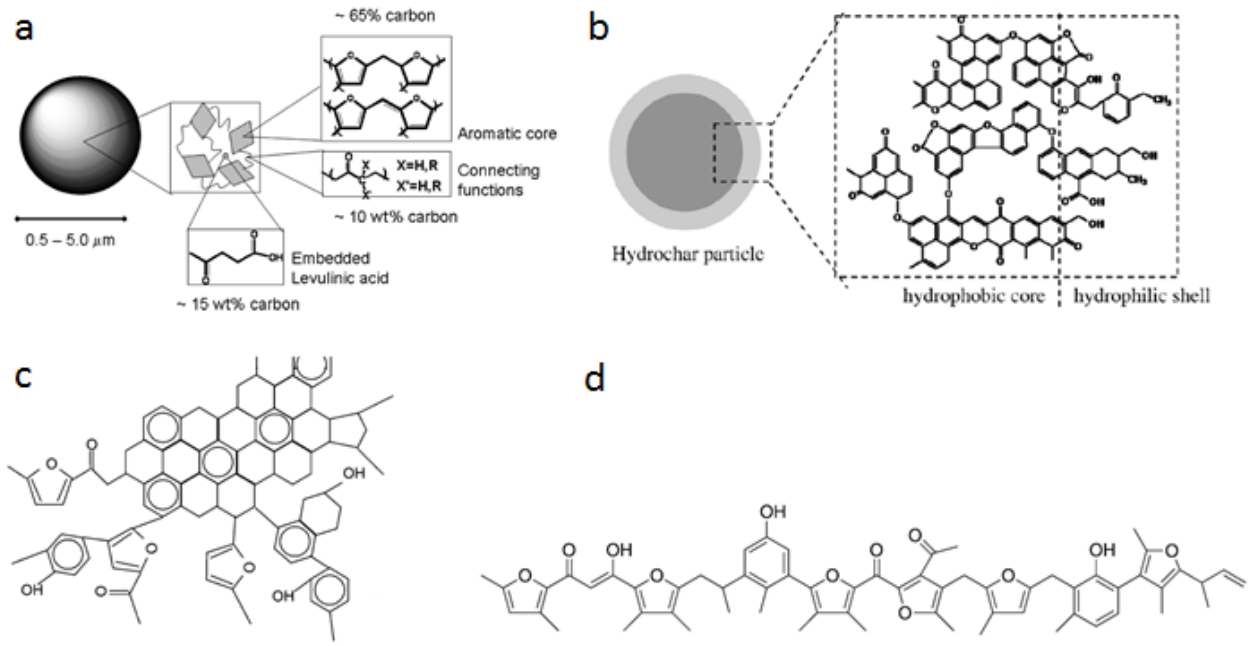

Figure 5. Hydrochar structural models from literature. a) Titirici and Antonietti model. Reprinted (adapted) with permission from Ref. [32]. Copyright 2009 American Chemical Society. b) Sevilla and Fuertes model. Reprinted from [54], Copyright 2009, with permission from Elsevier. c) Chuntanapum and Matsumura model. Reprinted with permission from Ref. [41]. Copyright (2009) American Chemical Society. d) Latham et al. model. Reprinted with permission from Ref. [76]. Copyright 2009 American Chemical Society.

indicating that they are attached to another functionality, while the β-carbons would have hydrogen. The CP method of NMR, which is quantitative, determined the α- and β- carbon to be present at a 1:1 ratio, which is consistent with the stoichiometry of furan.

2-D NMR was also employed in the Baccile et al. study, which provides information about how chemically distinct carbons are linked. For example, if a carbonyl carbon (>**C**=O) were attached to arenic carbon, the peaks for arenic and carbonyl carbon would align in the horizontal direction. Among the strongest cross peak correlations were between the α and β furan peaks, further indicating the presence of furans. The medium strength aromatic carbon peak had a good correlation with itself, which is consistent with aromatic carbon bound to other aromatic carbon. A strong cross correlation was seen between β carbon, which is consistent with the furan structure where β carbons are directly attached. The cross correlations

for C=O carbon were much stronger with aliphatic carbon than sp^2 carbon. NMR indicated that the carbonyl is almost always in ketone form, as opposed to aldehyde or carboxylic acid. The weak relation between the furan peaks and the C=O peaks indicates that a carbonyl peak is not adjacent to the furan ring.

The Baccile et al. study provides key insight into the structure of hydrochar, and comes to important conclusions. Baccile et al. establish the presence of furan as a part of the hydrochar structure, and to a less degree aromatic carbon. The α-carbons on furans are usually attached to a sp3 carbon, while the β carbons are protonated. Alkyl linkages connect the furans together via the α-carbons and contain ketone groups. Free levulinic acid is also embedded within the hydrochar solid.

The structural model of Sevilla and Fuertes is shown in Figure 5Figure 5b, which appears to be small fused polyaromatic clusters consisting of arenes, quinones, and furans, separated by ether linkages and with the carboxyl, hydroxyl, and ketone functionalities on the outside. The model was determined based on characterization by X-Ray Diffraction, X-Ray Photoelectron Spectroscopy (XPS), Raman Spectroscopy, IR Spectroscopy, and Elemental Analysis. X-Ray Diffraction, showed a broad, very weak band in the hydrochar, indicating that the material is amorphous in its structure. Elemental analysis showed a significant amount of dehydration reactions occurring on the cellulose in the formation of the hydrochars, with a small amount of decarboxylation reactions as well. IR Spectroscopy showed the presence of carbonyls (C=O), aromatics (aromatic C-H bonds), aliphatic content (C-H bonds), and C-O groups (ethers, alcohols, esters, carboxylic acids). Raman Spectroscopy showed broad, overlapping G and D bands, which indicate the presence of aromatic carbon clusters and sp^2 carbon. XPS, a technique that characterizes the surface functionality of a material showed the largest signals for CH_x, C-C, and C=C, followed by the C-O, the ketone/aldehyde peak, and the small –COOR peak (ester or carboxylic acid) peak. The composition of the surface functionality decreases in the order C-O > >C=O > COOR. The authors proposed the structural model along with a mechanism, where intermolecular dehydrations and aldol condensations took place.

The Sevilla and Fuertes study results (and model) differ from the Baccile et al. with an identification of alcohol and carboxyl content. Furanic carbon was not stressed either. The techniques employed by Sevilla and Fuertes indicated at functionality present in the material, but unlike the Baccile et al. study the focus was on the effect of reaction conditions on bulk properties than a close characterization of the hydrochar structure.

The Chuntanapum and Matsumura model [41] is shown in Figure 5c which involves fused aromatic rings with 6-membered non aromatic rings at the center and alkyl chains connected to furans, single-ring aromatics, alcohols, and ketones on the outside. Chuntanapum and Matsumura prepared the hydrochar at a much higher temperature than Sevilla and Fuertes or Baccile et al. The solid was analyzed via FT-IR, and Raman spectroscopy. In the study gas and liquid characterization techniques (gc, etc.) showed aromatic and furanic products. The IR of the solid product showed a strong OH stretch, a furan ring CH stretch, and a CH aldehyde stretch. The spectra also showed a significant C=O stretch, a somewhat strong C=C stretch, a significant furan C=C stretch, and an ether stretch was assigned at the band at 1430-1330 cm^{-1}. The Raman spectra was analyzed in a similar manner to the Sevilla and Fuertes study, where the presence of the G and D peaks was interpreted as a sign of aromatic structures.

The last model shown in Figure 5, the Latham model, is a chain-like structure containing furan rings and benzene rings, with methyl branches of the chain and rings, ketone functionalities on the chains, and alcohol groups. The model resulted from a study using NEXAFS and a previous study [55] which characterized hydrochar by Elemental Analysis, IR Spectroscopy, TGA (Thermogravimetric Analysis), and XPS, while the liquid products were analyzed by GC/MS.

The Latham et al. study is characterization of hydrochar formed from sucrose (a disaccharide composed of glucose and fructose) by using NEXAFS (Near-Edge X-Ray Absorption Fine Structure Fluorescence Spectroscopy) to characterize the hydrochar surface. NEXAFS uses high energy x-rays from a synchrotron

source to excite an electron in the 1s core energy level to the π* and σ* orbitals. The transition energy depends on the element, the bond types, and the functionality of the bond. The NEXAFS spectra was deconvoluted by assigning peaks based on the positions of peaks in the NEXAFS spectra of model compounds, and cross-checked with literature assignments.

The first peak corresponds to C=C 1s → π*, although it did not fit exactly with the fits for alkenes or benzene, anthracene, phenol, or terphenyl, which indicates multiple structure that contribute to the position. The benzene peak was located between two fit peaks, indicating that benzene is not a strong part of the structure. Peaks fit at 285.9 and 286.5 eV correspond to the β- and α-carbons in furan respectively, which is supported by fit peaks at 292.4 eV and 298-299 for C-C/C-O and C=C. A peak at 288.2 eV corresponds to carboxylic acids, while 289.3 eV is attributed to alkyl/aromatic OH. The C-H bonds are seen in the aliphatic domains, the same place with the OH functionalities.

The NEXAFS technique in the Latham et al. study indicates that furanic moieties are overrepresented compared to aromatic ones in the structure of hydrochar, in support of the conclusions in the NMR technique used by Baccile et al. The technique indicates carboxylic acid and alcohol functionality are present in the structure.

The studies shown indicate that there is some discrepancies and uncertainties in the structure and functionality of hydrochar and the interpretation of the spectroscopic methods. The aromatic content is not well understood either. One area that deserves additional scrutiny is the Raman spectra of hydrochar and how it is interpreted. The presence of the D band is generally assumed to mean that the hydrochar has polyaromatic domains, when the NMR and NEXAFS studies indicate that these groups are not significant compared to the furanic domains [32, 76]. One study that illustrated the point well was the study of Sevilla and Fuertes [54], where a hydrochar Raman spectra was compared to the same material, pyrolyzed at 800 °C, both spectra showing similar D and G peaks, with only a slight change with carbonization. In the

study of Chuntanapum and Matsumura [41], the Raman of the char showed higher signal intensity (or lower fluorescence) in the hydrochar that was recovered at shorter reaction times, as opposed to the material taken at 4 times the reaction. These effects were not explained, and it only further shows that the Raman of hydrochar is not well understood. According to Ferrari and Robertson, the G and D peaks are seen widely in carbon material, even those not known to be graphitic [38]. This highlights the need to understand Raman Spectroscopy in amorphous carbon materials.

The functionality of the hydrochar material also seems to be poorly understood. XPS and IR spectroscopy indicate the presence of significant hydroxyl functionality, with ether functionality also shown through IR, and the distinction of carboxylic acids as well as ketone functionalities has been made through XPS. NMR, it was acknowledged, wasn't very effective at determining the present of C-O bonds, while NEXAFS did not conclude anything significant on the C-O content besides the furanic ether. Other questions such as the presence of methyl groups or aldols, enols, phenols, or quinones remain.

IR Spectroscopy

Infrared absorbance spectroscopy measures a sample's absorbance of infrared light as a function of the frequency. Most of the vibrational modes in organic chemistry can be detected in the infrared region, so this method is commonly used to determine the chemical bonds and functional groups present in a given material [79], and has been used routinely to characterize a wide variety of compounds, including very complex materials such as petroleum residue [80] and lignocellulosic biomass [81]. Correctly assigning vibrational bands in a spectra for a complex, amorphous material is however, a daunting task. To understand the spectra that may appear in hydrochar, it is useful to assess the assignments in other, related materials. Here, hydrochar is derived from glucose, a model for biomass, and IR assignments from other saccharide-derived hydrochars and whole biomass would be of primary influence. The changes in the IR spectra of whole biomass with hydrothermal treatment can be studied, which can shed light on the types of bands that are and are not expected to exist in a hydrochar prepared from a similar material.

In the characterization studies of hydrochar that employed IR Spectroscopy, assignment were made for several functional group types without disagreement. The hydrochar spectra assignments included OH stretch (3300 cm^{-1}), CH stretches (2950 cm^{-1}), C=O stretch (1700 cm^{-1}), C=C stretch (1600 cm^{-1}), and C-H wag modes (875-750 cm^{-1}) [18, 41, 54-55, 82]. Other band assignments, and more descriptive interpretations of the bands varied.

Latham et al. attributed the C=C stretch at 1600 cm^{-1} to aromatic carbon [55], however van Zandvoort et al., in a study of hydrochar prepared under acidic conditions (hydrochars called humins) interpreted the C=C stretch as a furanic mode [83]. The van Zandvoort et al. assignment, unlike the Latham et al. one, affirmed the conclusion by the shift in position for the ^{13}C labeled sample.

Patil et al. studied humins prepared from glucose, fructose, and 5-HMF, and compared the IR spectra of the humins with HMF [84]. Significant HMF peaks at 1510 and 1030 cm^{-1} were weaker in the HMF-derived humins, and were weaker in the spectrum of the glucose-derived humins. Since the conversion of HMF to hydrochar is expected to incorporate the furan ring and hydroxymethyl group, while glucose is not expected to incorporate as much HMF into the humins, the peaks at 1525 and 1030 cm^{-1} are interpreted to come from the furan ring or hydroxymethyl group of HMF [82].

Van Zandvoort et al. measured the shift in position of the C=O stretch using a ^{13}C enriched humin, and determined that the 60 cm^{-1} shift indicated enone chemistry [83]. However, the authors noted that peak broadening occurred which indicated other types of functionality present.

The ether stretch in particular has also been difficult to find consensus, with assignments at 1460-1000 cm^{-1} [18, 54] 1150 cm^{-1} [40], 1030 cm^{-1} [64], and at 1250 cm^{-1} for an ether linkage between two aromatic rings [85].

Ishimaru et al. studied the carbonization (pyrolysis) of cellulose, lignin, and wood at 500 to 1000 °C [85]. Pyrolyzed biomass showed the aromatic C=C band at 1590 cm^{-1}, contrasting the assignment at 1610 cm^{-1} in hydrochar. This band was also assigned as carbonyl groups conjugated with aromatic structures. Three

aromatic C-H vibrations appear in the range of 900-700 cm^{-1}, and are well defined. While the Ishimaru et al. assignments are more specific than the hydrochar assignments, they also appear to have slightly different positions than the hydrochar assignments. For example, the C=C aromatic assignment by Ishimaru et al. is redshifted 20 cm^{-1} from the hydrochar assignment. Further, the assignment of the ether bridge at 1250 cm^{-1} is about 100 cm^{-1} blueshifted from the hydrochar Diakite et al. assignment of 1150 cm^{-1} [40]. Ishimaru assigns the ether as a bridge between two aromatic rings. The assignments of Ishimaru et al. can be a marker for the aromaticity of the hydrochar material, where shifts in position towards the Ishimaru assignments in hydrochar could indicate a growing aromatic content.

Raman Spectroscopy

Raman Spectroscopy measures the change in frequency of light scattered off a material from an incident laser (in the UV-Visible region), which is called the Stokes line, a weak effect compared to the intensity of light that is scatter elastically, that is, without a change in frequency. The elastic scattering phenomena is dependent on the change in the polarizability of the material with molecular vibrations [86]. Polarizability is the proportionality of the change in the electric field of the molecule relative to the electric field of the laser. The selection criteria for the Raman Effect is that the derivative of the polarizability vibrational mode cannot be zero. As a result, Raman is good at detecting covalent bond vibrations, especially ones with small dipole moments, such as C-C and C=C bonds. As a result, Raman Spectroscopy is a valuable technique to analyze carbon materials, and is especially useful in the information it can give about the types of defects that occur in highly carbonized materials.

In a paper by Ferrari and Robertson, Raman spectroscopy of disordered and amorphous carbon is carefully assessed with respect to its ability to characterize changes in these materials with their sp^2 carbon content and degree of clustering, degree of hydrogenation, and the sp^3 carbon content. The authors note that visible Raman spectroscopy is much more sensitive to sp^2 sites over sp^3 sites, due to the π-electrons in the sp^2 carbon. The π-electrons can form conjugated systems, and 6-membered aromatic rings maximize the

interaction, resulting in long-range polarizability. The relevance of Raman Spectroscopy of amorphous carbons and nanocrystalline graphite to hydrochar is apparent in that the Raman spectra of all these materials are dominated by the G and D peaks [38, 64]. The G and D peaks refer to specific molecular vibrations: The G mode and D mode are shown for 6-membered rings in Figure 6, left. The G mode has E_{2G} symmetry, and does not need the presence of 6-membered rings. The D mode has A_{1G} symmetry, and only occurs in six fold aromatic rings. The D and G bands appear at 1350 and 1580-1600 cm^{-1} respectively. Ferrari and Robertson state that the positions, intensities, and widths can give information about the structure of the material. A good example of this is shown in Figure 6, middle, with a graph of the ratio of the D to G band intensities as a function of the polyaromatic lattice (planar, fused 6-fold aromatic rings) characteristic length, L_a.

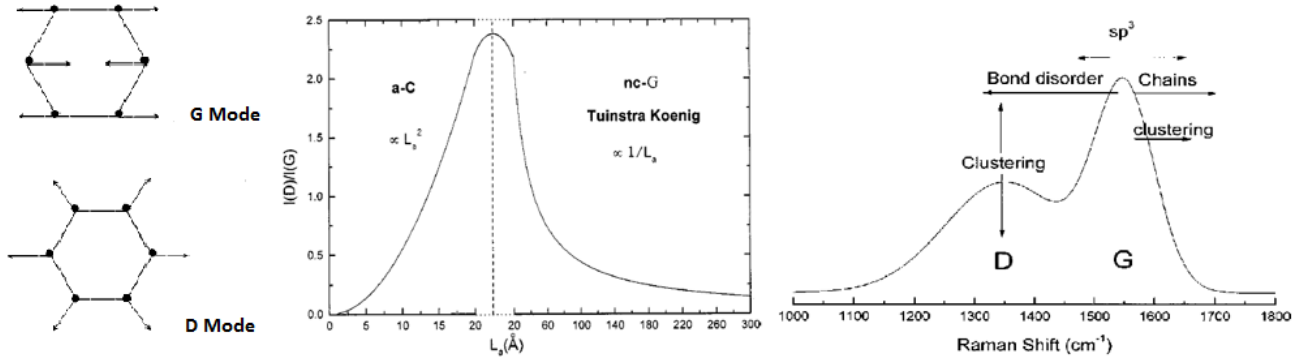

Figure 6. Raman spectroscopy interpretation in amorphous carbon and nanocrystalline graphite. Left) G and D vibration modes in an arene ring. Middle) D/G Band intensity ratio as a function of the aromatic cluster size (or lattice size) in amorphous carbon (left) and nanocrystalline graphite (right). Right) Raman spectra interpretation by the G band position and D band size. Reprinted figures with permission from Ref [38]. Copyright (2000) by the American Physical Society.

For crystal lattice sizes of zero, there is a very small D band, but and as the lattice size and number of rings increases, they add constructively and the D band intensity increases to a maximum around 20 Å. With increasing lattice size, the symmetry of the lattice increases, and contributions of the D mode on different rings start to cancel. The first part of the graph refers to the behavior of a-C, or amorphous carbon, and the D/G ratio is proportional to the lattice size squared, meaning the D/G is proportional to the lattice area or number of rings present. The other side of the graph applies to nc-G, or nanocrystalline graphite,

following the Tuinstra and Koenig equation, where the intensity decreases as the amount of edge sites decreases relative to the total area. Since hydrochar is not considered to have a significant polyaromatic content [32, 76], the D/G ratio is expected to increase with increasing carbon content. With changes in nanocrystalline graphite to form amorphous carbon, the G band drops in position from 1600 to 1510 cm^{-1}, which is caused by the increased bond disorder.

The Raman spectra of carbon materials is expected to change with increasing graphitization or aromatization. In a study by Ishimaru et al., cellulose was pyrolyzed, and with increasing temperature the D band position increases and the width decreases. The G band also decreases in width, and the right shoulder of the D band decreases

From the Ferrari and Robertson study, it was noted that the carbon material Raman spectra may change through band position, intensity, and broadness of peaks. To understand these changes and to understand specific vibrational modes, it is necessary to fit the Raman spectra. The Ishimaru et al. study also fit the spectra to quantify the D and G bands behavior. To fit the spectra requires a knowledge about the most significant vibrational modes for the carbon materials, where they should be located, and what type of line shape should be used. Several fitting methods have been proposed and implemented in the field of amorphous carbon materials.

Sadezky et al., in a study of commercial carbon black, diesel soot, spark-discharge soot, and graphite [43], proposed a combination of Gaussian and Lorentzian peaks to fit the Raman spectra and to gain structural information. In the curve fitting of the samples, the D3 was allowed to be Gaussian or Lorentzian, and the D2, D3, and D4 bands may not fit for a positive value. The best fitting combination was determined with all of the bands shown in Table 2, with the D3 peak in Gaussian form. The authors justified the decision, stating a literature precedent as the peak is amorphous and is randomly distributed on interstitial places by the graphitic lattices.

Table 2. Raman band assignments for soot developed by Sadezky et al. Reprinted (adapted) from Raman microspectroscopy of soot and related carbonaceous materials: spectral analysis and structural information, Carbon, Volume 43, 1731-1742, 2005. Copyright (2005). Ref #.

Band	Raman Shift (cm^{-1})			Vibration mode
	Soot	Disordered Graphite	Highly ordered graphite	
G	1580, s	1580, s	1580, s	Ideal graphitic lattice (E_{2g}-symmetry)
D1 (D)	1350, vs	1350, m	-	Disordered graphitic lattice (graphene layer edges, A_{1g} symmetry)
D2 (D')	1620, s	1620, w	-	Disordered graphitic lattice (surface graphene layers, E_{2g}-symmetry
D3 (D'')	1500, m	-	-	Amorphous carbon
D4 (I)	1200, w	-	-	Disordered graphitic lattice; polyenes; ionic impurities

From the Raman spectra fitting, Sadezky et al. note that the FWHM (full widths at half maximum) can indicate molecular structure, with larger values indicating a decreasing degree of graphitization. However, ratios between the G and D band or between other combinations of bands did not seem to show clear-cut trends and there seemed to be a mismatch between the XRD and Raman Spectroscopy in terms of the relative amount of ordering between different types of soot.

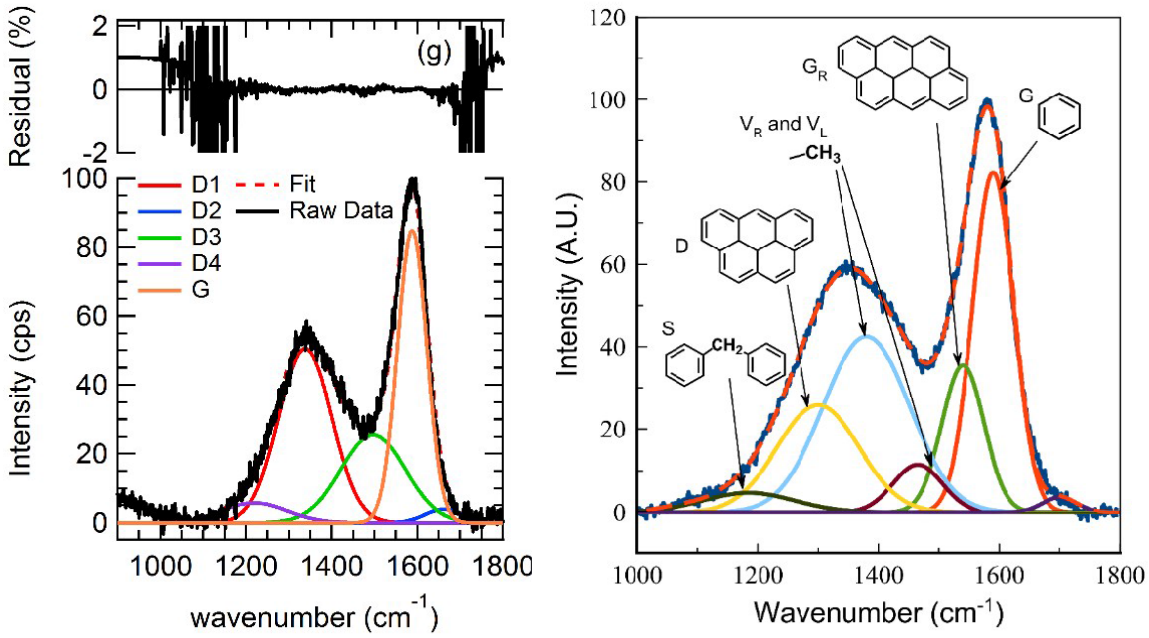

Figure 7. Timko et al. Raman spectra fitting of ball milled hydrochar. Left) Spectra fit using Sadezky et al. assignments. Right) Fitting with Li et al. assignments. The Sadezky et al. method uses 4 Lorentzian curves and 1 Gaussian curve; the Li et al. method uses 9 gaussian peaks. Reproduced from study [64] with permission from the Royal Society of Chemistry.

The Sadezky et al. fitting method has been applied to the Raman spectra of hydrochar in a study by Timko et al., to track changes in the material as it was subjected to ball milling, a mechanochemical treatment [64]. To connect the Raman spectra changes to structural insight into the material, the two fit area ratios were applied. The R2 metric of Beyssac et al. [39], D1/(G+D1+D2), is a measure of graphitization with decreasing values indicating an increasing graphitization. This metric incorporates the D2 breathing mode which also has E2G symmetry, but only occurs on surface layers.

The Li et al. Raman study of coal is another significant example of the application of novel Raman fitting assignments to an amorphous carbon. Brown coals pyrolyzed at varying temperatures between 500 and 900 °C were fit using the assignments in Table 3. The assignments came from a variety of literature sources, and includes aliphatic modes, as well as the carbonyl and ether groups, besides the aromatic ring vibration modes. Li et al. fit the spectra using Gaussian type peaks, and plotted the ratio of different groups against pyrolysis temperature.

Table 3. Li et al. Raman fitting assignments, developed to characterize brown coal. Reprinted from Ref. [42]. Copyright (2006), with permission from Elsevier.

Name	Position cm^{-1}	Assignment	Bond
G_L	1700	Carbonyl group	sp^2
G	1590	Graphite; aromatic ring quadrant breathing; alkene C=C	sp^2
G_R	1540	Aromatics w/ 3-5 rings; amorphous carbons	sp^2
V_L	1465	Methyl or Methylene (CH_3/CH_2); semi-circle breathing of aromatic rings; amorphous carbon structures	sp^2 sp^3
V_R	1380	Methyl; Semi-circle breathing of aromatic rings; amorphous carbon structures	sp^2 sp^3
D	1300	D Band on highly ordered carbonaceous materials; C-C between aromatic rings and aromatics with ≥6 rings	sp^2
S_L	1230	Aryl-alkyl ether; para-aromatics	sp^2 sp^3
S	1185	$C_{aromatic}$-C_{alkyl} ; aromatic or aliphatic ethers; C-C on hydroaromatic rings; hexagonal diamond carbon sp3; C-H on aromatic rings	sp^2 sp^3
S_R	1060	C-H on aromatic rings; benzene (ortho-di-substituted) ring	sp^2
R	960- 800	C-C on alkanes and cyclic alkanes; C-H on aromatic rings	sp^2

			sp^3

While the Li et al. assignments were derived from the literature, and fit the brown coal spectra well, it should be noted that the assignments are strictly derived from literature, and with different peak widths the spectra may be over fit and there is significant room for variability in peak intensity based on assigned position and width. In a study by Timko et al the Li et al. Raman fitting method was used to characterize hydrochar. [64]. As shown in Figure 7Figure 7, the spectra shows a good fit, and indicates the importance the presence of polyaromatic clusters of different sizes, along with methyl groups and methylene bridges. The ability of the fitting method to obtain a good fit does not in and of itself indicate that the peak assignments are representative for the given material. For example, there is a peak assigned for aromatic clusters larger than 6 rings, and little evidence exists outside this study that would indicate the formation of aromatic domains of this size. The Li et al. assignments are based off the literature exclusively, and hydrochar differs significantly from brown coal. The Li et al. fitting of brown coal features a wide envelope around 1300 cm^{-1}, with several bands (S, Vr, Vl) that are comparable to the G band in area, and the G band is smaller than the D band area, which differs significantly from the hydrochar spectra.

Brown et al. study

Brown et al. employed molecular modeling computations of model compounds to better interpret the Raman spectra of hydrochar [37]. The vibrational spectra of small, functionalized polyaromatics (and furan species) were simulated to determine the effect of configuration and functionality with the number of aromatic rings in a polyaromatic cluster on the D/G intensity ratio and G and D band positions. In addition, the other most significant vibrational modes were identified (along with the most significant band in the furan ring), and based off these, a fitting method was developed for hydrochar. The band assignments are listed in Table 4. The Breathing mode L, Breathing mode R, and D band are all symmetric breathing modes in arene rings, which are shown in Figure 8. In addition, Kekulé Mode, or the Kekulé Band, is another type of aromatic breathing mode, and is also shown in the same figure. The Kekulé Band is not found in single

arene ring compounds, but is found in polyaromatic rings. At around the same location as the Kekulé band is another band seen in furanic species, so the Kekulé band represents both arene and furan vibration modes. Finally, the G Band, the G_R band, and the G_L band are related to the Asymmetric Breathing Mode shown in Figure 8. The C-H Wag is an aromatic ring mode, involving motion of the hydrogen in the same direction normal to the plane of the ring. The Methyl and aliphatic mode CH_2/CH_3 mode are modes in methyl groups and alkyl groups directly off an aromatic ring. The methyl mode is a group mode, involving the methyl group and motion in the aromatic ring. The ether and carbonyl group are those near aromatic rings. The fitting assignments in Table 4 bring a more accurate and representative method for analyzing changes in the spectra of hydrochar.

Location (cm^{-1})	Band	Notation	Int.	Description
1011	Breathing mode L	Br_L	w	Arene ring modes of various symmetries
1096	Ether	Ether	w	Functional Group Mode
1179	C-H wag	C-H wag	mw	Carbon hydrogen wag on arene rings
1262	Breathing mode R	Br_R	mw	Arene ring modes of various symmetries
1341	D Band	D	ms	Symmetric and Kekulé breathing modes
1390	Methyl	Methyl	m	Functional group mode

1441	Kekulé/furan band	Kekulé	m	Arene ring C sp^2 stretching; A_2 symmetry; Furan
1463	Aliphatic mode	CH_2/CH_3	vw	Functional group mode
1506	G L band	G_L	m	Arene ring C sp^2 stretching; E_2G symmetry
1580	G band	G	s	Arene ring C sp^2 stretching; E_2G symmetry
1612	G R band	G_R	w	Arene ring C sp^2 stretching; E_2G symmetry
1695	Carbonyl band	C=O	w	Functional group mode

Table 4. Raman spectra fitting assignments used in this study. Adapted from Brown et al.[37]

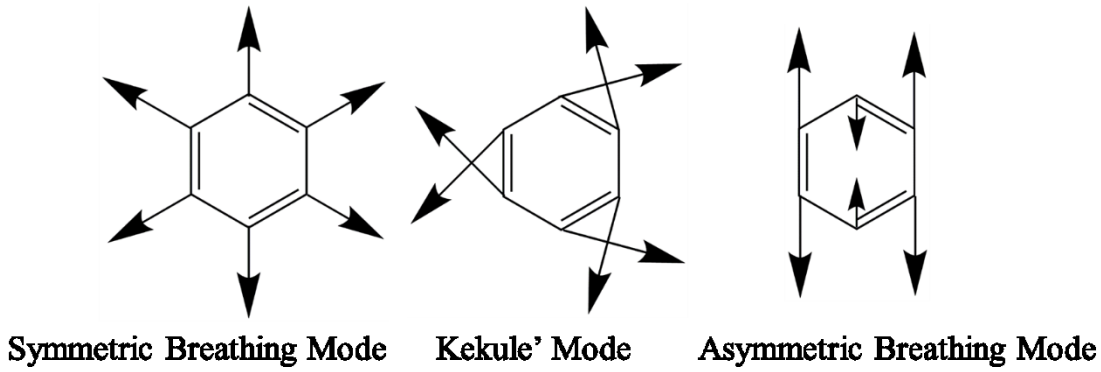

Figure 8. Significant Raman-active stretching modes, illustrated on a single arene ring. The Symmetric Breathing Mode manifests as the D band, the Kekulé Mode appears as the Kekulé band, and the Asymmetric Breathing Mode appears as the G band. Note that the Kekulé Mode is not observed in benzene, but in polyaromatic clusters. Adapted from Brown et al. (submitted for review)[37].

In spectroscopy, peak intensities, positions, and widths contain information about the chemistry of the substance tested. In Raman Spectroscopy, the relative intensities of the D and G bands, along with their positions, indicate changes in the aromatic domain size, as shown in Figure 9, which were arene-ring clusters simulated in the Brown et al. study [37]. The D/G intensity ratio increases to a maximum at 3 rings,

before rapidly decreasing. The G band position seems to show the inverse of the D/G intensity ratio trend, decreasing to a minimum at 3 rings, but shows much more variability than the intensity ratio. The D Band position trend shows a consistent shift to lower wavenumbers with increasing aromatic clusters size after two rings.

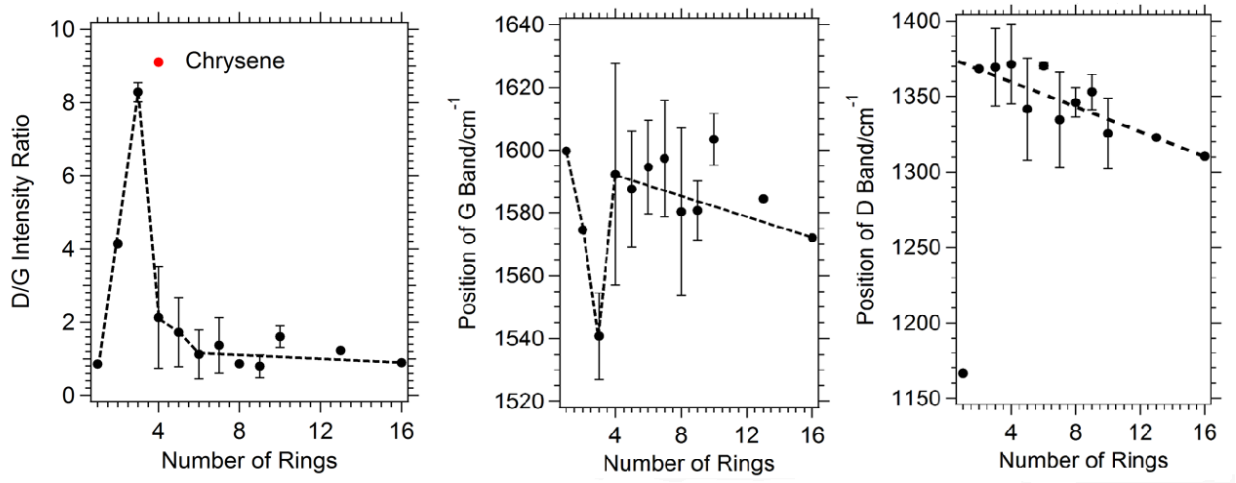

Figure 9. Trends in the D and G bands of the simulated Raman spectra of arene-polycyclic aromatic hydrocarbons as a function of aromatic ring size. Left) D/G intensity ratio. Middle) G band position. Right) D band position. DFT simulations were performed by Brown et al. Note that the error bars vary widely or are not present at all time points as the number of samples per time point varies from 4 for 4-ring aromatics to 1 for the 1, 2, 9, and 10 ring structures. All polyaromatics are planar 6, composed of 6-carbon fused rings. Adapted from Brown et al. [37].

The Brown et al. study includes a great deal more evidence to suggest the structure of hydrochar based on the Raman Spectra. The Kekulé mode was the third most intense vibrational mode in aromatic carbons, and the trends for the Kekulé band (normal and aldehyde-functionalized) position, K/D intensity ratio, and K/G intensity ratio as a function of the number of aromatic rings were also calculated and plotted. In addition, furanic species (furan, benzofuran, dibenzofuran, and bifuran) were modeled (normal and aldehyde-functionalized) for their G band, D band, and Furan mode positions, and D/G, Furan/G, and

Furan/D intensity ratios. The unfunctionalized furan species are not likely a part of the hydrochar structure due to the D band positions, which were far too low by about 100 cm^{-1} (200 cm^{-1} for furan). A comparison of all the modeled species (individual arene species of varying ring numbers, furan and the fused arene furan, and the aldehyde-functionalized versions of these species) by the Raman parameters (G band position, D band position, Kekule or Furan band position, D/G intensity ratio, (Kekule or Furan)/G intensity ratio, and (Kekule or Furan)/D intensity against the hydrochar spectra values showed that 6-8 ring arenes satisfied all of the parameters. Conditions where the Raman spectra is composed of furan and arene modes is also possible, provided they are carbonyl substituted furans and arenes with 2-3 rings. The study compared the findings of the Raman study against an NMR spectra of hydrochar, which implied a significant aliphatic content and a ~2:1 furan to arene ratio.

Mass Spectrometry

Mass Spectrometry is a widely used analytical technique, often coupled with gas chromatographs or liquid chromatographs to identify organic compounds by the ion fragment pattern [87]. Electron impact ionization (or EI) is a common method of ionizing a sample, using electrons fragment the compound and form cations, which are sorted by mass to charge ratio in a spectrometer. This pattern can identify the components and structure of the species, by the identity of the peaks present, the ratio between them, and the absence of other peaks [88]. To perform Mass Spectrometry to a solid material the sample has to be vaporized to enter the ionization step, which is outside of the design of standard Mass Spectrometers.

Solids have been analyzed by mass spectrometry, notably using the Aerosol Mass Spectrometer (Aerodyne Research Inc.), which is designed to vaporize non-refractory organic carbon aerosol particles [47, 89-90]. In this study, the Soot Particle Aerosol Mass Spectrometer (SP-AMS) (Aerodyne Research Inc.) was used to analyze hydrochar. The SP-AMS has two vaporizers, a thermal vaporizer and a laser. The thermal vaporizer, operating at 600 °C is effective for organic matter in aerosols, but cannot vaporize refractory black carbon (rBC), which does not enter the gas phase 600 °C. To overcome this, the instrument employs

a laser to vaporize rBC. The instrument is described by Onasch et al. [47], and is shown in Figure 10. The instrument is developed for atmospheric aerosol particles, which are already in aerosol form when they enter the inlet. The particles pass through the aerodynamic lens inlet, which is a series of slits designed to focus the particle beam, and as a result tends to exclude large or irregularly shaped particles. The particle beam is pulled in to a vacuum chamber, and it passes through the chopper TOF region.

The chopper is set to either Open or Closed mode. In the instrument, sample may stick to the walls and desorb, entering the ionization chamber and alter the signal. The chopper allows for this effect to be subtracted out, by running the spectrometer continuously but varying the sampling step-wise. The two settings for the chopper, Open and Closed, are alternated, and the Closed spectra is subtracted against the Open one, giving the spectra for the given time point.

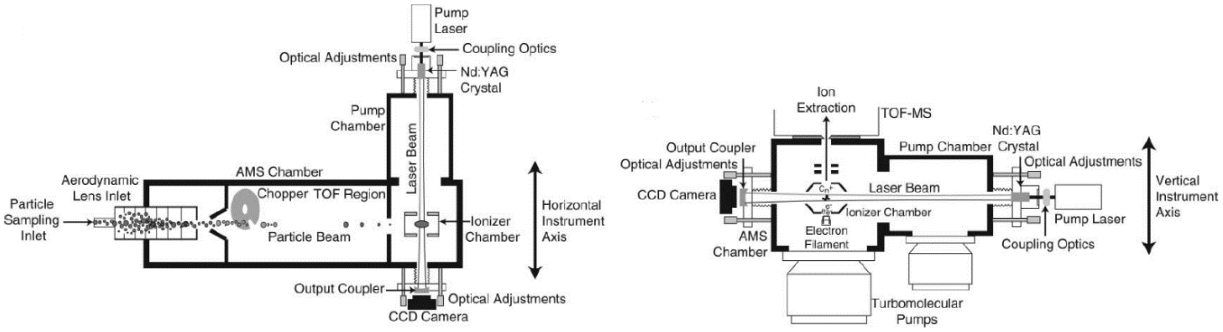

Figure 10. Diagram of SP-AMS. a) The sample enters the inlet as a particle stream, and is pumped into the ionizer chamber and is vaporized by the laser beam and a tungsten filament. b) An electron filament in the ionizer chamber ionizes the sample, and turbomolecular pumps move the sample to the ion extraction outlet, where they are separated by their mass to charge ratio, m/z. Adapted from Ref. [47]

The particle passes into the ionization chamber, where the near infrared 1064 nm laser (power densities > 0.2 MW/cm^2) vaporizes the sample. A CCD camera is at the bottom of the ionizer chamber to measure the light scattering and incandescence of the particles, so that refractory black carbon (rBC) can be detected. In addition to the laser vaporizer, a heated tungsten vaporizer is also used to vaporize the sample. In the normal direction to the laser and the particle beam is the electron emitting filament, a tungsten wire which emits electrons at 70 eV to ionize the vaporized samples creating cation species. The

ions of the original sample leave through the ion extraction outlet to the spectrometer. The spectrometer is a high-resolution time-of-flight spectrometer, developed by Tofwerk, Inc. The ions are moved through the spectrometer laterally using series of magnets to reflect the beam. This method separates ions by mass to charge ratio by as those with higher values move slower and are detected later. The detector collects and measures the ions that contact it per unit time as a function of time. The time signal is then converted to the m/z from the relation between time to reach the detector and the mass-to-charge of the ion. The ion rate (in unit Hz) can then be converted to concentration [47].

Methodology

Hydrochar Preparation

Hydrochar is prepared based off the method described by Timko et al. [64] 28.152 g D-(+)-glucose (Sigma-Aldrich) was dissolved in 100 ml DI water (purified to a minimum resistivity of 17.8 MΩ·cm) by mixing for 20 minutes. 100mL of this solution was transferred into a 160 ml PTFE-lined autoclave. Solutions were reacted at 180 °C starting when the oven was turned on, and samples were left in the oven to cool to ambient temperature overnight (10-11 hours). Heating and cooling profiles are shown in the Appendix. Reaction contents were washed with 100 mL of 50/50 ethanol and DI water mixture for 3 hours. Hydrochar was separated from the reaction contents by vacuum filtration through Whatman #1 filter paper. 50/50 ethanol/DI water solution was used to remove residual organics from the solid until the filtrate was clear. This was then dried at 65 °C for 24 hours, and stored in a desiccator. 3-5 batches were produced at each major time point. One batch was made each of 20 and 72 hour hydrochar.

3-Hour Hydrochar Collection Method

When 3 hour reaction time hydrochar was prepared, essentially no hydrochar could be collected using the filtration method described. When ethanol was used to wash the hydrochar as it was being filtered, the char appeared to go through the filter paper. Instead of filtering, the reactor contents were chilled in a 4 °C refrigerator for a few hours before being divided and centrifuged at 4000 rpm for 40 minutes. The supernatant was removed using a pipette, and the solid was dried for 24 hours at 65 °C.

Yield is calculated as the mass of hydrochar collected divided by the initial amount of sugar in the reactor. The mass of sugar used in the reaction is 28.152 g * mass solution in reaction/ mass original solution.

Elemental Analysis

Elemental analysis was performed at Midwest Microlab (Midwest Microlab Inc.). C content and H content were determined by the dry combustion method at 990 °C using an Exeter CE440 analyzer. O content was determined by the Unterzaucher Method. 1 CH and 1 O analysis was run each for 4-hour, 8-hour, 16-hour,

and 24-hour hydrochar, while 3 12-hour hydrochar samples were tested with 2 CH analyses and 1 O analysis each. In addition to the hydrochar samples, a pyrolyzed 8hg sample (pyrolyzed at 500 °C under nitrogen atmosphere for 10 hours, from the same hydrochar that was tested by the elemental analysis) and a carbon black sample (Regal Black 300, Cabot Corp) to compare the method with a known standard.

IR Methodology

Transmittance IR Spectroscopy

Transmittance IR Spectroscopy of hydrochar were collected through a KBr pellet. Potassium Bromide (KBr, Perkin-Elmer, FTIR grade) was dried overnight at 100 C overnight, then ground into a fine powder in an agate mortar and pestle, and dried again for at least two hours at 100 °C until use. Hydrochar was dried for at least one hour at 100 °C before use. 280 mg of KBr was gently mixed with 1.4 mg of hydrochar. This was then loaded into a pellet press (Pike Technologies, Inc.), forming a 13 mm diameter pellet using 7 tons of pressure for 6 minutes. The KBr pellet was then loaded into a Bruker Vertex IR (Bruker, Inc.). 256 scans of the background (air subtraction) and 256 sample scans were collected, at a resolution of 4 cm^{-1}, from 4000-600 cm^{-1}.

Diffuse Reflectance Infrared Fourier Transform Spectroscopy (DRIFTS)

DRIFTS spectra were collected on a Nicolet Magna 560 with a SpectraTech DRIFTS cell (Specac, Inc.). Samples were taken at 150 °C, after two hours of the sample drying at that temperature and purging of the cell purging under nitrogen atmosphere. 128 scans were taken for the sample and the background, with a resolution of 4 cm^{-1}, over the range of 3800-650 cm^{-1}.

Raman Spectroscopy

Instrument Settings

Raman Spectroscopy was conducted on a Horiba XploRa Raman microscope (Horiba Scientific), using a 532 nm laser at a power of 10 mW. A 1200-line grating was used with an aperture of 100 and slit width of 300. 25 scans were collected with 2 second accumulations, capturing the range 200-2600 cm^{-1} with a

midpoint at 1400 cm^{-1}. Laser light was manually focused on the sample at 100x magnification with an Olympus lens.

Baseline Subtraction Procedure

Each spectra was baseline subtracted to remove the fluorescence present in the Raman Spectra to varying degrees. In the Horiba Raman Instrument LabSpec software program, a baseline was manually fit a 3rd order polynomial such that the baseline lies tangent to the Raman Spectra at the regions of 400-700 cm^{-1} and 2200-2400 cm^{-1}, as shown in Figure 11Figure 11. After the spectra is baselined, the spectra was smoothed using a smoothing factor of 2 in the LabSpec Raman software.

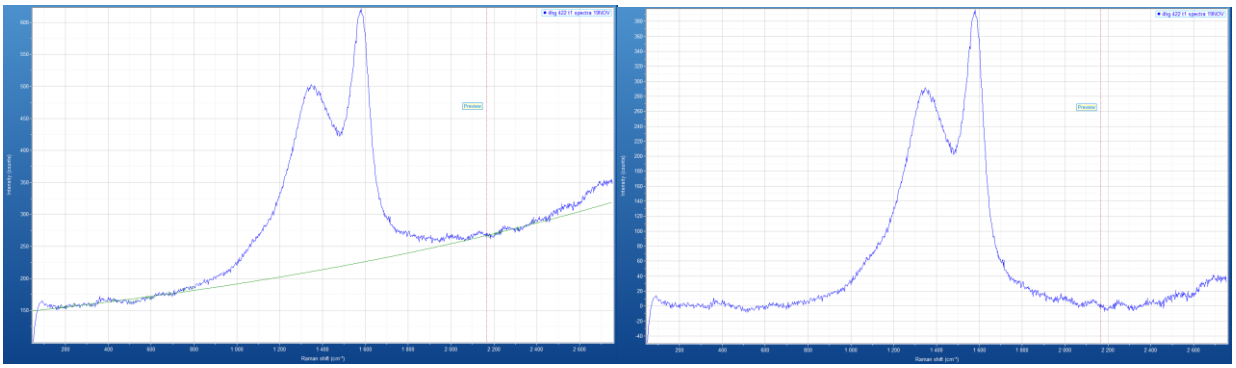

Figure 11. Representative baseline subtraction of a hydrochar Raman spectra. a) Raman spectra with baseline (green). b) Properly baselined spectra.

Raman Spectra Fitting Procedures

The Raman spectra were fit using the band assignments from Brown et al. and multiple fitting procedures were tested using the fitting assignments. The modification was necessary as bands can change in position, and accounting for these changes can lead to a more reliable spectra fit and the changes in the band positions with reaction time can have structural significance for the hydrochar. The benefits of a more reliable fit and more information to interpret is the danger of overfitting the Raman spectra.

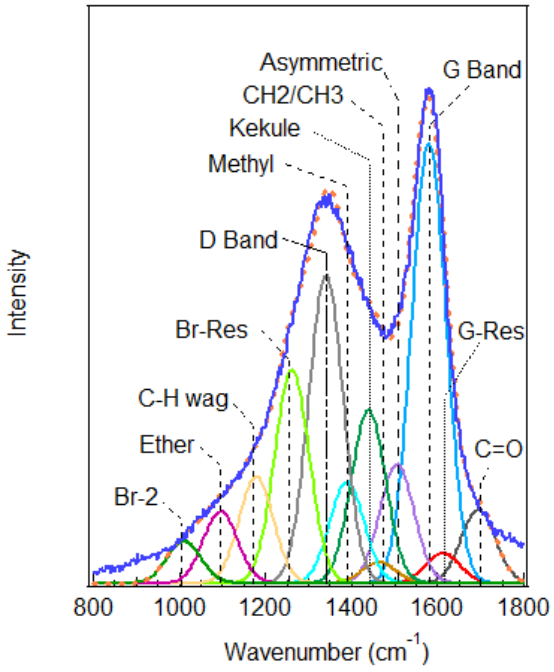

Figure 12. Raman spectra with fit peaks. The Raman spectra is shown as the dark blue curve on top of the fit peaks. The dashed orange line is the sum of the fit peaks, while the Gaussian peaks below the hydrochar Raman spectra are the fit peaks. The intensity scale is not given as the peak areas are reported as the percentage of the total peak fit area in the spectra.

The 12 bands of fixed width and position means 12 degrees of freedom for the intensity (or area). If positions were also allowed to vary there would be 24 variables, and for such a broad signal the peaks could shift significantly just to obtain a slightly better fit. This is a particular concern as the spectra have some noise. Therefore, a stationary method was compared to a variable method, where the Kekulé, D band, and G band, the largest bands and the most significant from a structural perspective, were relaxed in position sequentially.

A fit spectra for hydrochar is shown in Figure 12, and shows overlapping peaks, which is especially concerning in the region containing Kekulé, Methyl, and CH_2/CH_3. Allowing the Kekulé to vary in this region could lead to problems with the Kekulé shifting more than reasonable to obtain a good fit, so different sequences were tried to prevent overfitting. The sequence of fitting was determined by trial and error, and two other sequences are reported in the appendix.

Stationary Fitting Method

The stationary fitting method is called so because the peaks are not allowed to change in position from the calculated values derived from Brown et al. (in preparation). Spectra were fit in MagicPlot ver. 2.5 (Magic Plot Systems, LLC). A version of the software (MagicPlot Student) is available as a free download (http://magicplot.com). Each spectra was fit by a sum of Gaussian type peaks of fixed equal half-width half maxima (HWHM value of 47 was used) using the sum of least squares regression method over the range 1000-1750 cm^{-1}. If either the G Resonance or the CH_2/CH_3 peak fit to a value less than zero (the CH_2/CH_3 almost always did), the peak was locked to an area of zero and the spectra was refit. In fitting a curve to fit peaks using a fitting algorithm, Meier [91], in a paper on curve-fitting of vibrational spectra, noted that setting peak areas initially is a crucial step to converge on the best fit. However, here peak-positions and widths are initially fixed, and most peaks are not spaced close to each other, and initial peak areas have not impacted the peak fitting in the stationary method.

Variable Fitting Method

The Variable method is a modification of the stationary method to account for shifts in location of the Kekulé, D, and G Bands. Initially, all bands are fixed in position, and the fitting is conducted. Unlike in the Stationary method, all bands are allowed to vary during the fitting procedure, even if they fit to a negative area. After the first fitting, the position of the G Band allowed to vary and the fitting is repeated. The resulting peak location of the G Band is then locked in place and the process is repeated with the D Band allowed to vary in position. The spectra is refit, and the new D Band location is locked in place. After this, the Kekulé position is allowed to vary with the fitting, and the fitting is repeated. After this point, if any peaks are negative (usually both the CH_2/CH_3 and the G-Resonance), then the lower peak of the two is removed from the fitting method, the peak positions are set to the original values and locked, and the fitting is repeated, varying the G, D, and Kekulé bands.

Data Reporting

The resulting peak areas for a given spectra were converted into the percent of total peak fit area. Since all the peaks have the same half-width half-maxima, the percent of total peak fit area is also the percent intensity. The peak percentages were then averaged for each time point between the fifteen spectra taken. In addition, the G band, D band, and Kekulé Band positions were recorded (if varied), along with the adjusted r^2 value for the fit. The uncertainty is displayed with error bars which are the confidence intervals. The confidence interval is a function of the standard deviation, number of samples, and the confidence rating, for which 95% was used (meaning there is a 95% chance the average is located in that area). Plots were constructed using Igor Pro (Wavemetrics Inc.).

Aerosol Mass Spectrometry

Sampling system

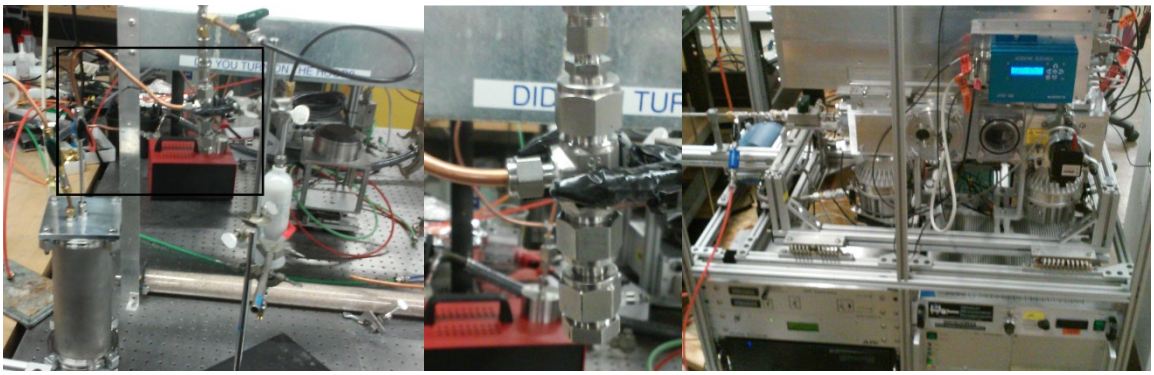

Figure 13. Images of the SP-AMS and the sample loading configuration. Left: T-junction containing the char is positioned before a junction to a bypass line to vent (center-top of frame) with an air filter for collecting fine particulate. The junction proceeds to the 2L hold volume (bottom-right) for proceeding to the instrument. Middle: The T-junction is where the sample is loaded. Right: The line for instrument sampling proceeds to a bypass junction to vent with a hand valve and an air filter. The sample line proceeds through a final valve before entering the SP-AMS.

The SP-AMS is designed for the study of atmospheric organic aerosols, which are naturally in aerosol form. In order to study hydrochar with this instrument, the hydrochar must be aerosolized. For this system, a manual aerosolizing system was assembled, as it had to also meet the ability to purge the sample and inlet lines of oxygen, which affects the performance of the system. The sampling system is shown in Figure 13 along with the schematic diagram representation in Figure 14. An Argon tank is connected to a regulator (set to 30 psig) which proceeds to a valve (V0). After V0 the line proceeds to a junction with two valves in parallel, V1 and a needle valve. V1 is opened to rapidly increase the gas flow rate and aerosolize the sample. The needle valve was set open such that the Argon purge flow rate stays at approximately 1 Std. L/min. The system proceeds to a junction with a vent line, where the valve V2 is followed by a HEPA filter before leaving to atmosphere. The line continues into another Swagelok T-junction, which is shown in the Figure 13, middle. The sample is loaded in the bottom and screwed into place before purging the system and aerosolizing the sample. This design is intended to prevent the sample from sweeping with the carrier gas near the instrument inlet and clogging the line. The line continues through the valve V3 to

a 2 Liter volume, shown in the left panel. This volume dilutes the sample and allows for a more uniform mass loading into the instrument. From the 2L volume, the outlet line passes through valve V4 and proceeds to a junction with a vent line with valve V5 and an air filter to atmosphere. The junction continues to V6 before entering the instrument. The flow rate into the SP-AMS instrument was set at 1.6 mL/s.

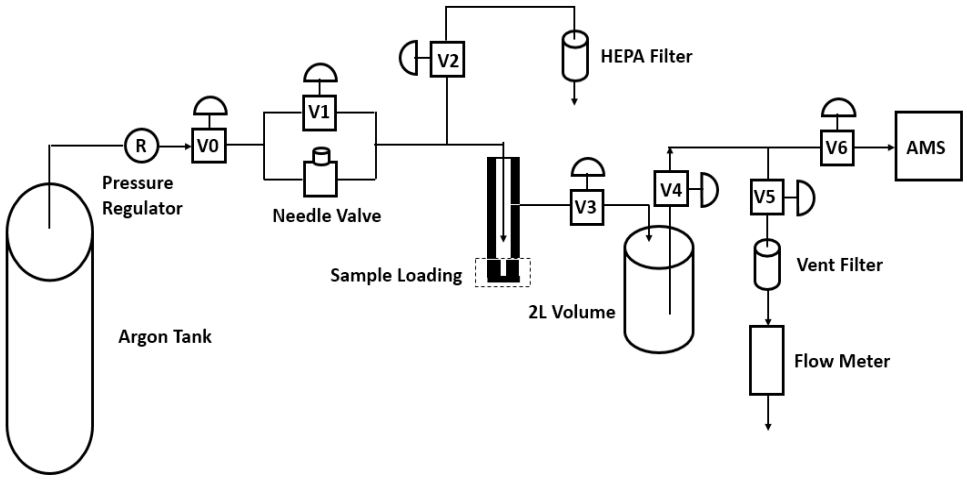

Figure 14. Diagram of the SP-AMS sampling system configuration. Lines connecting the sample material to the AMS are a combination of copper tubing, plastic lines, and metal Swagelok fittings.

Sampling Procedure

When using the sampling configuration, either V5 or V2 must be open at all times to prevent the system from pressurizing.

Initialize System. Close valves V0, V1, V2, and V6. Open valves V3, V4, and V5. Set regulator pressure to 30 psig.

Load Sample. Unscrew sample loading cap and wipe clean with Kim wipes. Grind dried sample. Weigh 0.5 mg of sample. **Record sample identity and weight**. Load into sample loading cap. Tighten back into place.

Purge inlet line. Slowly open V0, and adjust flow further using needle valve to modulate flow and flow meter to ensure flow rate reaches roughly 1 L/min. **Record Argon Purge Flow Rate**. Purge for at least eight minutes. **Record purge start and end times.**

Aerosolize sample. Open V1 45 degrees for 2 seconds. Close V1. Wait 45 seconds before beginning step 5.

Prepare for sampling. Open V2 and then close V5. Immediately proceed to step 6.

Begin Sampling. Open V6. Press Collect on AMS software program. **Record Run Start number**. Observe the displayed mass loading into the instrument (given in $\mu g/m^3$). Observe the displayed inlet flow rate (given in mL/min). Follow procedures below if applicable.

If inlet flow rate drops more than 0.03 ml/min, the inlet is clogged. Immediately stop the program and close V6.

If mass loading is greater than 200 $\mu g/m^3$, the mass loading is too high. Stop the run on the AMS software and close valve V6. Open valve V5, then close valve V2. Wait 30 seconds, then repeat sampling procedure from step 5.

If mass loading is lower than 15 $\mu g/m^3$, the mass loading is too low. Follow the applicable procedure below.

If this is the first attempt at reaching step 6, stop the run on the AMS software and close valve V6. Open valve V5, then close valve V2. Repeat sampling procedure from step 4.

If this is the second attempt at reaching step 6, too much of the sample flushed out of the system. Proceed to step 7.

End Sampling. When done sampling, press stop on AMS software program. **Record Run End Number**.

Reproducibility

In this study a manual sampling system was used to aerosolize the hydrochar and analyze in the mass spectrometer. To do so requires establishing that the technique is reliable for the study of hydrochar. Several sources of uncertainty has been identified when using the mass spectrometer, such as the data point variability, sample variability, and the batch variability. Data point variability refers to the variability between data points while the mass spectrometer is running a sample. The sample variability is the variability between samples from the same hydrochar batch run at different times on the mass spectrometer with identical instrument settings. The batch variability of different hydrochar batches prepared at identical conditions (on different days) in the mass spectrometer. The greatest source of uncertainty or variability determines the degree to which the mass spectrometry technique can be used quantitatively.

The variability between data points on the mass spectrometer operated continuously on the same sample of the same material is shown in Figure 15. The composition appears to be fairly constant with reaction time and ranges only 3.4% for CH composition, 2.4% for CHO1 composition, and 1.3% for CHOgt1. The data point variability appears to be small, and seven data points appears to be plenty enough to have a reliable average.

The variability between samples of the same hydrochar batch on the mass spectrometer operated continuously is shown in Figure 16. The composition is nearly constant with one outlying trial, t3. The composition ranges 1.7 % for CH composition, 1.9 % for CHO1 composition, and 0.4% for CHOgt1 composition. The trials have similar numbers of data points (6-8 data points), and were run consecutively, with no other material run between. The trial that differs the most (the third trial), was run with a significantly higher mass loading than the other three runs, which highlights the importance of ensuring reproducible mass loading of hydrochar into the AMS.

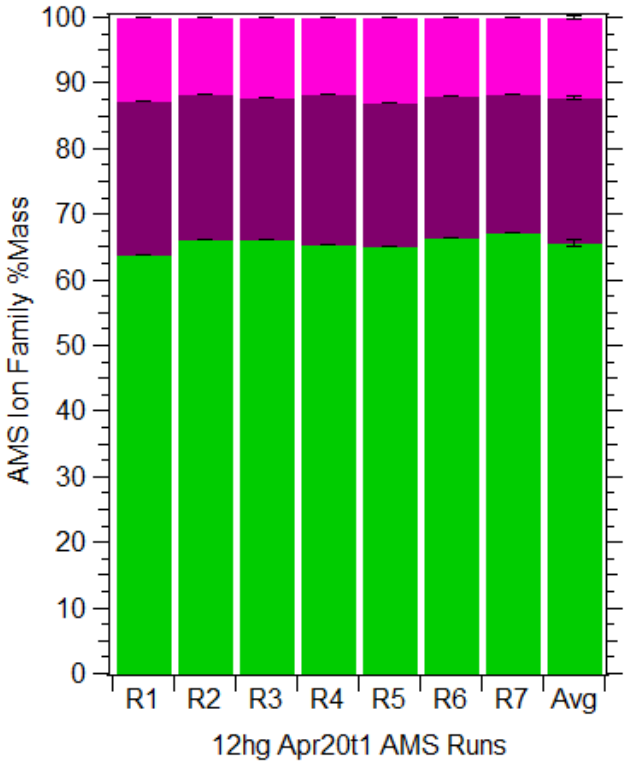

Figure 15. AMS data point reproducibility bar chart. Adjusted Ion Family Compositions for all data points in the AMS run. AMS was run on April 20, and was trial 1 of 12-hour hydrochar, batch 05/30. Ion family compositions for CH, CHO1, and CHOgt1 ranged 63.8-67.2 %, 21.1-23.5 %, and 11.6-12.9% respectively. Included is the average of the runs, and the error bars for the average range one standard deviation for the ion family masses.

The sample variability was clearly much smaller than the data point variability, which indicates that a single sample from within a batch of hydrochar is sufficient for reliable use of the AMS to quantify changes in the mass spectra of hydrochar.

The batch variability is seen in Figure 17. The composition is clearly very different between the 12-hour hydrochar batch run on Feb10 (06/08) and the batch run on Apr20 (05/30), with CH/CHO1/CHOgt1 contents ranging 6.8%, 1.3%, and 5.6% respectively. The most surprising difference is in the CHOgt1 composition, which varies sharply from 6.4% of the composition for the Feb10 trial (06/08 batch) to 12.0% for the Apr20 (05/30 batch).

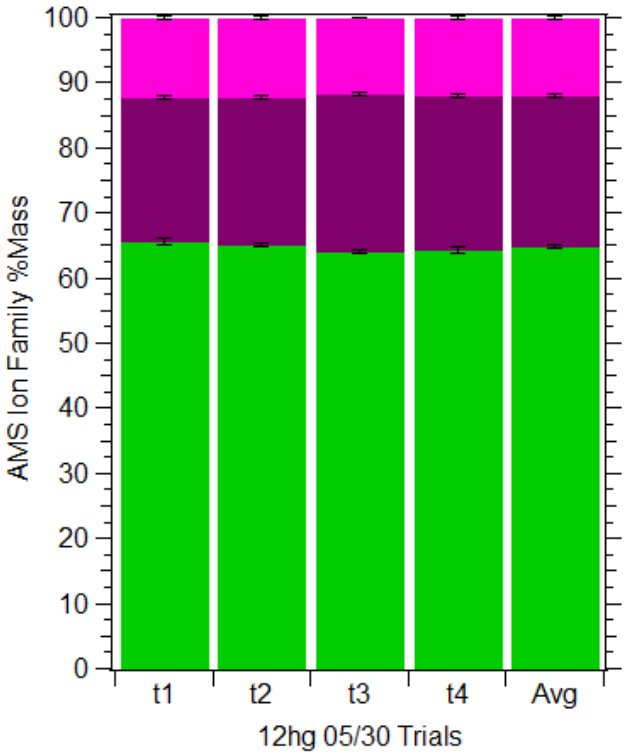

Figure 16. AMS sample reproducibility bar chart., showing adjusted ion family compositions for all data points in the AMS run. AMS was run on April 20, and was for 4 samples of 12-hour hydrochar, batch 05/30, run on April 20 on the SP-AMS. Ion family compositions for CH, CHO1, and CHOgt1 ranged 64.0-65.7 %, 22.2-24.1 %, and 11.8-12.2% respectively. Included is the average of the runs, and the error bars range one standard deviation for the ion family masses.

Clearly the batch variability is the most significant source of uncertainty. This is level of variability is also seen in the Elemental Analysis with a 12 hour standard deviation in CHO mass composition (between 3 batches) of 1.4 %, 0.2 %, and 1.4 % (for a composition of 69.2 %, 4.3 %, and 26.5 %). Since the batch variability is the largest source of variability the range in values between the 12hg Apr20 runs and the Feb10 runs is used for the error bars in the ion trends.

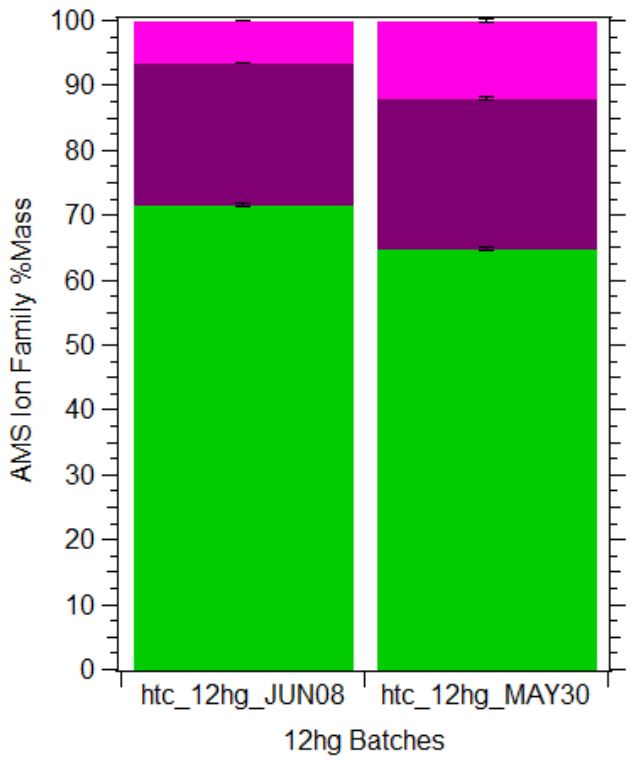

Figure 17. AMS batch reproducibility bar chart, showing adjusted ion family compositions for the AMS trials of two hydrochar batches prepared under the same reaction conditions. The two hydrochar batches were 12-hour hydrochar prepared on 06/08 and 05/30. The 06/08 batch was run on the mass spectrometer on Feb10, trial 1. The 05/30 batch was run on April 20, with 4 trials (t1-t4) averaged together. Ion family compositions range 6.8 %, 1.3%, and 5.6% for the CH, CHO1, and CHOgt1 ions respectively.

Analysis

Ion Families

The ion families that are attributed to char are as follows: Cx, CH, CHO1, CHOgt1, and HO. Other ion families are detected, but in smaller quantities. Cx family contains only carbon ions ($^{12}C_1^+$, $^{13}C_1^+$, C_2^+, C_3^+, etc.). CH ions are of the form C_xH_y, containing only carbon and hydrogen, while CHO1 and CHOgt1 are of the form C_xH_yO and $C_xH_yO_z$ respectively, but the CHO1 and CHOgt1 do not have to have hydrogen necessarily. HO contains O, HO, and H_2O, as well as the isotope forms. The hydrochar spectra are the combination of all of the ion families, scaled to unity.

Peak Assignments

The SP-AMS and its software program makes it possible, and quite easy, to attribute peaks on a mass spectrum to specific ions. At a given integer mass value many bands can be fit to the same integer peak, and the high-resolution spectrometer on the SP-AMS can give an acceptable fit at low m/z values. The problem then arises with how to connect a specific ion to the chemistry of the hydrochar. For example, a peak at m/z=43, C_2H_3O, could come from a ketone or an alcohol or an aldehyde, but it is not immediately clear what functionalities are strongly associated with this ion, and which ones are only weakly associated. In addition, a given peak could be a secondary peak (a peak of secondary importance) from another ion family. Therefore, it is necessary to compare the mass spectra of hydrochar to organic compounds to understand the quantitative significance of given peaks.

In order to understand the significance of the mass spectra of hydrochar, some NIST compounds related to hydrothermal decomposition of glucose (levulinic acid and 5-HMF), furanic structures (furfural and 5-HMF) and aromatic (arene) compounds (benzene, toluene, and indene) were studied for their mass spectra patterns. Levulinic acid has a substantial peak at m/z=43, and a minor peak at m/z=55. By studying the mass spectra of aliphatic alcohols and ketones, it is clear the m/z=43 peak is C_2H_3O, and is seen in primary alcohols and primary ketones. m/z=55 is C_3H_3O, and also forms from the ketone. Furfural, by comparison, shows two equally strong primary peaks at m/z=95 and 96, with formulas of $C_5H_3O_2$ and $C_5H_4O_2$ respectively. This indicates that the furan peak remains intact during ionization. In 5-HMF, the furan ring remains intact with a major band at m/z=97, with other bands at m/z=126 and 41.The aromatic compounds by comparison do not fragment as widely as the others. Benzene has its major peak at m/z=78, while for toluene it is located at m/z=91 and 92. Indene has its major peaks at m/z=115 and 116.

Elemental Composition

The elemental composition of the hydrochar can be reasonably calculated based off the mass spectra, assuming that the ionization efficiencies are the same for organic carbon fragments. Calculating the

elemental composition was done by summing the amount of carbon, hydrogen, and oxygen for the most significant ion fragment of each ion family at all m/z's in the range considered.

The organic mass spectra is equal to the sum of the mass fractions at each integer m/z value, j_{mz}:

$$1 = \sum_{mz=12}^{115} j_{mz}$$

Similarly, the mass spectrum can also be analyzed from the perspective of the individual ion families, F_i.

$$1 = \sum_{i}^{5} F_i$$

The five ion families are Cx, CH, CHO1, CHOgt1, and HO. Since multiple ions often inhabit the same integer m/z value, the two equations shown previous are combined, with a redefinition of the mass fractions at each m/z by the ion family, $j_{mz,i}$:

$$1 = \sum_{i=1}^{5} \sum_{mz=12}^{115} j_{mz,i}$$

To obtain the elemental composition of the mass spectra, the atomic compositions (number of atoms for each element) of the $j_{mz,i}$'s must first be determined. For this, matrix $\bar{n}_{\frac{m}{z},i}$, $\begin{bmatrix} n_{C,\frac{m}{z},i} \\ n_{H,\frac{m}{z},i} \\ n_{O,\frac{m}{z},i} \end{bmatrix}$ is populated. Some of the element values can be automatically entered as the composition by ion family is already determined.

The atomic composition of the Cx ion family is $\bar{n}_{E,Cx} = \begin{bmatrix} n_{C,Cx} \\ n_{H,Cx} \\ n_{O,Cx} \end{bmatrix} = \begin{bmatrix} x \\ 0 \\ 0 \end{bmatrix}$ for a generic ion of formula $C_xH_yO_z$.

For the same generic formula, the atomic compositions $\overline{nE}_i$ are as follows: $\bar{n}_{CH} = \begin{bmatrix} n_{C,CH} \\ n_{H,CH} \\ n_{O,CH} \end{bmatrix} = \begin{bmatrix} x \\ y \\ 0 \end{bmatrix}$, $\overline{nE}_{CHO1} = \begin{bmatrix} n_{C,CHO1} \\ n_{H,CHO1} \\ n_{O,CHO1} \end{bmatrix} = \begin{bmatrix} x \\ y \\ 1 \end{bmatrix}$, $\overline{nE}_{CHOgt1} = \begin{bmatrix} n_{C,CHOgt1} \\ n_{H,CHOgt1} \\ n_{O,CHOgt1} \end{bmatrix} = \begin{bmatrix} x \\ y \\ z \end{bmatrix}$, $\overline{nE}_{HO} = \begin{bmatrix} n_{C,HO} \\ n_{H,HO} \\ n_{O,HO} \end{bmatrix} = \begin{bmatrix} 0 \\ y \\ 1 \end{bmatrix}$. The $\overline{nE}_{m/z}$ values

were determined by the molecules stoichiometry, which can be checked using the HR Peak Fitting Panel in the AMS Software program (Squirrel) in Igor. The panel is shown in Figure X in the Appendix. The peaks that are fit to a given unit mass m/z region are labeled and give the molecular formula. The atomic composition of the fragment is then converted into mass composition, by the following equation: $m_{E,\frac{m}{z},i} = \frac{n_{E,\frac{m}{z},i} * AM_E}{\sum_{k=1}^{3} n_{E_k,\frac{m}{z},i} * AM_{E_k}}$, where AM_E is the atomic mass of E.

The elemental composition on a mass basis is then obtained by the sum of the products of the mass spectra and the mass fractions for the elements C, H, and O, for each ion family and each m/z value. This can be expressed by the following: $m_E = \sum_{i=5}^{5} \sum_{\frac{m}{z}=15}^{120} m_{E,\frac{m}{z},i} * j_{mz,i}$.

The elemental composition was calculated for the mass spectra directly obtained from running the mass spectra, along with a variety of conditions to observe the effect on the elemental composition. The "raw" elemental composition is the as-is mass spectra. "no H2O" was formed by zeroing the m/z=18 peak in the HO family (the H_2O+ ion). "no CO and CO2" was formed by zeroing the CO and CO_2 peaks, or the values at m/z=28 in the CHO1 family and m/z=44 in the CHOgt1 family respectively. "Adjusted", or "Adj." was formed by zeroing the H_2O, CO, and CO_2 peaks. This approach zeroes the largest three peaks in the mass spectrum.

Another approach considered was to scale up the Cx content. It is reported in the literature of aerosol mass spectrometry that the rBC content has a lower ionization efficiency than organic matter, due to its low volatility. Assuming an ionization efficiency of rBC of 20% the signal would have to be scaled by a factor of 5. The rBC content was defined as the entire C3 peak, and some of the C2 and C1 peaks. The amount of C1 and C2 attributed to rBC are defined as 62.5 % and 35 % of the C3 peak respectively. These masses are subtracted from the Cx family, and then multiplied by 5. The elemental composition is then determined. This is called the Aiken5x method. The Aiken20x method assumes a 25% collection efficiency

along with the original 20% ionization efficiency, and the rBC content is therefore multiplied by a factor of 20 as opposed to the factor of 5 mentioned previously. The Aiken20xhalfHO method scales the rBC content by a factor of 20 while also reducing the HO content by 50%.

Error Calculations

Error bars were calculated for ratios of two peaks against each other, and for peaks that were a fraction of the mass loading. Since there is error in the mass loading and in any given species, the following equation was used to determine the new error:

$$\sigma^2_{\frac{\bar{x}}{\bar{y}}} = \sigma^2_{\bar{x}} * \frac{1}{\bar{y}^2} + \sigma^2_{\bar{y}} \left(\frac{\bar{x}}{\bar{y}^2}\right)^2$$

Where σ^2 is variance, while σ is standard deviation. $\bar{x}$ is the average value of species x.

The values input into this equation are the standard deviations and averages of either the total mass loading, the adjusted mass loading, or the mass loading of a given ion species. The total mass loading is the sum of the Cx, CH, CHO1, CHOgt1, and HO ion families using the High-Res AMS calculations (Pika). The Adjusted mass loading is the total mass loading minus the HO ion family and the CO^+ and CO_2^+ ions. The individual ions that were recorded (also using the Pika HR analysis package) were the following:

CH ions

Aliphatics: CH_3, C_2H_5, C_3H_7, C_4H_9, C_5H_{11}

Olefins: C_2H_3, C_3H_5, C_4H_7, C_5H_9

Aromatics: C_6H_5, C_7H_7, C_9H_7, $C_{10}H_8$, $C_{11}H_{10}$, $C_{12}H_8$, $C_{14}H_{10}$

Other: C_3H_3, C_4H_3, C_4H_5, C_5H_3, C_5H_5, C_6H_7O

CHO1 ions: CO, CHO, CH_3O, C_2H_3O, C_3H_3O, C_5H_5O

CHOgt1 ions: CO_2, $C_5H_3O_2$, $C_5H_4O_2$, $C_5H_5O_2$

The 12-hour point combines four runs, while all other time points are from one run each. Since one of the runs has a different mass loading to the other three, the standard deviation would be much larger than the other runs. To account for this, an averaging is used:

$$\sigma^2_{12-hour\ Avg} = \frac{\sigma^2_{12hg\ t1} + \sigma^2_{12hg\ t2} + \sigma^2_{12hg\ t3} + \sigma^2_{12hg\ t4}}{4^2}$$

The error bars are calculated using the confidence function. The confidence function uses the standard deviation, number of points sampled, and the confidence rating. For samples with a known standard deviation, the confidence interval is:

$$(\bar{x} - z^* \frac{\sigma}{\sqrt{n}}, \bar{x} + z^* \frac{\sigma}{\sqrt{n}})$$

Where $\bar{x}$ is the average value of x, σ is the standard deviation, n is the number of runs, and z^* is the critical value, which is a function of the confidence rating and the number of samples. For a confidence rating of 95% with 10 data points, the z^* is 1.833.

Results and Discussion

The results of the study of hydrochar properties begins with the bulk properties of the char, its mass yield and elemental composition as a function of reaction time. These changes can indicate the relative magnitude of changes expected with the chemistry of the material, but small changes in bulk properties do not necessarily mean small changes in chemical properties. Generally, all of the trends show the changes with reaction time are most significant at the earliest reaction times, and decreases afterwards.

Hydrochar yield

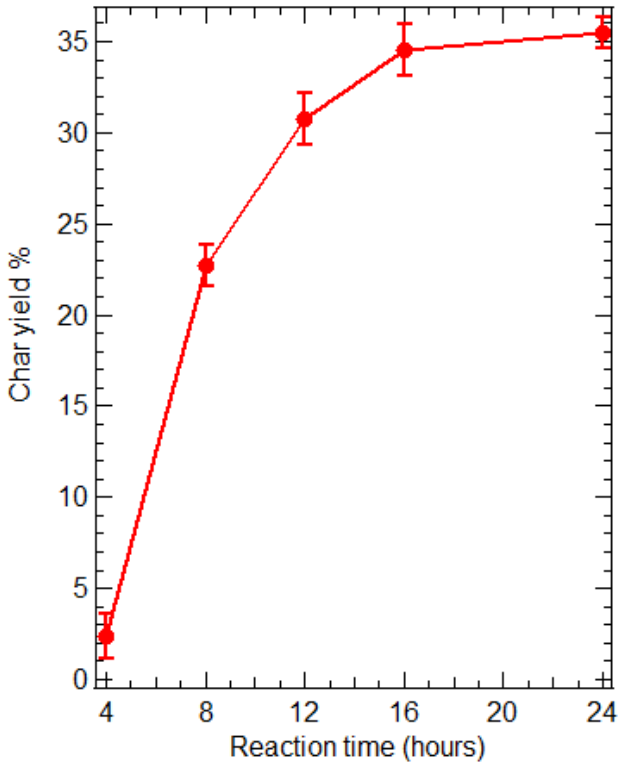

Figure 18. Hydrochar percent mass yield as a function of reaction time. Char yield is the mass of char relative to the initial mass of sugar. Error bars are the confidence interval (with a 95% confidence rating) for the 3-5 samples at each time point.

The yield of hydrochar is shown in Figure 18 and in the Appendix in Table 7. The yield is the lowest at 4 hours and increases up to 24 hours, with the rate of yield decreasing with reaction time after 4 hours. The difference from 4 to 8 hours is a significant ten-fold increase in yield from 2 % to 23 %. The yield continues

to increase even at 24 hours reaching 36 %, but the trend is starting to level off, with the yield at 16 hours reaching 35 %.

Elemental Analysis

The elemental analysis showed no change in the molar hydrogen content, a decrease in the molar oxygen content, and an increase in the molar carbon content, indicating that a combination of dehydration and decarboxylation reactions take place.

The elemental composition of hydrochar as a function of reaction time is shown in Figure 19, left. Not shown is the raw hydrochar elemental compositions, which are in the Appendix. The sum of the oxygen, hydrogen, and carbon content measured is around 93-95%, which is a function of the technique itself, which measures the carbon and hydrogen contents and the oxygen content in separate procedures. The atomic oxygen fraction appears to decrease with reaction time, dropping from around 15 % to 14 %. The atomic hydrogen content doesn't appear to show a trend with reaction time, with no significant difference between any of the time points. The atomic carbon content increases from 47.5 % to 48.5 % from 4 hours to 24 hours. The change indicates a mixture of dehydration reactions ($-H_2O$) and decarboxylation reactions ($-CO_2$). If it was around 1:1 dehydration and decarboxylation, the oxygen content would decrease, the hydrogen content would remain constant, and the carbon content would decrease. The elemental composition is also shown in the van-Krevelen diagram in Figure 19, with the 3 samples of the 12-hour hydrochar that were tested. The 24-hour point and the 12-hour point S2 are about equidistant to the 12-hour average point, which seems to illustrate that the sample-to-sample variability of the char is substantial and that with this data the stoichiometric changes in the hydrochar cannot be closely scrutinized. However, it would be reasonable to state that the general trend of dehydration (when compared to the glucose precursor) also occurs in the hydrochar after it forms.

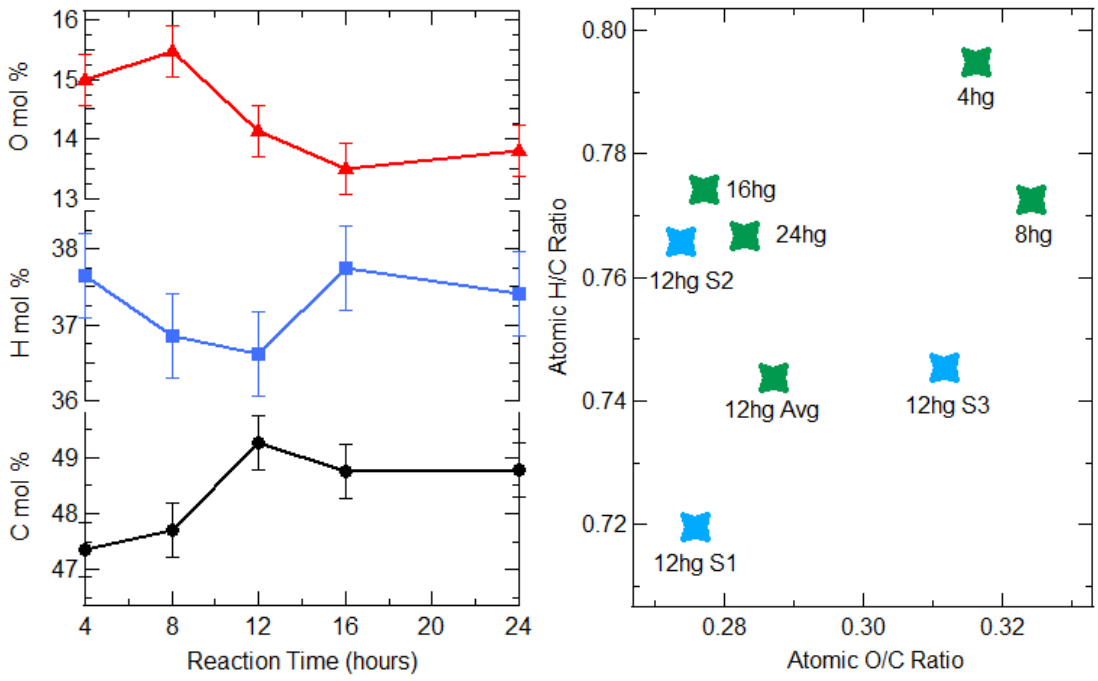

Figure 19. Atomic composition of hydrochar from Elemental Analysis. Left) Changes in molar CHO composition of hydrochar are plotted as a function of reaction time. Error bars are the standard deviations for the three 12-hour glucose samples. Right) van-Krevelen diagram of the hydrochar elemental compositions, along with the three 12-hour glucose samples.

The van-Krevelen diagram of hydrochar compared to the feedstock and other carbon materials is shown in Figure 20, right. Fully carbonized solids are located at the origin of the plot in the bottom left, and changes in hydrogen and oxygen content can be mapped together. The hydrochar samples show a remarkable difference from the glucose feedstock with significantly lower H/C and O/C ratios, dropping from 2 to 0.7 and from 1 to 0.3 respectively. The composition of the hydrochar, compared to the glucose, indicates significant amounts of dehydration reactions took place in the formation of the hydrochar. Glucose, $C_6H_{12}O_6$, goes to an equivalent $C_6H_{4.6}O_{1.8}$. With pyrolysis, the hydrochar O:C ratio decreases from 0.32 to 0.23, while the H:C ratio decreases sharply from 0.77 to 0.31. This change is quite different from the change observed in the glucose with hydrothermal carbonization. While this is indicative of dehydration, it is not only the case. Decarboxylation or aromatization or a combination of reactions may also take place. While the pyrolyzed sample is more carbonized than its starting material, it has significantly higher oxygen and hydrogen content than carbon black.

Comparison to literature values

The hydrochars tested in this study are comparable to the hydrochars tested in the literature, as shown in Table 5. The hydrochars from literature have slightly higher oxygen contents, but are within 2 % for the carbon content. It is important to note that hydrochar composition was close to literature value when the O measurement was ignored and the O composition was determined by difference from the CH measurement. When the O measurement was included the carbon content mass value reported increases from 63.3% to 67.1%, which shows that accurate measurement of the CHO composition should be done by measuring the O content, not by determination by subtraction.

Table 5. Comparison of hydrochar elemental mass composition by elemental analysis to literature values. While O was measured separately in this study, other studies found O by difference (not by a measurement), so the O measurement in this study is omitted here, and calculated by difference from the raw mass % C and H reported.

Conditions	C/H/O	O/C	H/C	Ref
HTC: Glucose feed, T=180°C, t=4 hr, C_0=253.4 g/L	63.2/4.2/32.6	0.386	0.795	This Study
Humins: Glucose, 2 M soln., 220°C, 0.1 M acid, 6 hours		0.36	0.79	[82]
HTC: Glucose feed, T=170°C, t=4.5 hr, C_0=90 g/L	64.91/4.20/30.89	0.357	0.776	[18]
HTC: Glucose feed, T=180°C, t=12 hr, C_0=253.4 g/L	65.25/4.04/30.71	0.35	0.74	This Study
HTC: Glucose feed, T=180°C, t=12 hr, C_0=111.1 g/L	64.47/4.69/30.84	0.36	0.87	[77]
Pyr-HTC: Feed: 8hg Pyr-T: 500°C, t=10 hr Atmosphere: N_2	68.72/1.77/29.51	0.32	0.31	This Study

Pyr-HTC: Feed:12hg Pyr-T: 550°C, t=6 hr Atmosphere: N_2	84.66/2.83/12.51	0.11	0.40	[77]

The elemental composition of hydrochars, with respect to the starting material as well as related carbon materials is shown in Figure 20. The starting material, glucose, is in the top left corner, with a known elemental composition of H/C and O/C ratios of 2 and 1 respectively. The hydrochars appear around a composition of 0.7 and 0.3 for H/C and O/C respectively, and appear very close to the dehydration trend line running through the glucose composition to the point of a perfect carbon material. From this it is clear that the predominant type of reaction occurring to the glucose under hydrothermal carbonization is a dehydration reaction. However, while the carbon content does increase with reaction time, it is not as clear as the change seen in the glucose as it is reacts under hydrothermal conditions. The hydrochar differs significantly from the pyrolyzed hydrochar, which has a slightly lower oxygen content and a significantly lower hydrogen content.

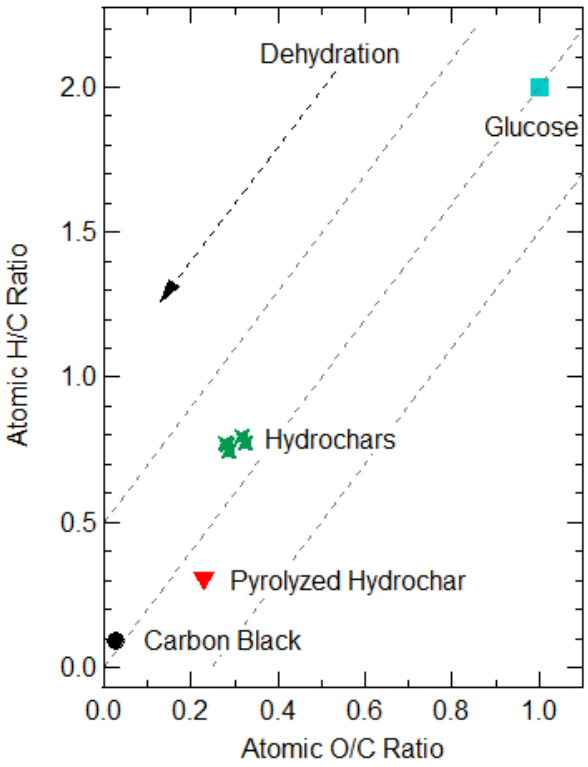

Figure 20. van-Krevelen diagram of hydrochars and glucose, with pyrolyzed hydrochar and carbon black for comparison. The dashed lines indicate changes in the stoichiometry consistent with dehydration reactions.

IR Spectroscopy

The IR Spectroscopy technique identifies methyl, alcohol, and carbonyl functionality along with furan and arene rings. The IR methods show the methyl and arene contents increase while the alcohol, carbonyl, and furans decrease with reaction time.

DRIFTS Method

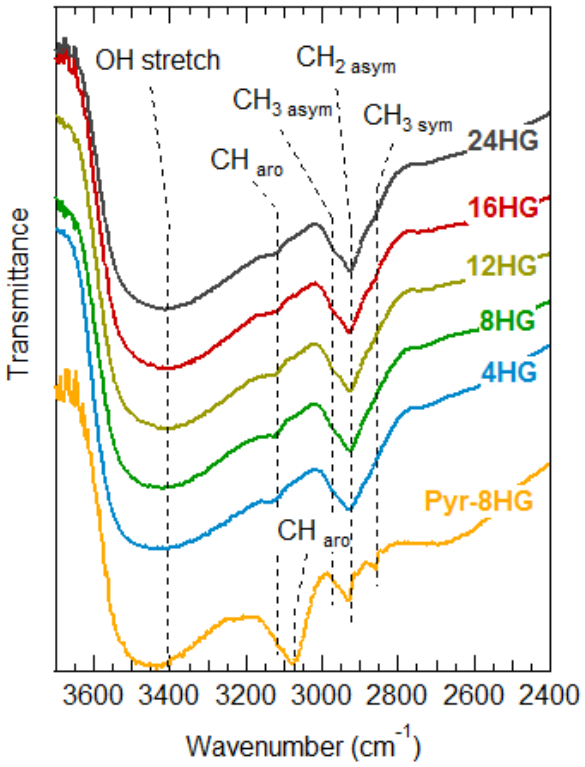

Figure 21. DRIFTs spectra of hydrochar and pyrolyzed hydrochar with varying reaction times. Spectra were normalized for equal area under the curve across the range 3700-2400 cm^{-1}. Spectra were taken at 150 °C, after drying for 1 hour under nitrogen atmosphere.

The DRIFTs spectra of hydrochar are shown in Figure 21. The spectra show a broad absorbance at 3400 cm^{-1}, which is attributed to the OH stretching mode. The band at 3120 cm^{-1} is assigned as the furan CH stretching mode, based on the assignment by Chuntanapum and Matsumura [41]. The furan CH stretching mode is not observed in the spectra of hydrochar prepared under similar conditions in a study by Sevilla and Fuertes [18]. Here, the sample was dried at 150 °C for 2 hours under nitrogen to remove any residual water that overshadows the spectra in that region. At 2900 cm^{-1} there is a broad stretch which contains the aliphatic CH stretching modes for CH_3 symmetric, CH_2 asymmetric, and CH_3 asymmetric at 2870, 2930, and 2960 cm^{-1} respectively, according to Timko et al. [64]. These assignments agree well with the positions suggested by El-Bassoussi et al. [80]. The CH_3 asymmetric stretch sharpens with increasing reaction time, indicating better defined methyl sites.

With pyrolysis however, clear differences emerge in the spectra relative to the precursor, the 8hg sample. With pyrolysis, the OH stretch shifts from 3400 to 3450 cm^{-1}. The CH aromatic stretch drastically increases, with a shift in position from 3120 to 3075 cm^{-1}, due to an increase in the aromatic carbon content. It could be argued that a 2nd absorbance grows in at 3075 cm^{-1}, as opposed to a shift in position of the 3120 cm^{-1} absorbance accompanied by a shift in intensity. The aliphatic CH region at 2900 cm^{-1} appears to be split in half, with the CH_3 symmetric separated from the CH_3 asymmetric and CH_2 asymmetric. Further, the peaks appear to be sharper in the pyrolyzed sample than in the hydrochar, with better definition of where peaks start and end. This indicates that the aliphatic carbons are more uniform in the pyrolyzed material than the original. The broad, weak absorbance at around 2700-2750 cm^{-1} which is not observed in the hydrochars is simply due to the background. The DRIFTs spectra further indicates an increase in the aromatic carbon fraction after pyrolysis, with the aromatic CH stretch drastically increasing in intensity.

KBr Transmittance Method

The lower mid-IR region is shown in Figure 22. The C=O stretch appears at 1705 cm^{-1}, while the C=C stretch appears at 1610 cm^{-1}. The C=C stretch can be attributed to furanic carbon, with van Zandvoort et al. in a study of humins found a broad, deep C=C stretch at 1605 cm^{-1}, and the ^{13}C-enriched humins IR showed a shift consistent with C=C stretching . The band at 1515 cm^{-1} is attributed to furan [64, 83-84]. The furan peak at 1515 cm^{-1} appears to decrease in intensity with reaction time, indicating a decreasing furan content with reaction time.

The region of 1450-1050 cm^{-1} contains many small peaks, which could be attributed to a variety of vibrational modes including aromatics. Bands appear at 1450, 1360, 1305, 1210, 1160 (only at 4 hours), and 1075 cm^{-1} in this region. The 4-hour spectra also has bands at 1400 and 1160 cm^{-1} which are not seen at the other time points. The band at 1450 cm^{-1} could very likely be the CH_3/CH_2 asymmetric deformation band, which is observed in petroleum residue at 1485-1445 cm^{-1} [80].

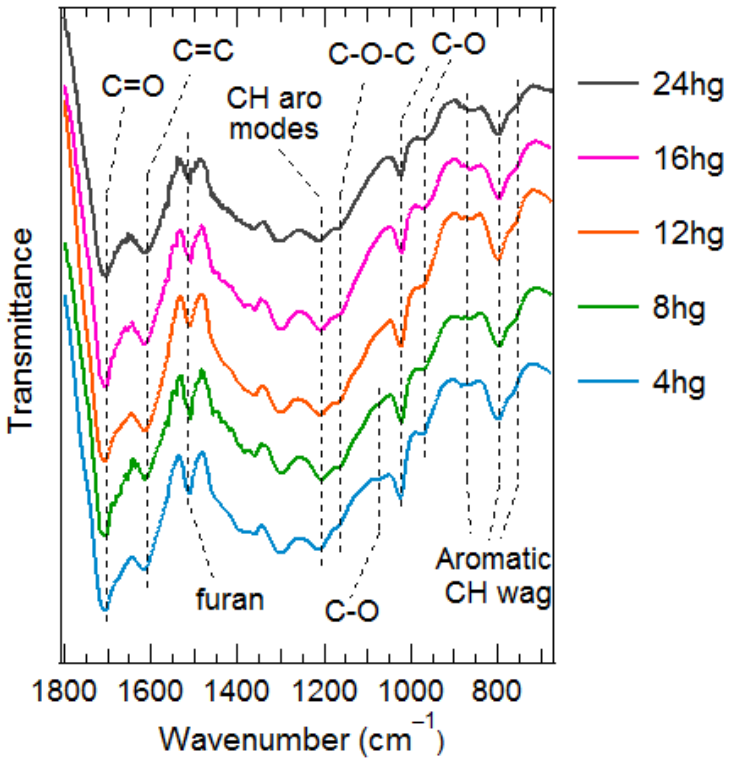

Figure 22. Transmittance-mode IR spectra of hydrochars. Plotted over the lower mid-IR region, where transmittance mode has better resolution than DRIFTs. Spectra are normalized to have equal area under the curve from 1800 to 675 cm^{-1}.

The shoulder at 1400 cm^{-1} in the 4 hour spectra, which appears to be a small, steeply sloped section, does not appear in the other spectra shown. This peak cannot be attributed with confidence. The band at 1075 cm^{-1} appears at 4 hours and disappears completely by 16 hours, which could be attributed to an ether stretch or a type of C-O stretch. The band at 1360 cm^{-1} could be CH_3 symmetric deformation and CH symmetric bending, based on petroleum residue locations [80]. The significant band at 1305 cm^{-1} cannot be easily assigned. In an IR reference text, Socrates assigns primary alkyl alcohols (-CH_2OH) to 1440-1260 cm^{-1} [92], however, in the IR of hydrothermally treated algae, there is a substantial OH stretch but no band at 1300 cm^{-1} [61]. IR spectra of hydrochar in studies by Sevilla and Fuertes [18, 54] had such a peak at 1300 cm^{-1}, but it was attributed to C-O stretching in hydroxyl, ether, or ester and O-H bending vibrations. This was justified by the observation that the region decreased in intensity with the hydrothermal degradation of cellulose. The strength of the absorbance as a C-O bond justifies this assignment, as opposed to alkyl

vibrational modes. The band at 1210 cm^{-1} is also quite significant, and an assignment as C-H aromatic group modes has been proposed by Timko et al. in a study of hydrochars [64]. It could also be phenol, which has been reported in a study of humins [83].

The band at 1030 cm^{-1} is attributed to furan [82], and is believed to be a C-O stretch [64]. Patil et al. noted that the band is retained in the humins from 5-HMF in the furan ring or the hydroxymethyl group.

The CH aromatic out-of-plane wagging modes are present at 865, 800, and 760 cm^{-1}. El-Bassoussi et al. attributed the bands to aromatics with varying degrees of substitution, with increasing substitution at higher wavenumbers. The band at 865 cm^{-1} appears to shift to lower wavenumbers with reaction time, while the band at 760 cm^{-1} appears to decrease relative to the band at 800 cm^{-1} with increasing reaction time. This could indicate that there is a slightly higher degree of substitution in the char with increasing reaction time.

The qualitative changes in the spectra from 4 to 8 hours are seen with the disappearance of the peaks at 1400 and 1160 cm^{-1}. The changes in the composition of the char with reaction time, a trend of increasing carbon content, could be indicative of a decrease in the C-O functionality with reaction time. These changes are significant as they occur when the yield of the char drastically changes, which indicates that the char that first forms has slight qualitative differences from the char that forms in bulk.

Conclusions

While IR can identify functionalities present in the hydrochar, the technique is not quantitative (either comparing one peak to another, or comparing the same peak in different materials). The IR spectra of hydrochar identifies alkyl content with the CH_2 stretches and CH_3 stretch. Functional groups are identified with the hydroxyl H-O stretch, C-O modes which indicate hydroxyl and ether groups, and phenol. Furan modes are identified, with the furan C-H stretch and modes at 1520 and 1030 cm^{-1}. Finally, aromatic

modes are also observed, with the C=C stretch at 1610 cm^{-1}, and the C-H out-of-plane modes at 875-750 cm^{-1}.

Small changes are also observed in the IR with reaction time. The CH_3 stretch sharpens with reaction time, indicating more chemically uniform sites. The C=C stretch at 1610 cm^{-1} increases with reaction time indicating a greater aromatic content, while the furan mode at 1520 cm^{-1} decreases with reaction time, indicating a decreasing furan content. With reaction time, the ether mode at 1070 cm^{-1} decreases, while the C-H out-of-plane modes at 875-750 cm^{-1} shift to lower wavenumbers.

Raman Spectroscopy

The Raman Spectroscopy fitting indicates that the hydrochar contains aldehyde-functionalized 1-ring and 2-ring arenes and aldehyde-functionalized single-ring furans. The Raman trends with reaction time indicate an increasing 2-ring content relative to 1-ring content.

Raman Spectroscopy, as a technique that is sensitive to aromatic domains in carbon materials, can provide chemical insight that IR Spectroscopy cannot. The technique has been applied to hydrochar previously in the literature [18, 40, 60-61, 64, 93], but generally the technique is not used beyond tracking the D/G ratio or to simply state that there are aromatic structures in the hydrochar. Additional structural information, such as band intensities for other vibrational modes present, and band positions can also provide structural information. The average Raman spectra of hydrochar prepared at different reaction times are shown in Figure 23, and the spectra are very similar with only fine changes, therefore a fitting method is necessary to characterize changes in the spectra. Fitting methods derived from Brown et al. were applied to the Raman spectra, with two fitting methods compared which either fixed all band positions or sequentially varied the G band, D band, and Kekulé to observe position changes. The two methods are analyzed in the results section, to determine if band positions could be realistically tracked using the current fitting method, as the additional variables may over fit the spectra.

Stationary Fitting

The Stationary assignments and method were applied to hydrochar, and a representative fitting of an average Raman spectra is shown in Figure 24. This method fits the Raman spectra well with an average residual sum of least squares r^2 value of 0.9962.

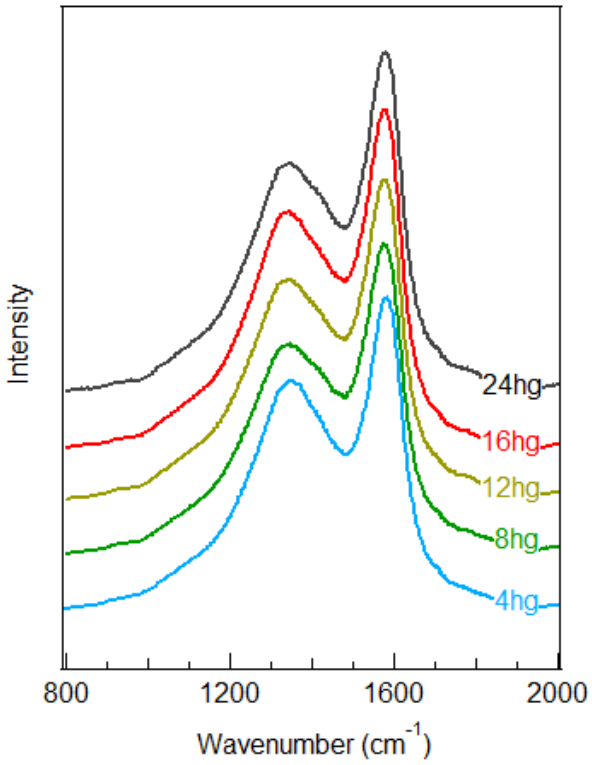

Figure 23. Average Raman spectra of hydrochars prepared at different reaction times. Spectra are normalized by peak area from 1000-1750 cm^{-1} and offset equally.

Since the Raman spectra were not expected to change significantly in positions or shape, the method lowers the number of independent variables in the fitting method, which prevents overfitting [94]. The largest peaks are the G band, D band, Br_R, and Kekulé in that order. The method fits the Raman spectra across the range of 1000-1750 cm^{-1}, but at the ends of the fitting it is not zero, and it appears that the residual is much larger at the higher wavenumber side, which is a result of the baseline subtraction method. The method could result in a relatively larger carbonyl (C=O) peak with a relatively lower Br_L, but more importantly the condition is applied relatively uniformly so trends with reaction time can be quantified.

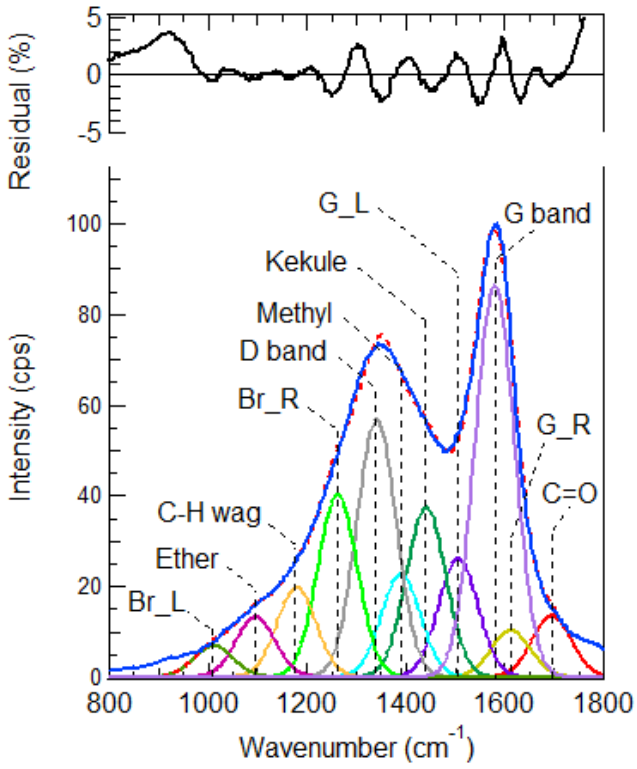

Figure 24. Stationary fit method applied to the average 4-hour hydrochar Raman spectra. Shown in the bottom part are the raw Raman spectra (blue), the sum of fits curve (orange dashed curve), and the Gaussian fit curves. On the top of the graph is the residual of the fit (the difference of the raw spectra with the sum of fits, shown in black). The maximum intensity is scaled to 100% for the Raman spectra. The average Raman spectra did not fit a CH_2/CH_3 peak, so it is not shown.

The change in Raman fit peak area by the stationary method for the D band and the related breathing modes (Br_R and Br_L) and the G band and the related asymmetric modes (G_R and G_L) are shown in Figure 25. The G band is the largest by area, followed by the G_L and then the G_R. The G band increases with reaction time, with the largest change between the 4 and 8 hour points. The G_L band shows a similar pattern to the G band, which is expected given their proximity and that they come from similar vibrational modes. The G_R band, however, shows a trend that appears to be the inverse of the G band, decreasing with reaction time from 4 to 8 hours, and increasing from 16 to 24 hours. The D band, Br_R, and Br_L are symmetric breathing modes, and unlike the asymmetric breathing modes (G, G_R, and G_L), are separated by other bands, the C-H wag and Ether. The D band does not show a similar trend to the G band, and does

not appear to be significantly increasing with reaction time. Br_R and Br_L do not show strong trends or variability with reaction time.

The D/G trend with reaction time is shown in Figure 26Figure 26, and appears to decrease with reaction time. The D/G ratio drops from 4 to 8 hours, and seems to increase after this point, but remains to be a statistically significant decrease from 4 hours to all points after. The 4-hour D/G ratio is 0.66 and decreases to an average of 0.62. The K/G trend is similar to the D/G, only with less dramatic changes. The K/G value at 24 hours is within the statistical limit of the 4 hour point. The Kekulé band represents the Kekulé mode in polycyclic aromatic hydrocarbons, as well as a Furan vibration mode. The similarity in trends between the two could indicate that the Kekulé band is highly dependent on the arene content, not the furan content.

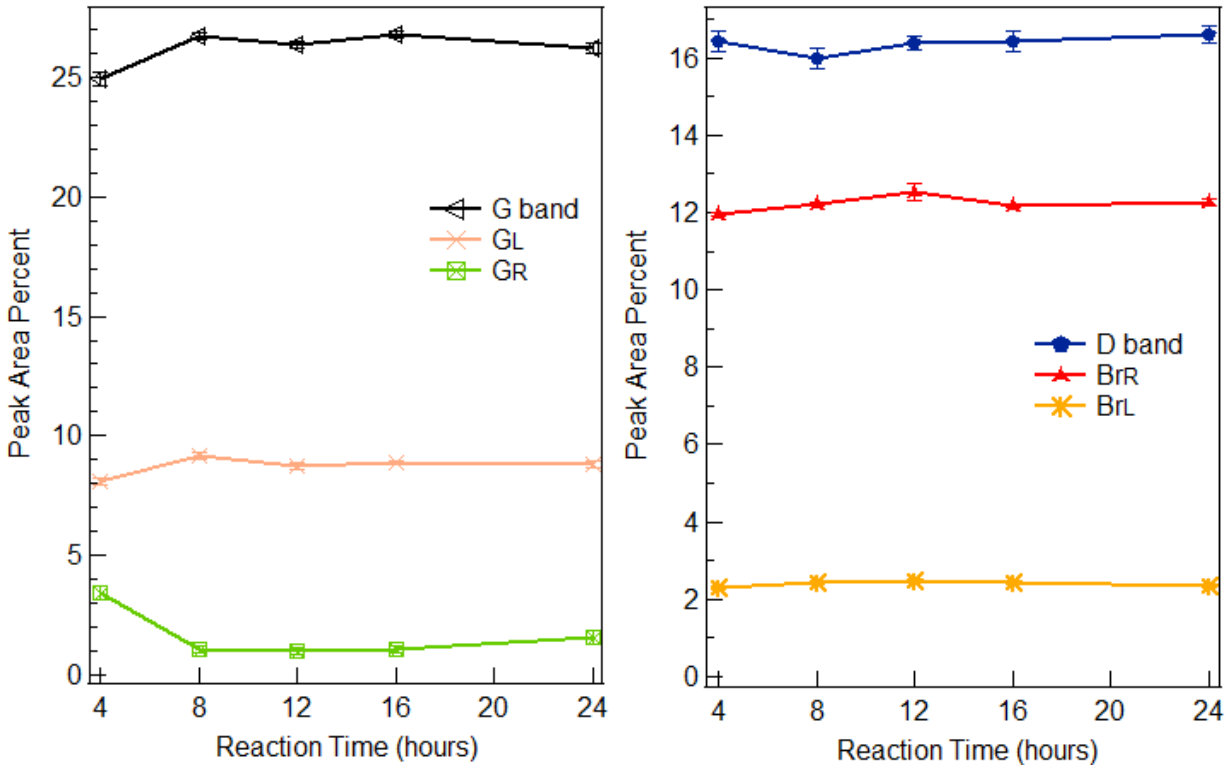

Figure 25. Raman fit peak area of aromatic ring modes related to the D and G modes are plotted against reaction time using the stationary fitting method. Left) Asymmetric Breathing Modes from top to bottom are the G mode, GL, and GR. Right) Symmetric Breathing Modes from top to bottom are the D band, Br_R, and Br_L. Error bars are plotted on both graphs.

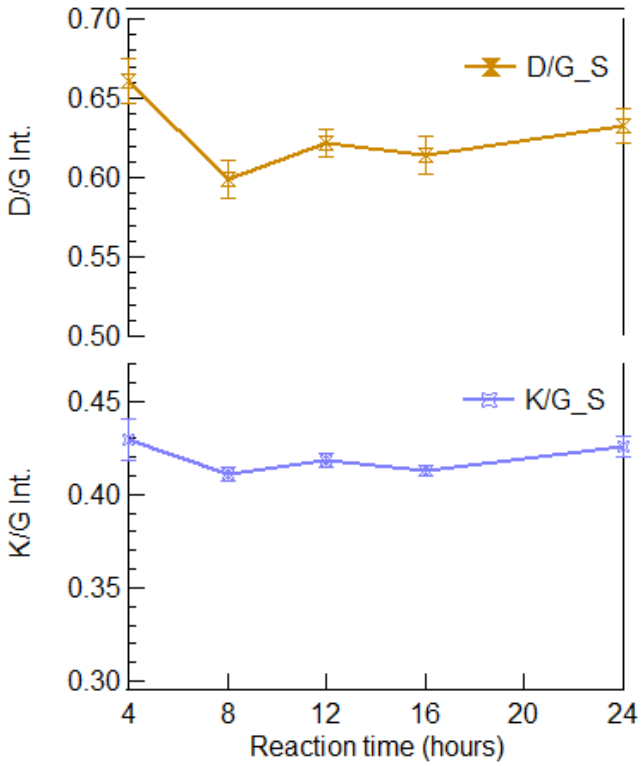

Figure 26. Raman D/G and K/G band intensity ratios as a function of reaction time, determined by the stationary fitting method.

In Figure 27, the methyl, carbonyl, ether, and CH_2/CH_3 peak areas are plotted against reaction time. The methyl band shows strong decrease with reaction time, which also appears to slowly decrease with reaction time. This trend appears to be the inverse of the yield trend with reaction time, despite the large size of the error bars. This trend indicates less methyl groups on the aromatic domains with increasing reaction time. The ether band does not have a distinguishable trend with reaction time, but it closely resembles the shape of the Breathing Res and Breathing mode L modes, which it is located between. The carbonyl band appears to increase with reaction time, which indicates an increasing amount of carbonyl groups (carboxylic acid, ester, aldehyde, and ketone). Finally the CH_2/CH_3 band is the smallest band in fit area, and decreases to zero after 4 hours. This indicates that the alkyl content decreases with reaction time.

The inability to fit the CH_2/CH_3 could be due a variety of factors. First, the noise level in the spectra makes the spectra difficult to fit, especially as the peak is so small. Second, the proximity of the CH_2/CH_3 to the Kekulé could affect the fit, with the bands being separated by 22 cm^{-1}, half the distance normally seen between bands. The CH_2/CH_3 is also the peak located in the lowest part of the valley between the G Peak and the D Peak in the Raman Spectra. When four four-hour hydrochar Raman samples were fit using this method (60 spectra), around 80% of the spectra did not fit a positive value for the CH_2/CH_3 peak. Clearly, the peak cannot be easily fit due to its size, proximity to the Kekulé/furan peak, and its location in the lowest part of the curve.

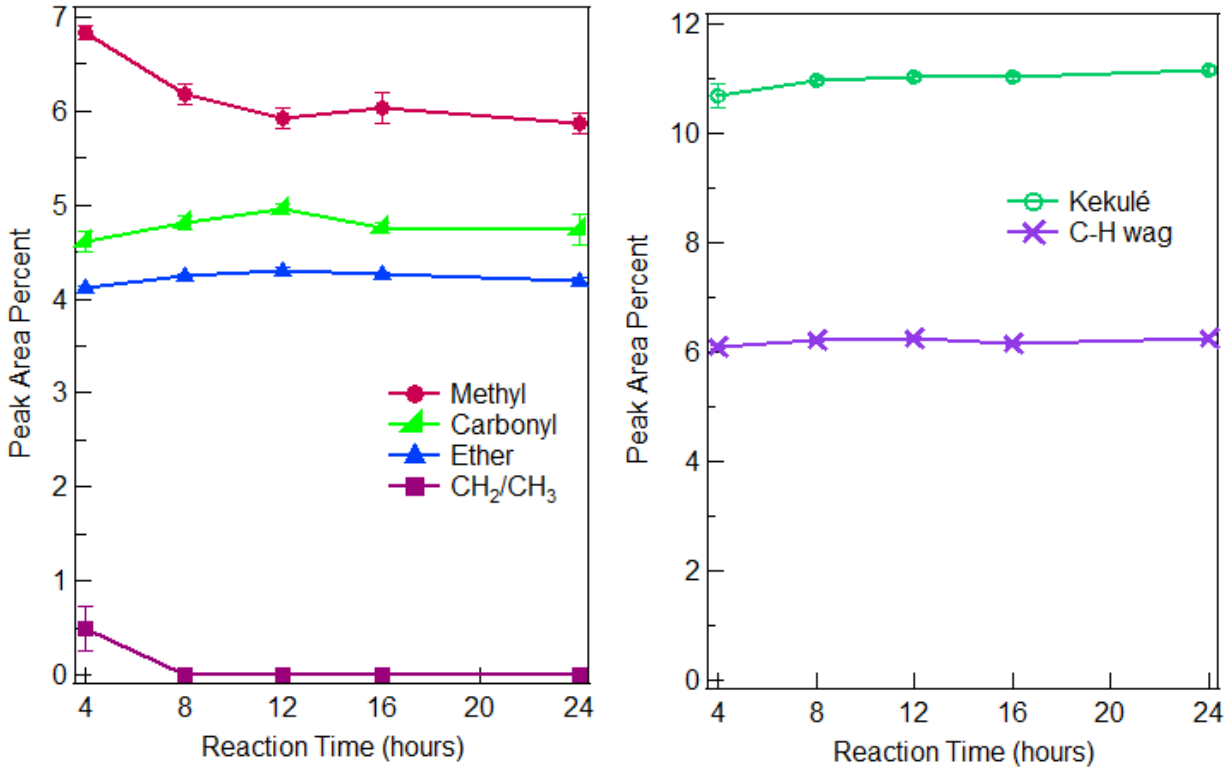

Figure 27. Raman fit peak area of functional group modes (left) and other ring vibration modes (right) plotted against reaction time using the stationary fitting method. Left) Functional group modes, in order of peak area: Methyl, Carbonyl, Ether, and aliphatic mode (CH_2/CH_3). The CH_2/CH_3 is zero for most of the time series. Right) Additional ring-vibration modes, the Kekulé/Furan (called the Kekulé) and the C-H wag in aromatic rings (C-H wag). Error bars are plotted in these graphs.

The trends in the Kekulé and C-H wag are also shown in Figure 27, both showing little change with reaction time. The Kekulé band increases with reaction time, but the change from 4 to 8 hours is not statistically significant. It is expected that the Kekulé band should have a similar trend to the D and G band trends as it is a ring vibration mode, and it is similar.

From the stationary method, the methyl and CH_2/CH_3 bands decrease with reaction time, with the biggest changes seen from 4 to 8 hours. The D/G and K/G also decrease with reaction time. The method has a good r^2 value, but changes in band position with reaction time (or from sample-to-sample) could affect the fitting and cause changes in the relative peak area of different peaks, which is not representative of the actual changes or variability that may exist.

Variable Fitting

The variable method fits the Raman spectra of hydrochar by sequentially allowing the G band, D band, and Kekulé band to shift (in that order). The r^2 of the fit is on average 0.9977, which is higher than that in the stationary method. A representative Raman spectra fit by the variable method is shown in Figure 28. The most striking feature of the new fit is the lack of G_R band and the appearance of the CH_2/CH_3 band, which is larger than in the stationary method. The changes in Kekulé, D band, and G band positions appear to be small, which is expected.

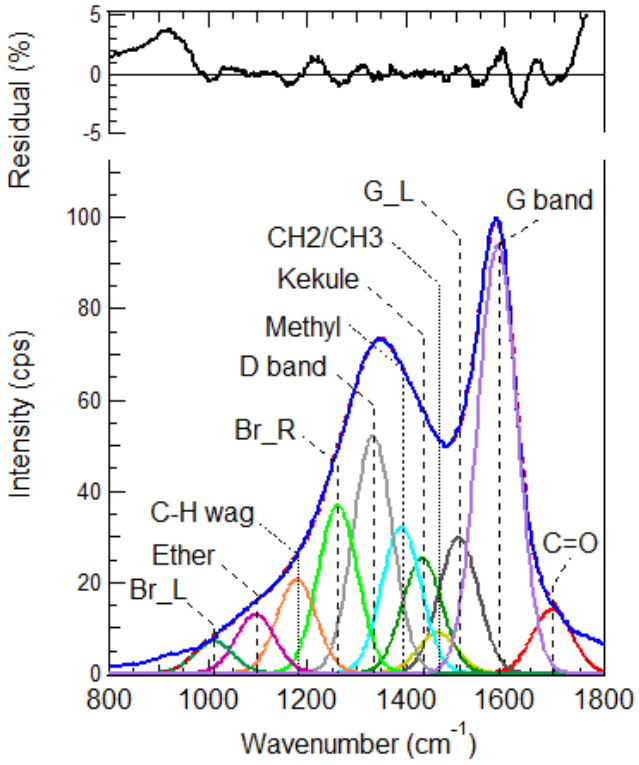

Figure 28. Variable fit method applied to the average 4-hour hydrochar Raman spectra. Shown in the bottom part are the raw Raman spectra (blue), the sum of fits curve (orange dashed curve), and the Gaussian fit curves. On the top is the residual of the fit (the difference of the raw spectra with the sum of fits, shown in black). The maximum intensity is scaled to 100% for the Raman spectra. The average Raman spectra did not fit a G_R peak, so it is not shown.

The trends in peak area of the G and D bands (and the associated peaks) are shown in Figure 29. The G band appears to have a highest area in the 4 hour spectra, and the 8-hour point appears to be the lowest. The G_R trend appears to decrease with reaction time, with almost no fit area, which could be due to the G band shifting closer to the G_R band and obscuring it. The G_L band shows very little variability and almost no trend with reaction time. The D band shows a similar trend to the G band, but the 4-hour point appears to be at a comparable value to the 12-hour and 16-hour points. The Br_R and Br_L do not increase or decrease with reaction time, and show little variability.

The relative change in the D/G and K/G ratios are shown in Figure 30. The D/G ratio appears to slightly increase with reaction time from 4 to 12 hours with values of 0.56 and 0.57 respectively, and remains constant from 16 to 24 hours. The error bars of the 4 and 12 hour points overlap and the trend is not

statistically significant. The K/G ratio trend, by contrast, is much more uneven, but is a statistically significant increase with reaction time (between the 4 and 8 hour points). Brown et al. determined the K/G ratio for polyaromatics, and determined the trend to be generally decreasing in intensity with increasing number of rings, but as the K/G ratio is zero for a 1 ring aromatic, the K/G increases from 1 ring to 2 rings. The implications of the K/G trend is consistent with the D/G.

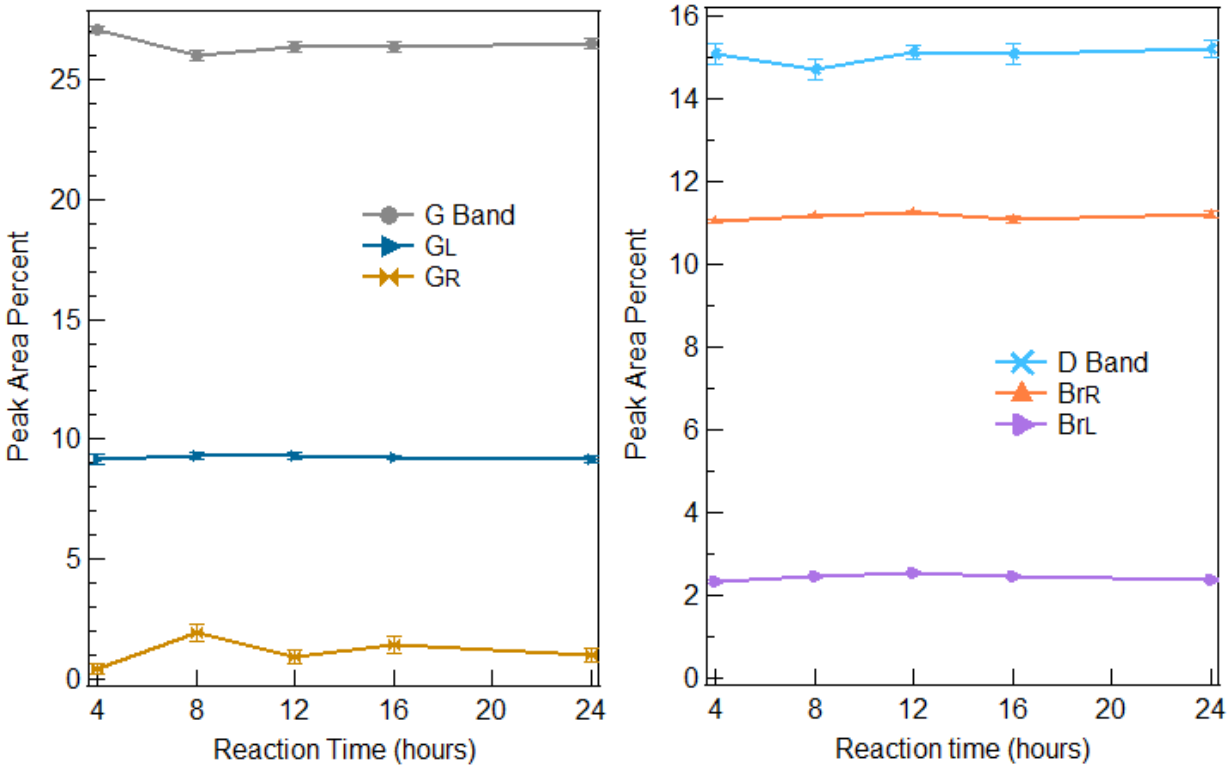

Figure 29. Raman fit peak area % of breathing modes using the variable method, plotted against reaction time. Plotted from top to bottom are the G mode, G-Resonance mode, Kekulé, Asymmetric modes, and C-H out of plane wagging. The confidence interval is plotted for the five species.

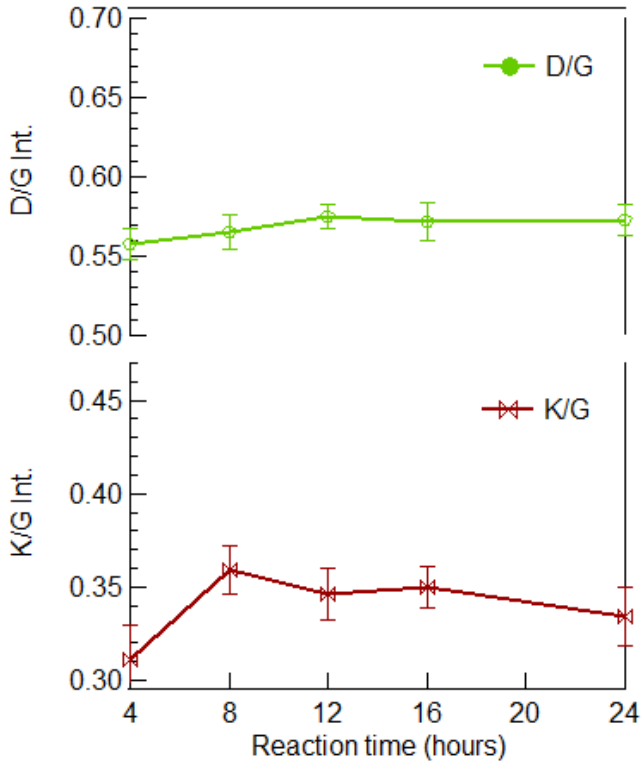

Figure 30. Raman D/G and K/G band intensity ratios as a function of reaction time, determined by the stationary fitting method.

The fit of the functional groups (Methyl, Carbonyl, Ether, and CH_2/CH_3) are shown in Figure 31. The Methyl band shows a statistically significant decreasing trend with reaction time, which was also observed in the stationary fitting method. The carbonyl does not appear to increase or decrease with reaction time. Similarly the Ether band does not appear to show a trend with reaction time, remaining constant. The CH_2/CH_3 trend does not have a statistically significant change, but shows a large amount of variability, especially for such a small peak. In the stationary method, the CH_2/CH_3 appears as a small peak at 4 hours before dropping to zero for the other time points. Here, a similar drop is seen, but the CH_2/CH_3 is greater than zero and this method seems to indicate that there more of a constant CH_2/CH_3 seen at all reaction times.

In this fitting method, after fitting for the G, D, and Kekulé positions, usually both the G-Resonance and the CH_2/CH_3 would be negative. The larger peak of the two was locked to zero, and the fitting method was

repeated. This condition makes the CH_2/CH_3 and G-Resonance peak areas dependent on one another. While the CH_2/CH_3 and G-Resonance seem to be dependent, the uncertainty is much larger for the CH_2/CH_3 peak. The uncertainty in the CH_2/CH_3 is so large, it doesn't appear to have a distinguishable trend. The Kekulé and CH wag trends do not appear to be statistically significant, and the Kekulé trend appears to be the inverse of the CH_2/CH_3, which is justified by their proximity and the variability in Kekulé band position as well, which also have an outsize effect on the fit of the adjacent CH_2/CH_3 band.

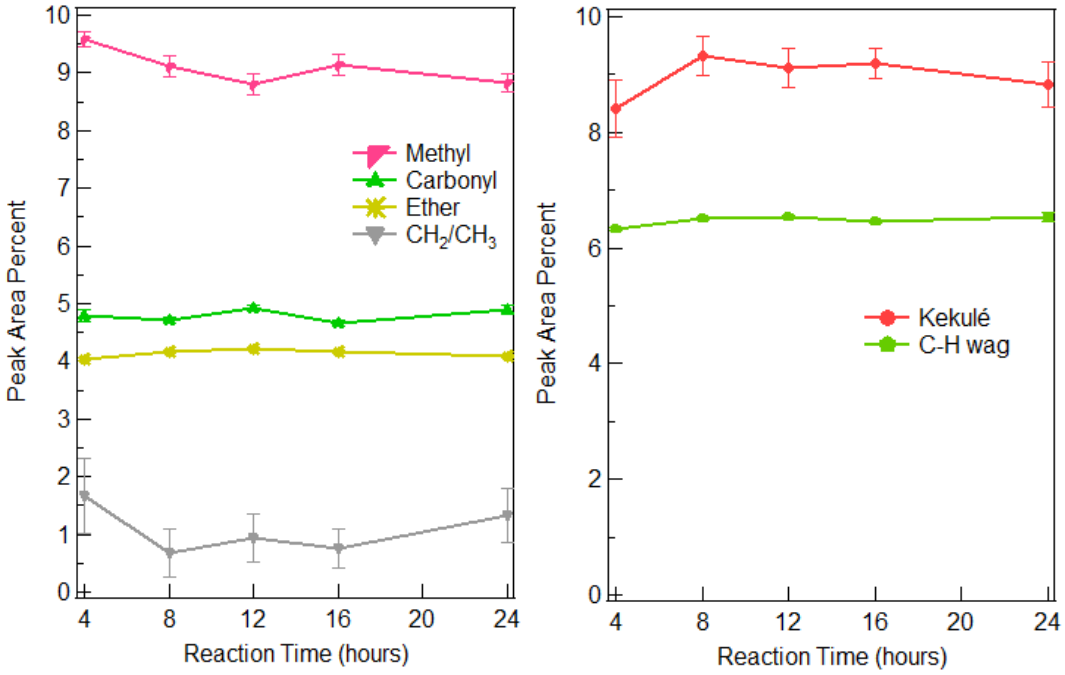

Figure 31. Raman fit peak area % of functional modes and the Kekule and C-H wag modes using variable method, plotted against reaction time. Left) Functional modes, from top to bottom: Methyl, Carbonyl, Ether, and CH_2/CH_3 bands. Right) The Kekule and C-H wag. The confidence intervals are plotted for all species shown.

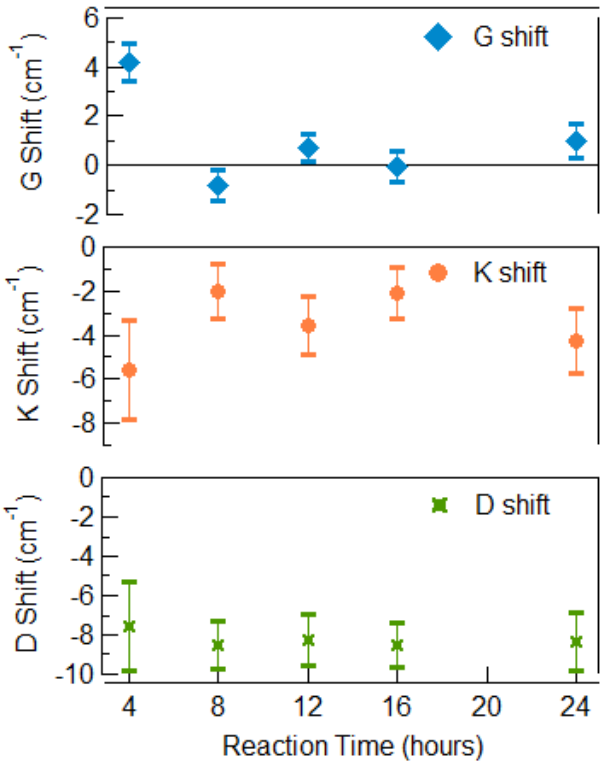

Figure 32. Shift in the G band, Kekulé, and D band fit position with reaction time from their zero positions for the of 1580, 1441, and 1341 cm^{-1} respectively. Error bars are shown, which are the 95% confidence interval for the new position confidence.

The changes in the band positions of the G band, D band, and Kekulé band from the assigned positions are shown in Figure 32. The G band position at 4 hours is 1585 cm^{-1}, but decreases to around 1580 cm^{-1} at reaction times beyond 4 hours. The assignment of the G band to 1580 cm^{-1} appears to be a good approximation for the stationary assignment, and there is generally small variability of the G band position.

The Kekulé band position trend appears to be the same as the G band, but in the opposite direction. The error bars on the Kekulé position are much wider than the G shift, indicating that the Kekulé band is difficult to fit exactly and the variability seen in the Kekulé shift and the scatter of the trend indicates that fitting the Kekulé position could result in overfitting of the spectra. Part of the reason the G band is easier to fit than the Kekulé is because it is a large, standalone peak, while the Kekulé is near the methyl and the D band, which is also allowed to vary and could interfere with the Kekulé. The Kekulé position appears to

blue-shift with reaction time, but the change is not statistically significant. The D band position appears to slightly red-shift in wavenumber with reaction time, but the trend is also not statistically significant. The error bars on the D Band shift appear to be comparable in size to those of the Kekulé. Of the three bands, the D band appears to have the least accurate assigned position, as the band shifts on average 8 cm^{-1}, compared to 2-3 for the Kekulé, and essentially no shift for the G band.

Comparison of the Stationary and Variable Methods

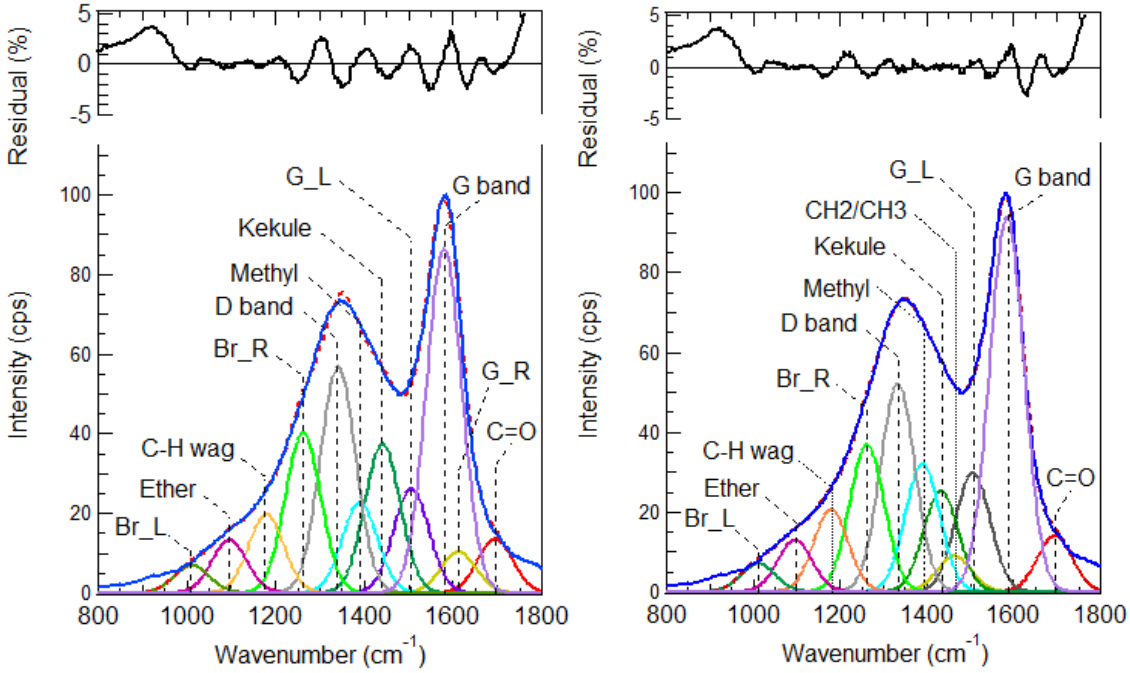

Figure 33. Average 4-hour hydrochar Raman spectra, fit by the two fitting methods, and includes the sum of fits curve (dotted curve), the fit peaks, and the residual of the fit (the fit curve subtracted against the raw spectra). a) Raman spectra fit by the Stationary Method. b) Raman spectra fit by the Variable Method.

Sample fit curves for the stationary and variable fitting methods are shown in Figure 33. While much of the fits are not easily distinguishable between the two fitting methods, the D Band (grey), Methyl (sky blue) and Kekulé (dark green) appear different. The D Band is shifted slightly to the left in the variable method, while the Methyl appears to have increased in the variable method, while the Kekulé decreased. The G-Resonance seems to have disappeared in the variable method, and the G band has increased in

intensity. The residual for both can also be visually compared. From about 1150-1500 cm^{-1}, the stationary and the variable residuals are noticeably different, with greater residual in the stationary method.

The improvement in r^2 of the fit going from the stationary to the variable method is quantified by Table 6, and the variable method is a marginal improvement roughly from 0.9967 to 0.9977. The standard deviation on the r^2 values (for 15 runs each) was between 0.0003 and 0.0005 for all points. The fit improves with variable G Band, D Band, and Kekulé fit peak positions, without making any region of the fitting area worse than the stationary method.

Table 6. Comparison of the average r^2 values for the sum of least squares fitting for the Stationary and Variable methods. The standard deviations on the r^2 values was between 3E-4 and 5E-4 for all points.

	Stationary Method r^2 Values	Variable Method r^2 Values
4hg	0.9963	0.9974
8hg	0.9967	0.9977
12hg	0.9967	0.9977
16hg	0.9969	0.9979
24hg	0.9965	0.9977

The D/G and K/G trends determined by the stationary and variable methods had some noteworthy differences, and are shown in Figure 34. The D/G and K/G trends pointed in opposite directions using different methods, which is a noteworthy discrepancy. Also of note, in the variable method, the K/G has much more variability than the D/G, but in the stationary method, it is the D/G that has more variability,

with the K/G showing small changes. Allowing the G, D, and Kekulé bands to shift in position changed how the uncertainty or variability was distributed in the fitting. With stationary fitting, the D and G band intensities had significant variability. Allowing these to shift resulted in variability in the band positions and the Kekulé band intensity. The variable method trends are preferred over the stationary, as the positions do change with reaction time (especially the G band), and the D band position was far from the best fit. By not accounting for this, the Raman spectra are not fit in a representative manner with the stationary method, so the trends hold less meaning.

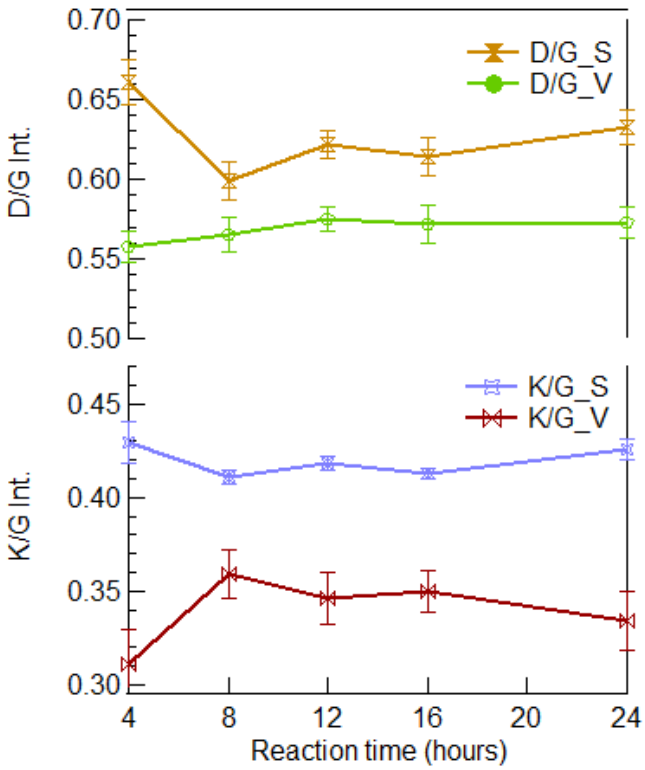

Figure 34. Comparison of K/G and D/G intensity ratios with reaction time by stationary and variable methods.

Discussion

The Variable fitting method reliably fits the hydrochar structure, which shows changes with reaction time, which can be used to further corroborate the structure of hydrochar based on the Brown et al. study [37]. The Brown et al. study employed the G, D, and Kekulé band positions and the D/G, Kekulé/G, and Kekulé/D

intensity ratios to determine the arene and furan composition of the hydrochar. From the Raman and using NMR, Brown et al. concluded the structure of hydrochar consisted of aldehyde-functionalized furans and 2-3 ring aldehyde-functionalized arenes connected by aliphatic chains. To bolster this claim, the hydrochar Raman trends are examined to see if there are consistent with increased arene domain sizes.

When excluding model compounds for the structure of hydrochar, Brown et al. acknowledged that the D band position and the D/G ratio were the best indicators for the hydrochar structure, based on the sharp difference between some of the model compounds and the hydrochar. If the size of the (aldehyde-functionalized) arene rings increased (from 2 towards 3 ring), the D/G ratio would increase from 1.1 to 3.3-4.4, and the D position would increase from 1354 to 1330-1390 cm^{-1} (which has a midpoint of 1360 cm^{-1}). Consistent with the D/G trend, the ratio increases with reaction time, from 0.56 to 0.57, while the D band position shifts from 1333 to 1332 cm^{-1}, unlike the trend. However, when the The D/G ratio shift is extremely small, and indicates a very slight shift from 2- to 3-ring arenes. While the D band position indicates the opposite, which is a shift towards more 2-ring arenes, the uncertainty on the calculated 3-ring D band position is very large and the general trend for the D band is to decrease in position with increasing aromatic domain size after 2 carbons.

The G band location shifts to lower wavenumbers, from 1584 to 1580 cm^{-1}, in agreement with the shift from 2- to 3-ring arenes, which clearly decreases from 1571 to 1550-1567 cm^{-1}. The Kekulé position increases from 1435 to 1438 cm^{-1}, which corresponds to the simulated shift from 1438 to 1458 ± 20 cm^{-1}. The K/G intensity ratio increased from 0.31 to 0.34 from 4 to 24 hours, which also agrees with the simulated change from 2- to 3-ring aldehyde-functionalized aromatics, which increases from 0.31 to 0.6 ± 0.1. Of the 5 independent (the K/D ratio can be determined by the D/G and K/G ratios) Raman metrics used to analyze hydrochar, four of these agree with the assessment that the structure of hydrochar shifts from 2-ring aromatics towards 3-ring aromatics.

Changes in the furan content are also possible, and based on the mass spectrometry evidence, with the increase in the $C_6H_7O^+$ ion with respect to the $C_5H_3O_2^+$ and $C_5H_4O_2^+$ ions with reaction time, this could indicate that the aldehyde group on the 5-HMF incorporated into the hydrochar structure disappears with reaction time. This transitions might be examined by the Raman assignments for aldehyde-functionalized furan converting to furan. The G band location of 1584 ± 20 cm^{-1} shifts to 1594 ± 35 cm^{-1}, while the D band location shifts from 1342 ± 53 cm^{-1} to 1205 ± 71 cm^{-1}, and the Furan mode (Kekulé mode equivalent for furan species) location shifts from 1496 ± 25 cm^{-1} to 1474 ± 34 cm^{-1}. The transitions seen in hydrochar are red-shifts in the G and D band positions and a blue-shift in the Kekulé band position, which are all opposite the trends observed here. The D band shift is the most apparent change, shifting 140 cm^{-1}. The intensity ratios of the furan vibrations, the furan D/G and the Furan Mode/G show changes of 3.9 to 530 and 18 to 750 respectively, indicating that the D band and Furan mode bands would become much more prominent than the furan G mode with the loss of the carbonyl group on the furan. The Furan/D mode intensity ratio decreases from 4.9 to 1.4, indicating that the Furan and D modes of furan would be equal in intensity. These changes are not observed in the hydrochar Raman spectra, with the fit peak closest to 1200 cm^{-1} (CH wag, at 1179 cm^{-1}) remaining constant in intensity with reaction time.

Conclusions

From the comparison of the Raman fitting methods, it is clear that both fitting methods worked well to fit the data, with good overall r^2 values, while most of fit peaks did not vary significantly between the two methods, indicating that changes in band positions were not dramatic. However, the D and G band positions have been known to be important markers for the structure of carbon materials [38], The band positions could not be obtained without varying the positions. In addition, the D Band showed a well-defined trend that fits with what hydrochar is expected to do with reaction time.

Since the variable method has 3 more degrees of freedom for the fitting, (the G Band, D Band, and Kekulé fit peak positions) the fitting algorithm changes these to improve the fitting. While this can lead to more

information from the Raman spectra with increased accuracy, it may be overfitting the spectra, by artificially moving peaks such as the Kekulé and Defect to improve the fitting. Evidence of this behavior is shown in the CH_2/CH_3 trend, which strongly resembles the inverse of the Kekulé shift trend and has large uncertainty despite its small fit area. For this reason it may be of benefit to use a different convergence method where band positions are bounded or allow to change in a dependent manner.

The Brown et al. fitting methods are ultimately more meaningful than the Li et al. and the Sadezky et al., as these are developed for coal and soot respectively. Li et al. has two peaks representing arenes with greater than 6 or less than 6 rings, and does not have a Kekulé/furan mode. Sadezky et al. assignments are developed for a graphitized material, and hydrochar simply does not possess 'defects' in the same way that the Sadezky methods does. While both methods (Li and Sadezky) can fit the spectra of hydrochar well, the fitting is not meaningful to the underlying chemistry of the material. For this reason it is important to have sound assignments for the fit curves and well-defined, narrow ranges that they are expected to be. In this study, while much did not change between the Stationary and Variable methods, the variable method gave significant variability to the methyl band intensity, CH_2/CH_3 band intensity, and the Kekulé position. All these bands are adjacent, and share a similar behavior.

Finally, it is worth noting that a great deal of refining went into this process to characterize hydrochar by Raman Spectroscopy. The signal to fluorescence, instrument settings, and fitting method were modified for this analysis. Another area for improvement is increasing the denoising filter was applied to all of the spectra. The noise of the spectra may not affect the peak intensities directly, but can decrease the sensitivity towards the peak positions.

The most significant findings from this method are that the G Band position decreases about 4 cm^{-1} from 4 to 8 hours, while the D band has a slight decrease in position with reaction time. In addition, the D/G ratio does not change noticeably with reaction time. The Methyl Band decreases with reaction time, which

was backed up with both fitting methods. Finally, the variability in the D and G band area has decreased by allowing for the bands to shift in position, which indicates that that allowing the bands to vary in position does not result in erratic changes in the peak fit area. As shown in Figure 34 Raman spectra of hydrochar are very similar in shape, highlighting the importance that the fitting method should not fit to the best shape (i.e. overfit), but should allow for the interpretation of the underlying chemistry. The variable fitting method does accomplish this task, and can be used to understand the changes in other carbon materials.

Mass Spectrometry

The Mass Spectra shows the presence of methyl, alcohol, and ketone functionality, along with, furan and arene content, supporting the IR. With reaction time, the aromatic content increases significantly relative to the furan content, and the 2-ring vs 1-ring arene ratio increases with reaction time, consistent with the Raman Spectroscopy.

Mass Spectra Assignments

The mass spectra for 12-hour hydrochar colored by ion family is shown in Figure 35**Error! Reference source not found.**. The inset shows the mass spectra at full-scale across the range of m/z=10 to m/z=60. The largest peaks are at m/z=18, 28, and 44, corresponding to H_2O, CO, and CO_2 respectively. The CO accounts for ~35% of the total signal, while the CO_2 and H_2O account for around 10 % each. These products are believed to be decomposition products of hydrochar, and have been noted to increase in intensity when only using the thermal vaporizer on the AMS.

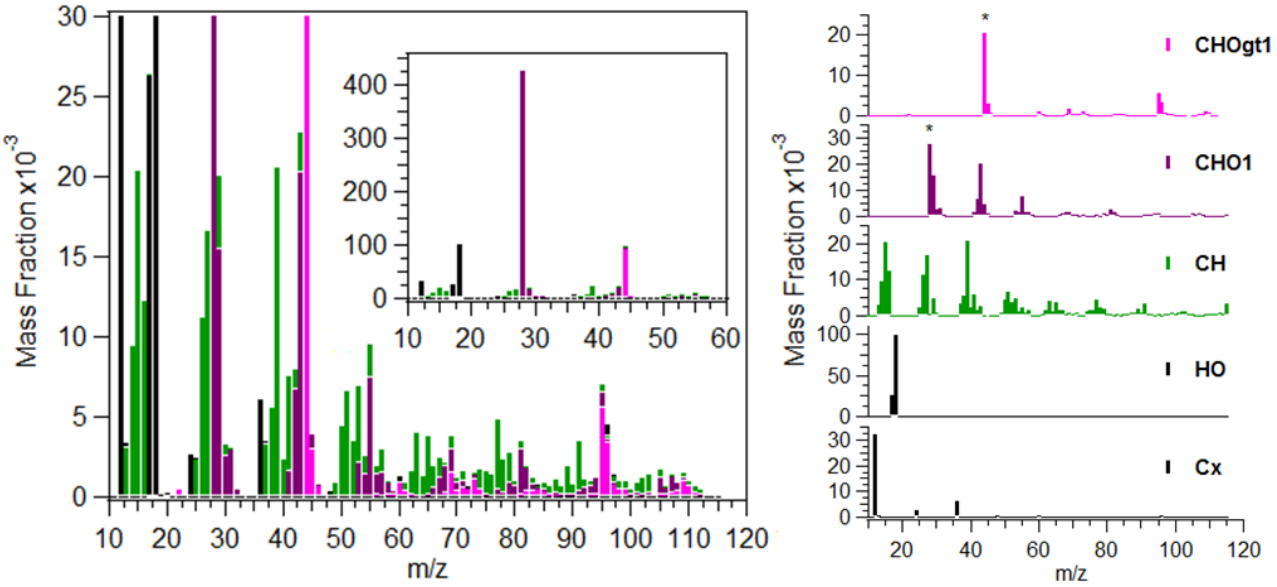

Figure 35. Left) AMS Spectra of 12-hour hydrochar, with peak areas represented by the ion families, not to full scale. Inset) Same spectra, across range m/z=10 to 60, at full scale. Right) Mass Spectrum of 12-hour char by ion family, plotted on separate y-axes. The CO and CO_2 peaks exceed the scales and are denoted by stars.

The overall mass composition of the hydrochar spectra by ion family is shown in the pie chart in Figure 36, with the signals increasing in the order CHOgt1 < CH < CHO1. The Cx family is the family of ions that only contains carbon. The C_1 and C_3 signals are the largest Cx signals, accounting for 3 and 0.5% of the total mass signal respectively. The C_3 signal has been observed in the characterization of soot by AMS, and is an ion fragment of aromatic carbon. In a study by Corbin et al. [95], the SP-AMS was used to analyze a variety of soot compounds, and the C_1/C_3 mass ratio was used as an indicator for the chemistry. The C_1/C_3 ratio was found to be around 0.67. This is very different to hydrochar, which has a C1/C3 ratio of around 6. According to Corbin et al., an organic molecule is much more likely to form C1 than C3, so the amount of C3 is an indicator for the black-carbon content. The Cx signal overall comprises around 5% of the total mass. The HO family contains ion fragments containing at least 1 Oxygen and at least 1 Hydrogen, with no other atoms. The ions for this family are m/z=18, 17, and 16, corresponding to the presence of water in the hydrochar, and comprises about 13% of the total signal.

The other three ion families shown are the CH, CHO1, and CHOgt1, which are the presence of ion fragments containing carbon and at least one hydrogen and zero oxygen, carbon and exactly 1 oxygen, and carbon and at least 2 oxygen respectively. The presence of molecular oxygen in hydrochar is significant from a functional standpoint, as hydrochar is believed to have alcohol, carboxylic acid, and ketones groups. The relative distributions of the CH, CHO1, and CHOgt1, and the ion fragments attributed to them can confirm earlier analysis on the oxygen distribution, and perhaps the presence of aromatic or furanic domains.

The CH family has a strong methyl peak, with very small peaks for any other alkyl ions. At m/z=77, the first significant peak for an aromatic is observed ($C_6H_5^+$), the benzyl ion. At m/z=91, a larger peak than the phenyl ion is observed, and is attributed to $C_7H_7^+$, which is the benzyl ion. This ion indicates single-ring aromatic with an alkyl functionality. This structure is predicted based on the presence of the strong methyl band in the Raman spectra. At m/z=115, a strong peak is observed is attributed to $C_9H_7^+$, which is attributed to indene or benzofuran. The presence of the alkyl and aromatic content is supported by the IR Spectra, which shows both aliphatic and aromatic CH stretches, aromatic C=C stretch, and aromatic C-H wag. The Raman Spectroscopy indicates an aromatic content consisting of small arene units (1-2 rings) with alkyl linkages [37].

The CHO1 family has significant peaks at m/z=28, 43, and 55, attributed to CO^+, $C_2H_3O^+$, and $C_3H_3O^+$ respectively. The quantities of these ions, containing oxygen, are high because of the stability of the ions, due to their small size. The peak at m/z=43 is observed in alkyl alcohols and primary ketones, in particular levulinic acid, which the NIST mass spectra [96] has its main peaks at m/z=43 and m/z=55 at a similar ratio to that observed in the mass spectra shown. Levulinic acid is a known decomposition product of 5-HMF (a known intermediate in the formation of hydrochar from glucose) [54, 97], and Baccile et al. proposed levulinic acid exists embedded within the hydrochar structure [32].

The CHOgt1 family has its strongest peaks at m/z=43, 95, and 96, attributed to CO_2^+, $C_5H_3O_2^+$ and $C_5H_4O_2^+$ respectively. The $C_5H_3O_2^+$ and $C_5H_4O_2^+$ could be attributed to a furfural-type functionality, which is a furan ring with a carbonyl group off the ring. The NIST mass spectra of furfural [96], has two major peaks at m/z=95 and 96, which is strong evidence for the type of functionality.

Ion Family Composition

The adjusted composition of 12-hour hydrochar is shown in Figure 36. The CH ion family comprises 50 % of the mass spectra, followed by the CHO1 family with 22% of the signal. The CHOgt1, Cx, and HO are of comparable area, with around 11%, 9%, and 9% respectively of the mass signal. The H2O and Cx ions come from the decomposition of the hydrochar, which is not expected to have significant black carbon content or significant water content either.

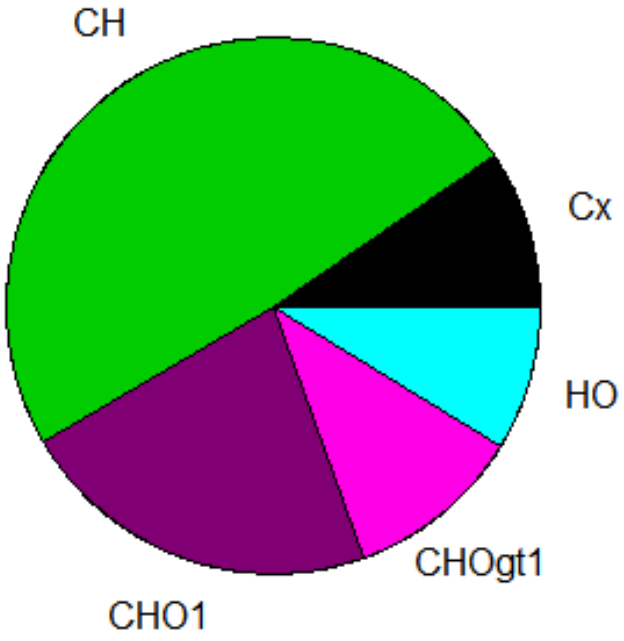

Figure 36. Pie chart of 12-hour hydrochar ion family mass composition.The composition is adjusted by removing the CO, CO_2, and H_2O ions. The mass spectra used for this pie chart is the Apr20 t3 run.

Elemental Composition

The average elemental composition of the hydrochar from the elemental analysis compared to the AMS-derived composition is shown in Figure 37. The EA average atomic H/C and O/C ratios are 0.76 and 0.30 respectively, while the AMS_Raw ratios are 1.05 and 0.74 respectively. The discrepancy in the hydrogen content is small relative to the O/C ratio, which is greater than two-fold. The over-representation of the oxygen is evident in the large size of the CO, CO_2, and H_2O peaks, which collectively account for 60% of the mass signal. The disparity in mass composition, coupled with the large size of the CO, CO_2, and H_2O peaks was the reasoning behind eliminating these peaks to obtain agreement between the AMS and the composition of the material. As shown in Figure 37, the H_2O peak was removed. As a result, the composition changed with decreased H/C and O/C contents. The H/C ratio agrees well with the bulk characterization, but the O/C ratio is still double what it should be in value. Removing the CO and CO_2 peaks from the raw spectra betters the O/C ratio from 0.74 to 0.46, but the H/C ratio increases to an unacceptable degree.

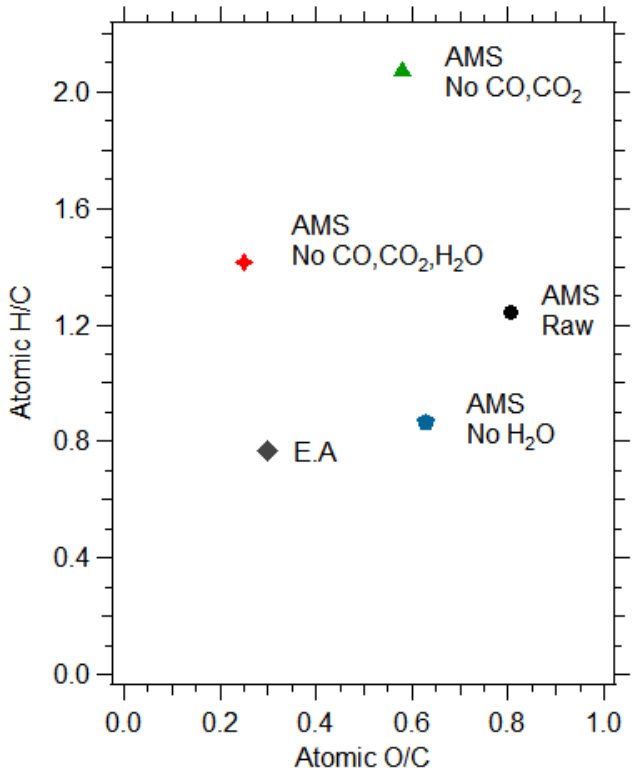

Figure 37. Van-Krevelen diagram of average elemental composition of hydrochar derived from bulk elemental analysis, compared with the composition derived from AMS. The AMS-derived compositions are the "AMS_raw", or as-is composition, the "AMS_noH2O", where the H2O content is removed from elemental composition calculation, and the "AMS_noCO_and_CO2", where the CO and CO_2 peaks are removed from elemental composition calculation.

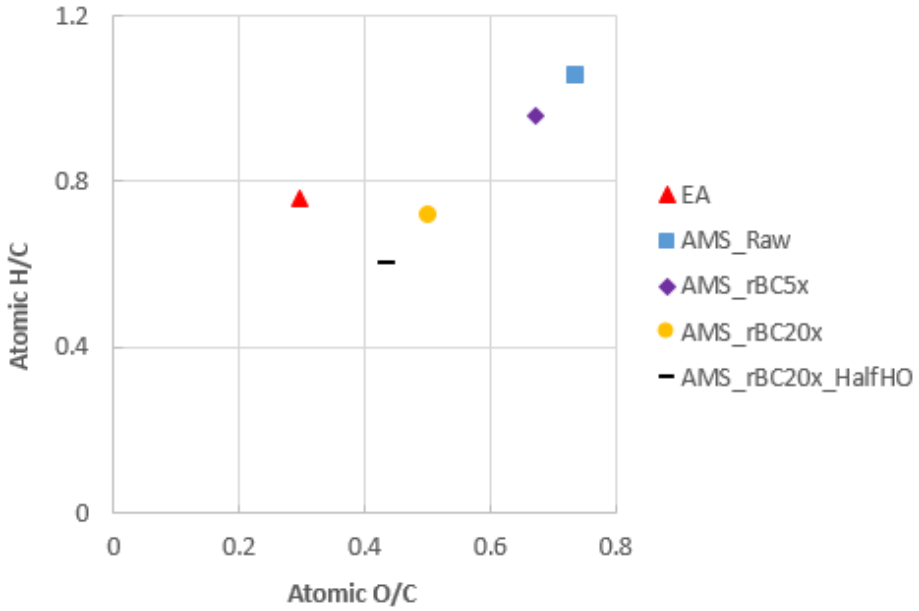

Figure 38. Van-Krevelen diagram of average atomic elemental composition of hydrochar derived from bulk elemental analysis, compared with the composition derived from AMS. The AMS-derived compositions are the "AMS_Raw", or as-is composition, the "AMS_rBC5x" multiplies a portion of the Cx content by 5, the "AMS_rBC20x" multiplies a portion of the Cx content by 20, and the "AMS_rBC20x_halfHO" does the same as previous, while also decreasing the HO content by 50%.

The changes in the elemental composition of the AMS by fitting a "rBC content" to the material, with a scaling factor to account for the low ionization efficiency (and a low collection efficiency) is shown in Figure 38. The rBC content is small, as a change of 5 times the content in size did not change the elemental composition substantially. With a factor of 20 (a factor of 5 for the ionization efficiency and a factor of 4 for the collection efficiency), the rBC content approaches the same H/C ratio as the bulk elemental composition. Removing half of the HO content of the 20x sample continues the change in composition in a close direction to before.

While fitting for a rBC content brings the elemental composition closer to that of the bulk composition, the trend underestimates the H/C ratio while overestimating the O/C ratio. The big assumption behind

the fitting of the rBC content is that hydrochar contains rBC. The Raman of hydrochar suggests 2-3 ring arenes, not a graphitic or highly carbonized or condensed aromatic structure. The AMS does not detect significant aromatic compounds, so this method which was developed for soot particles, which are known to have a significant rBC content, may not be appropriate. Since it is possible that the elemental composition can be fit by a combination of scaling down the CO and or CO_2, scaling up the rBC content and scaling down the H_2O, it is important to consider how the ions form and what their presence indicates about the material.

CO, CO_2, and H_2O content

CO, CO_2, and H_2O are partial and total combustion products for a carbon material, however, no oxygen gas was present as the carrier and purge gas used was Argon, so the high amount of CO and CO_2 is due to the high oxygen content of the char. In a study of organic compounds by aerosol mass spectrometry, Canagaratna et al. note that the thermal vaporization conditions used in AMS can decarboxylate and dehydrate oxidized organic aerosols, and lists H_2O as a decomposition product of alcohols functionality while H_2O, CO_2, and CO can form from carboxylic acids [89].

Yu et al. studied the thermal decomposition products of hydrochar via TG-IR, and the glucose-derived hydrochars prepared at 180 °C were found to have significant CO and CO_2 peaks, with the CO_2 coming off in one distinct peak, while the CO came off in a long, broad peak, which indicates that the CO_2 comes from essentially one type of functionality, while the CO comes from a variety of sources, as the hydrochar pyrolyzes. The CO peak can therefore be looked at as a rough marker for the other types of oxygen-containing functionality in the material besides the carboxylic acid.

Corbin et al. indicated that the CO peak in SP-AMS (of appeared to be particle size dependent, and also did not appear in SP-AMS when the laser was not used to vaporize the soot samples (with the resistively-heated vaporizer on) [95]. Again, this reinforces that CO is a thermal decomposition product, and since it is found to vary with particle size, this suggests that CO come from the surface of the material. Although the

bulk elemental composition of hydrochar does not change significantly with reaction time, the particle size does. SEM is shown in Figure 73 and Figure 74 in the Appendix, and particle size clearly changes from the 3-hour to 4-hour hydrochar, and from the 12-hour to 72-hour hydrochar. The changes in the CO peak with reaction time will be explored in the next section.

Changes with Reaction Time

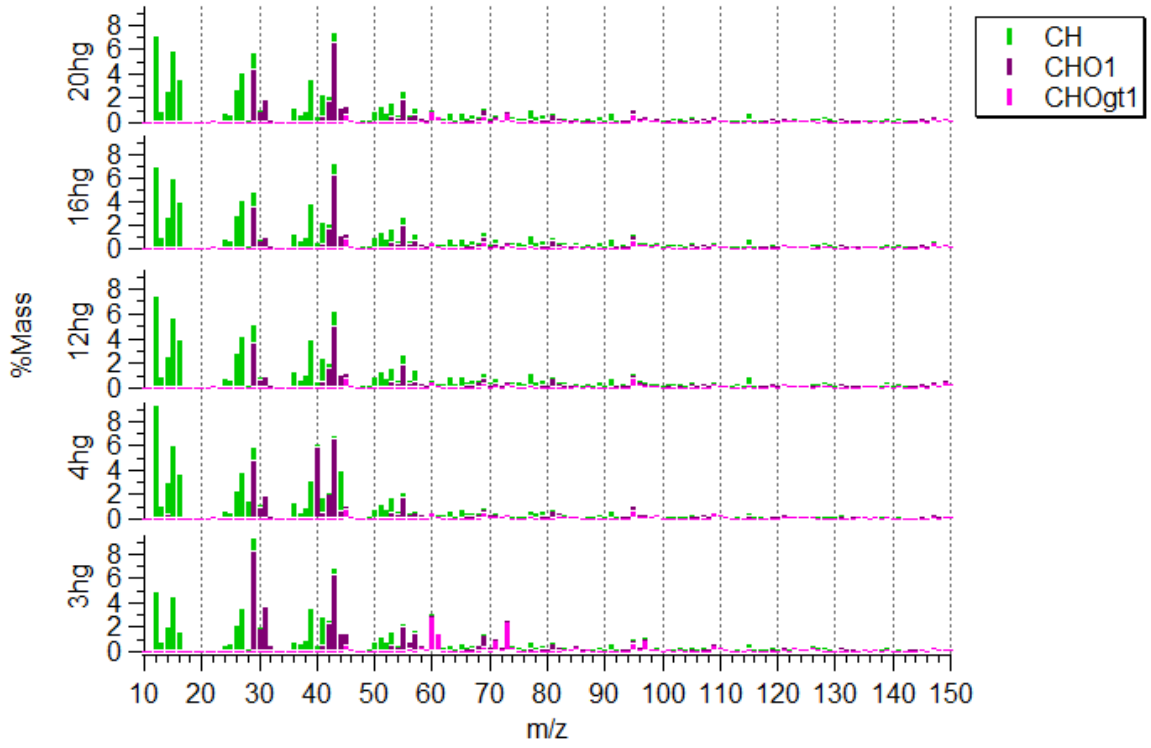

Figure 39. Mass Spectra of hydrochar used for ion trends. Spectra were normalized by removing the CO and CO_2 ions and HO family ions. The CH ions (containing carbon, or carbon and hydrogen) are in green, the CHO1 ions (containing carbon, hydrogen, and 1 oxygen atom) are in purple, and the CHOgt1 ions (containing carbon, hydrogen, and more than 1 oxygen atom) are in pink.

The mass spectra of the hydrochar used for analyzing changes in composition with reaction time are shown in Figure 39. The mass spectra shows some major changes with reaction time, such as the appearance of a major CHO1 peak at m/z=40 at 4 hours, the disappearance of the CHOgt1 peaks at m/z=60 and m/z=73 after 3 hours, for example. The method is sensitive enough to detect changes in hydrochar chemistry from hydrochars prepared at different reaction times.

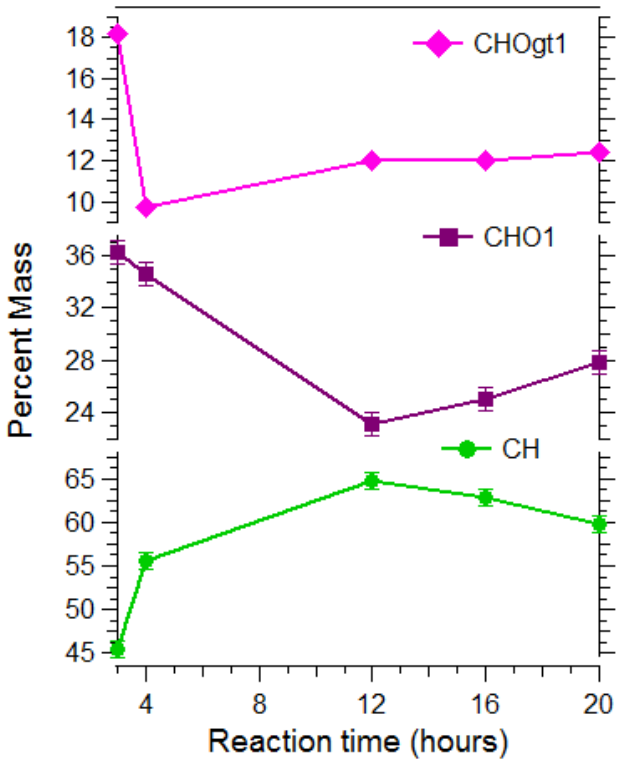

Figure 40. Relative mass composition of the ion families of the hydrochar mass spectra as a function of reaction time. The CO, CO_2, and HO family ions were removed from the mass spectra, to normalize the spectra. From top to bottom: CHOgt1 (pink, bow-tie), CHO1 (purple, diamond), CH (green, square).

In Figure 40, the changes in the mass composition of the ion families with reaction time are shown. The CH content increases sharply from 3 to 12 hours from 45% to 65% of the mass, and remains constant. The CHO1 content decreases from 36% to around 22% by 12 hours, and remains fairly constant. The CHOgt1 content, meanwhile, shows the most dramatic change with a sharp decrease from 3 to 4 hours (from 18% to around 10%), and increases to around 12% mass. The ion family trends are expected given the elemental trends which shows a decrease in oxygen content with reaction time. While the Elemental Analysis did not measure the 3-hour composition, the mass spectrometry indicates that the elemental composition would differ from the 4-hour. It is also worth noting that the change by ion family composition may be a more sensitive measure of composition than the elemental analysis, showing more dramatic changes with reaction time.

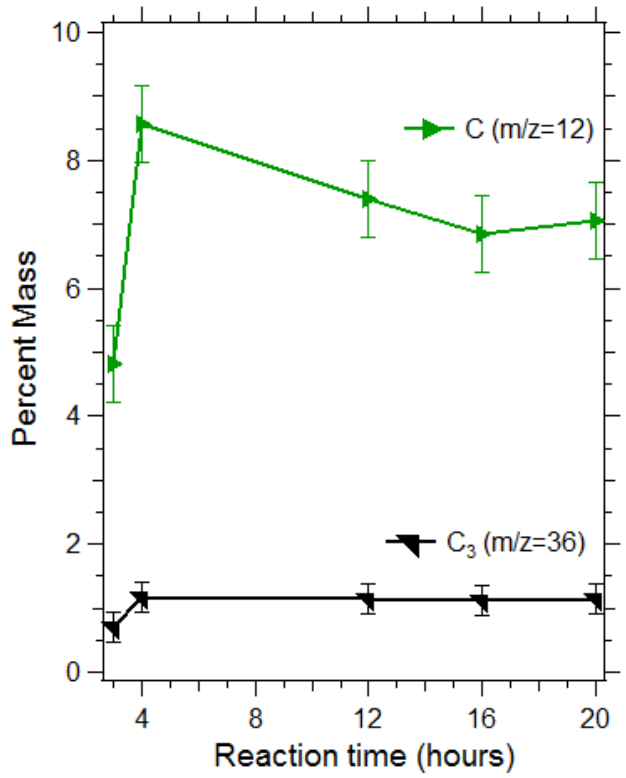

Figure 41. Composition of mass spectrometry Cx ions as a function of reaction time. The mass composition is the percentage of the ions mass out of the total mass of all the organic ions, excluding the CO and CO_2 ions and the HO family ions. The C and C_3 ions are plotted.

The trends in the carbon ions (C and C_3) are shown in Figure 41 with similar trends. C (m/z=12) is attributed to organic carbon, and increases from 3 to 4 hours, before decreasing from 4 to 16 hours. The C_3 ions also increases from 3 to 4 hours, but remains at a constant value. The C_3 ion is attributed to black carbon, and the relatively small size indicates that the black carbon content of hydrochar is negligible.

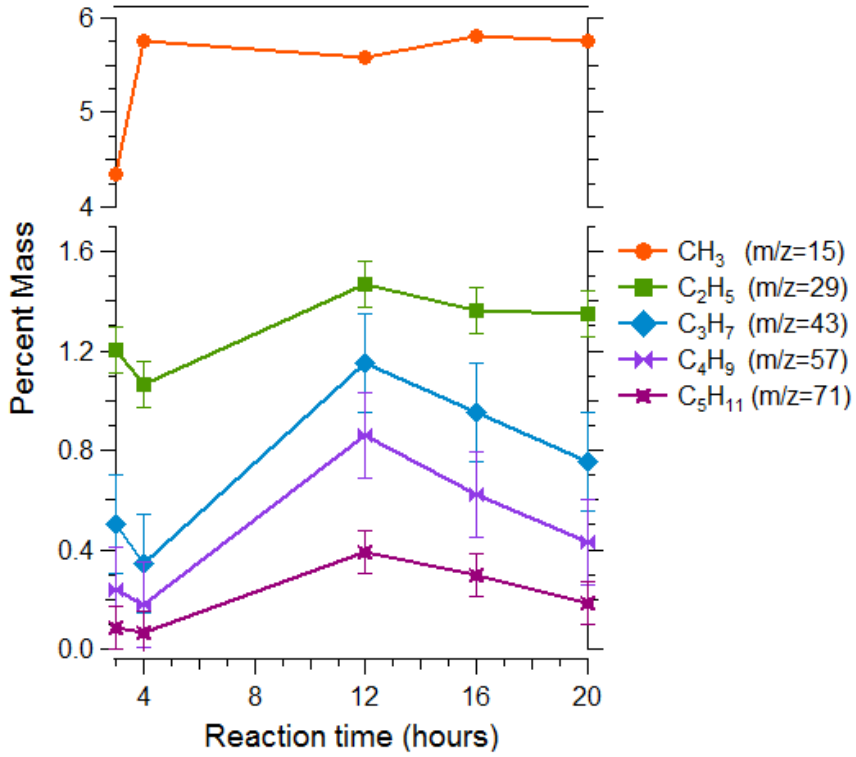

Figure 42. Mass Composition of mass spectrometry aliphatic ions as a function of reaction time. The mass composition is the percentage of the ions mass out of the total mass of all the organic ions, excluding the CO and CO2 ions and the HO family ions. Ions plotted are from top to bottom: CH_3 (orange, circle), C_2H_5 (green, square), C_3H_7 (blue, diamond), C_4H_9 (purple, hour-glass), and C_5H_{11} (violet, flower).

The aliphatic CH ions with less than 6 carbons are shown in Figure 42, and decrease in mass composition with increasing fragment size. The 3-, 4-, and 5-carbon aliphatic fragments show very similar trends, indicating that larger alkyl chains of different sizes are incorporated into the hydrochar structure in a similar manner. The 2-carbon fragment (C_2H_5) displays a somewhat similar trend to the 3-,4, and 5-carbon fragments, which is a result of 2-carbon fragments forming from larger alkyl chains. The CH_3 ion indicates the methyl ions are much less prominent in the 3-hour hydrochar than the other alkyl chains, and changes quickly at 4-hours.

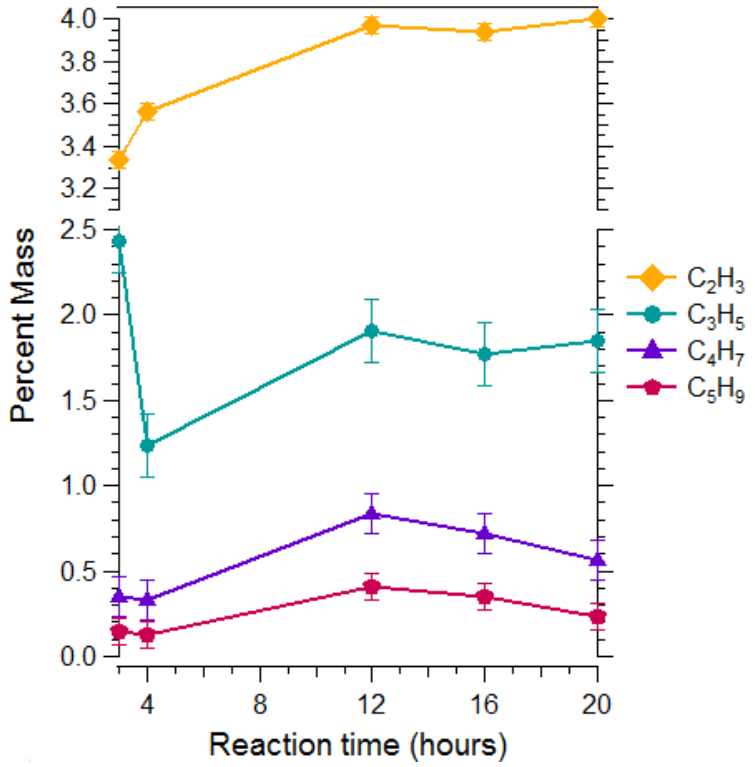

Figure 43. Mass Composition of mass spectrometry olefin ions as a function of reaction time. The mass composition is the percentage of the ions mass out of the total mass of all the organic ions, excluding the CO and CO_2 ions and the HO family ions. Ions plotted are (from top to bottom): C_2H_3 (yellow, diamond), C_3H_5 (blue, circle), C_4H_7 (purple, triangle), and C_5H_9 (violet, pentagon).

The olefin CH ion trends are shown in Figure 43 for 2-5 carbon fragments. The 4- and 5- carbon fragments shows strong similarity to the 3-, 4-, and 5-carbon aliphatic fragments. The 3-carbon fragment shows a different trend, decreasing after 3 hours. The 2-carbon olefin shows a near continuous increase with reaction time. This suggests the 2- and 3-carbon olefins are not related to the aliphatics and behave differently. It is not clear why the C_3H_5 fragment behaves so differently and more investigation is required for this ion.

In Figure 44, the aromatic CH ion trends all show a strong similarity to each other, with a strong increase in intensity between 4 and 12 hours. The 1-, 2-, and 3-ring arenes fall into 3 distinct mass ranges, and almost without exception decrease in concentration in the mass spectra with increasing molecular weight.

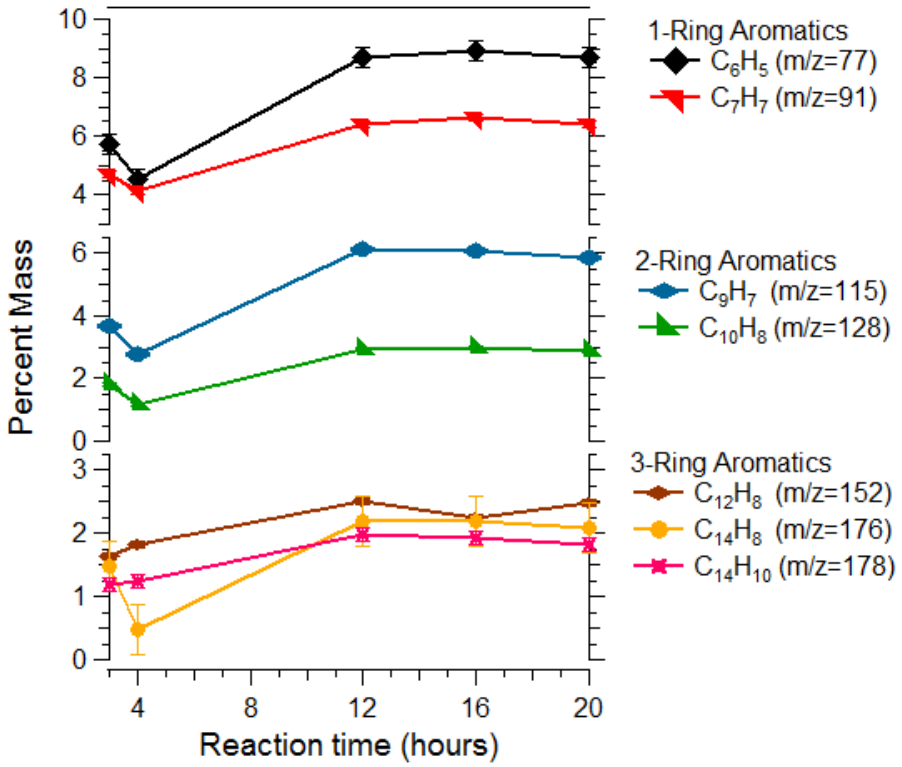

Figure 44. Mass composition of AMS aromatic CH ions as a function of reaction time. The mass composition is the mass fraction of the adjusted mass ascribed to the specific CH ion. From top to bottom: C_6H_5 (black, diamond), C_7H_7 (red, triangle), C_9H_7 (blue, diamond), $C_{12}H_8$ (brown, diamond) $C_{14}H_8$ (yellow, circle), $C_{14}H_{10}$ (pink, cross).

Additional CH ions are plotted in Figure 45, which have large variability in their positions, and the trends seem to somewhat resemble those of both the aromatic and the aliphatic trends. The ion trends for the C_4H_3 (m/z=51), C_5H_3 (m/z=63), and C_5H_5 (m/z=65) appear to be the closest in trend shape, and these ions are seen as minor side peaks for aromatic species based on NIST mass spectra, with m/z=63 as a side peak for indene and m/z=51 and m/z=65 for toluene [96]. m/z=39 was a side peak in the mass spectra of toluene, benzene, furfural, and 5-HMF [96], and the trend resembles those for $C_5H_3O_2$ and $C_5H_4O_2$, also furfural peaks.

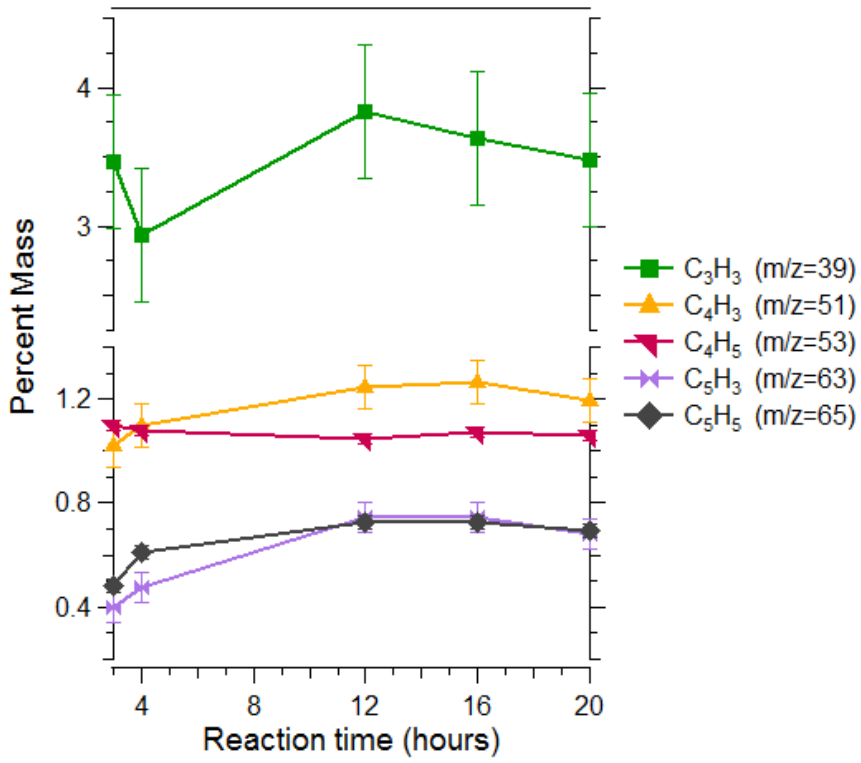

Figure 45. Mass composition of AMS CH ions as a function of reaction time. The mass composition is the mass fraction of the adjusted mass ascribed to the specific CH ions. From top to bottom: C_3H_3 (green, square), C_4H_3 (yellow, triangle), C_4H_5 (pink, triangle), C_5H_3 (purple, bow-tie), C_5H_5 (grey, diamond).

Significant CHO1 ions are plotted in Figure 46. All CHO1 ions have at least one degree of saturation, and these ions can indicate the presence of furanic rings and oxygen-containing functional groups. The CHO ion (m/z=29) decreases sharply from 3 to 4 hours, which has the same value as the 4 hour point. The CHO ion can be attributed to aldehydes, which are expected to be highly reactive under hydrothermal conditions based on the prevalence of aldol reactions in saccharide chemistry [67]. Patil et al. proposed that humin formation results from the high reactivity of 5-HMF with DHH (2,5-dioxo- 6-hydroxyhexanal), which can perform up to 5 aldol additions with HMF [69]. Several aldehyde species form from glucose, such as glyceraldehyde, glycolaldehyde, furfural, and 5-hydroxymethylfurfural [67].

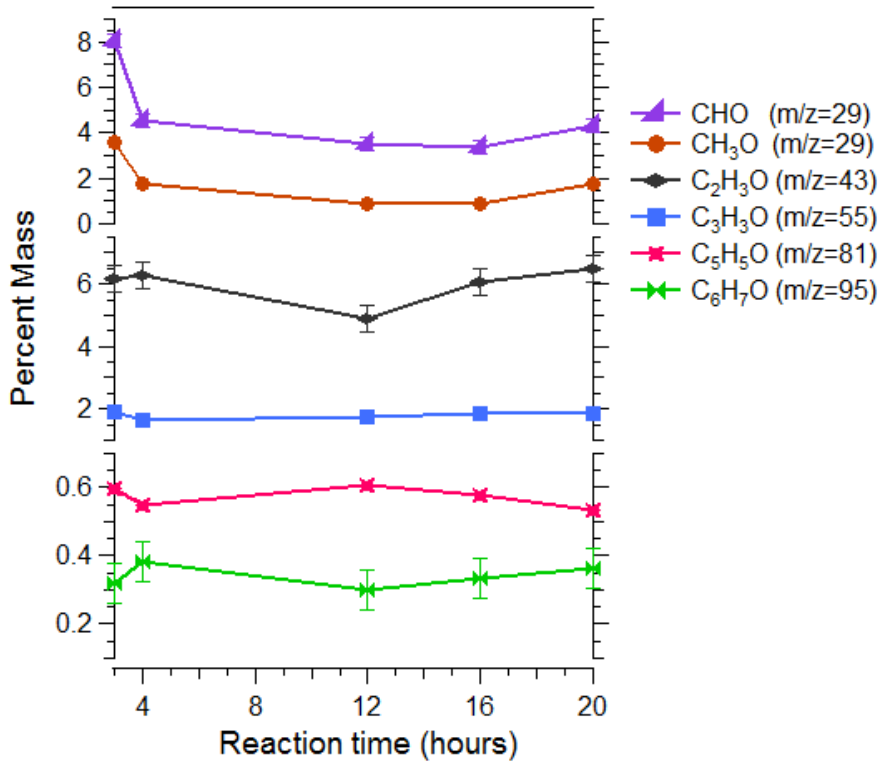

Figure 46. Mass composition of AMS CHO1 ions as a function of reaction time. From top to bottom: CHO, CH_3O, C_2H_3O, C_3H_3O, C_5H_5O, and C_6H_7O. The CHO1 ion family is the ions containing carbon and hydrogen, with exactly one oxygen atom.

The CH_3O peak (m/z=31) follows the trend for CHO, showing that the two ions are indistinguishable and provide the same information about the structure of hydrochar. This is somewhat surprising, as the CHO was believed to represent aldehydes, while the CH_3O was believed to represent alcohol groups at the end of alkyl chains (or as part of hydroxymethyl groups).

C_2H_3O can be attributed to methyl ketones and hydroxymethyl groups. The C_2H_3O trend appears to be at a minimum at 12-hours, but otherwise does not change with reaction time. C_6H_7O (m/z=95) is a dimethyl furan ion (furan with alkyl linkages at the 2- and 5-carbons), but it may appear from a species such as 5-methylfurfuryl alcohol. C_6H_7O shows a very similar trend to C_2H_3O, indicating that the two trends are related to each other. 5-methylfurfuryl alcohol has prominent peaks at m/z=43 and m/z=95, and the m/z=43 ion derives from the hydroxymethyl group.

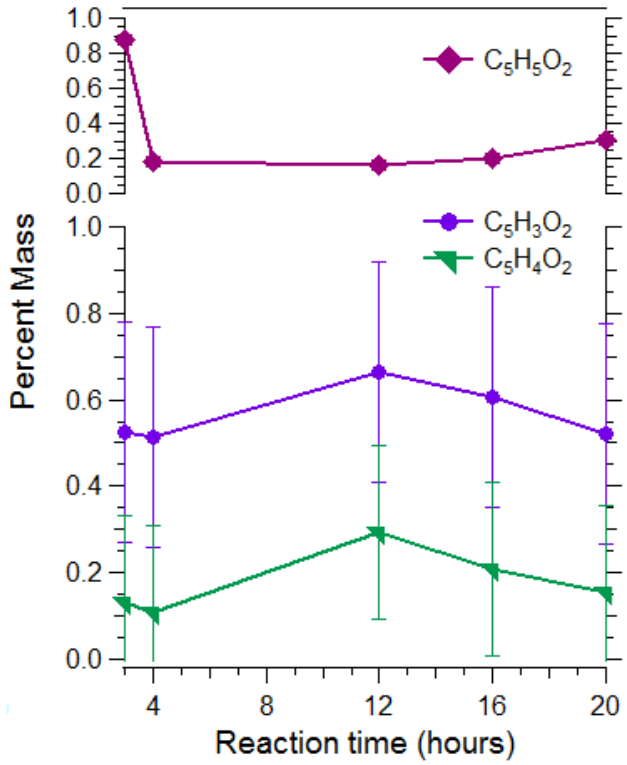

Figure 47. Mass composition of AMS CHOgt1 ions as a function of reaction time. The CHOgt1 ions plotted are $C_5H_3O_2$, $C_5H_4O_2$, and $C_5H_5O_2$. CHOgt1 ion family is the ions containing carbon and hydrogen, with more than one oxygen atom.

$C_3H_3O^+$ (m/z=55) cannot be attributed to specific compounds, but is seen as a side peak in levulinic acid however they are seen as minor side peaks for furan species, and do not appear to change significantly with reaction time. $C_5H_5O^+$ (m/z=81) is a furan peak (seen in the NIST webbook spectra of dimethylfuran), and appears to decrease with reaction time. The trend for $C_5H_5O^+$ appears to be the inverse of C_6H_7O (m/z=95).

The CHOgt1 trends are shown in Figure 47. $C_5H_3O_2$ and $C_5H_4O_2$ (m/z=95 and 96 respectively) are attributed to furfural functionality, and increase from 4 to 12 hours and decrease from 12 to 20 hours. The $C_5H_5O_2$ ion (m/z=97) is the main peak in the mass spectra of 5-hydroxymethylfurfural (5-HMF or HMF) [96] and differs from the $C_5H_3O_2$ and $C_5H_4O_2$ and decreases rapidly with reaction time. The significant difference in trend behavior between the m/z=97 and the m/z=95 and 96 could be due to the greater abundance of 5-HMF in hydrochar compared to furfural.

The mass spectra of hydrochar contains aliphatic ions along with aromatics and furans, with some evidence of the functional groups present, such as alcohols and ketones. The presence of aromatics, furans, aliphatics, and functional groups (alcohols and carbonyls) is consistent with the IR Spectroscopy, while the presence of aromatics (in particular the 2- and 3-ring aromatics) is supported by the Raman fitting, and NMR from literature sources support the presence of aromatics, aliphatics, and furans [32, 37]. Mass Spectrometry also shows the aromatic content to increase with reaction time (after the hydrochar initially forms at 3-4 hours). In addition, mass spectrometry shows a variety of furan peaks, with several different trends with reaction time, which could be used to understand how the furan functionality changes with reaction time. To better understand these trends, ratios of different functional groups are plotted against reaction time.

Elemental Composition Trends

Trends in the elemental compositions of hydrochar derived from the mass spectra are shown in Figure 48. The AMS trends with reaction time in the "Raw" or as-is mass spectra show the elemental O and C carbon changes very little with reaction time. The H content shows much higher relative variability, decreasing from 5 to 4 % from 3 to 4 hours, and increases by as much from 4 to 20 hours. The changes in the elemental composition by the Elemental Analysis method show bigger changes with reaction time for the oxygen and carbon, but show much smaller changes in the hydrogen composition.

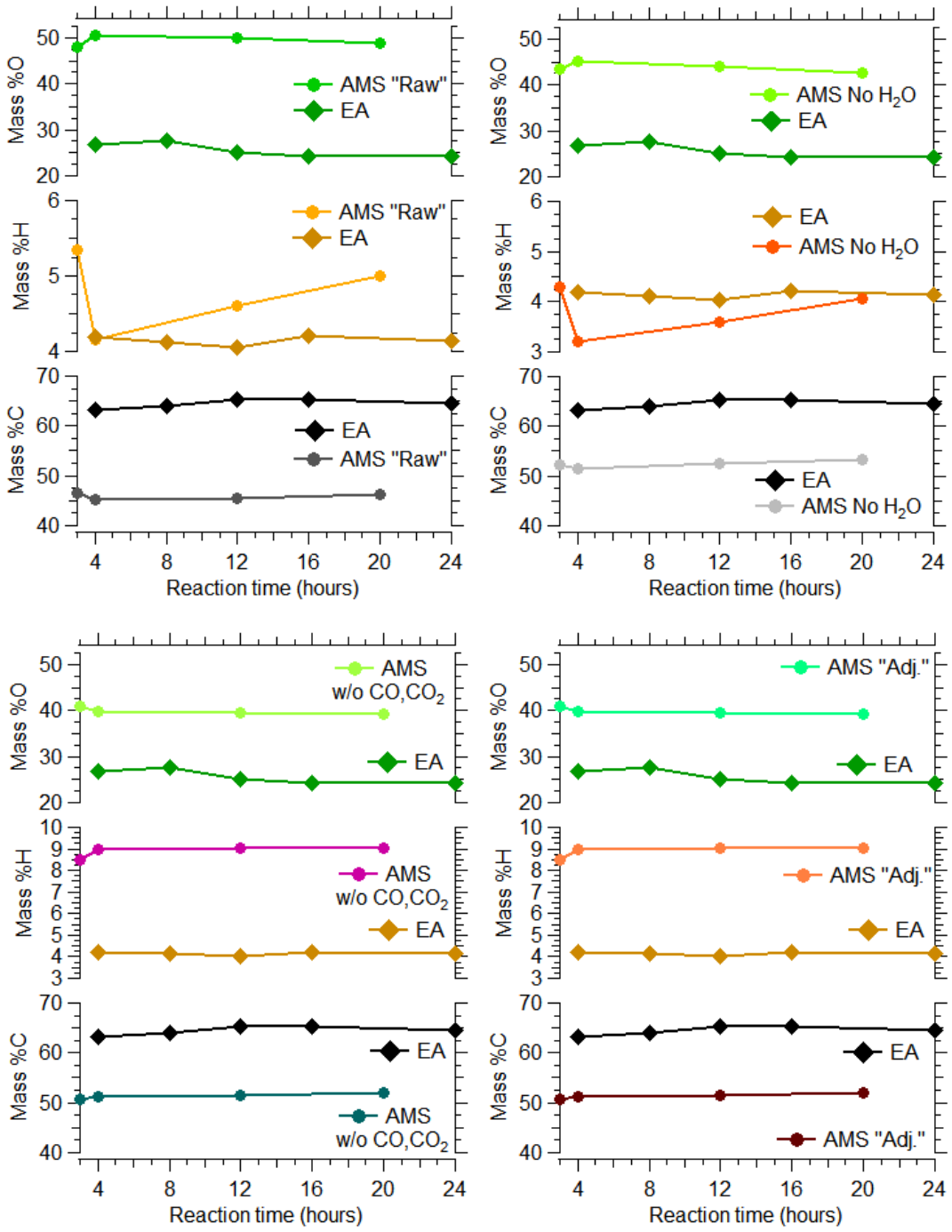

Figure 48. Elemental Composition of Hydrochar derived from Mass Spectrometry compared to Elemental Analysis Composition. Left, Top) Mass spectra directly converted to elemental composition. Right, Top) Mass spectra with the H_2O fragment removed. Left, Bottom) Mass spectra with both the CO and CO_2 fragments removed. Right, Bottom) Mass spectra, with CO, CO_2, and H_2O removed. No error bars were constructed for these graphs.

Removing the CO and CO_2, as shown in the bottom-left panel, makes the changes in the AMS hydrogen content much smaller with reaction time. In addition, the carbon and oxygen content change even less with reaction time, while retaining the same change between the 3 and 4 hour time points.

Simply removing the H_2O mass, does not appear to change the trends strongly with reaction time. As discussed in the elemental composition section, removing the H2O peak does decrease the H content, and the range of mass composition for the hydrogen also decreases. Finally, the "Adj" or Adjusted composition is shown, in which the CO, CO_2, and HO family ion were removed from the mass spectra shows almost identical mass compositions for the 4, 12, and 20 hour time points. Removing the CO and CO_2 removes the variability seen in the hydrogen composition, and removing the H_2O as well doesn't change the trends further.

Discussion

Mass Spectrometry offers an additional method to characterize hydrochar, which can corroborate the findings from other methods of analysis, or disagree and provide an opportunity to come to a greater understanding of the analytical techniques as they apply to amorphous carbon materials. The ion trends provided a way of identifying and quantifying different structures within the hydrochar, such as aromatics, furanics, aliphatics, and functional groups. Based on work studying saccharide decomposition in subcritical water and the products that form, the chemistry of hydrochar is proposed to change with reaction time as follows:

1. Aromatic content increases with reaction time relative to the furan content. Luijkx et al. showed 1,2,4-benzenetriol (BTO) forms from 5-HMF [98]. Chuntanapum and Matsumura gave evidence that BTO is incorporated in the structure of hydrochar, with hydrochar forming from cooled reaction liquids containing BTO, and BTO disappearing with reaction time [41]. BTO was also used as a reactant for humin formation by van Zandvoort et al., which showed 100% conversion of the BTO, increased conversions of the sugar (relative to no BTO added), larger humin mass yield, and the

IR and NMR showed aromatic content to increase [82]. BTO is therefore believed to be highly reactive and incorporated in the hydrochar structure. It is believed to form in greater amounts with reaction time, as it forms from 5-HMF.

2. The number of multi-ring aromatics relative to the number of single-ring aromatics increases. Multi-ring aromatics form from single-ring, and may have slow reaction kinetics.

3. The number of 3-ring arenes increases relative to the number of 2-ring. Raman Spectroscopy indicated increasing aromatic domain size between 2 and 3 rings.

The first pattern can be examined by the mass spectrometry mass ratio of aromatics to furans, which is shown in Figure 49. The arene to furan ratio clearly increases with reaction time from 3 to 16 hours, effectively doubling in intensity. All of the arenes show similar trends of sharp increases from 4 to 12 hours, and the furan fragment $C_5H_5O_2$ decreases sharply from 3 to 4 hours. The trend resembles the mass yield of hydrochar with reaction time.

The second pattern can also be examined by the mass spectrometry, by the ratio of 2- and 3-ring aromatics compared with the 1-ring aromatics, which is shown in Figure 50. The trend appears to be increasing with reaction time, but the change is small. Clearly 1-ring aromatics are present in the structure of hydrochar, which means they contribute towards the Raman spectra.

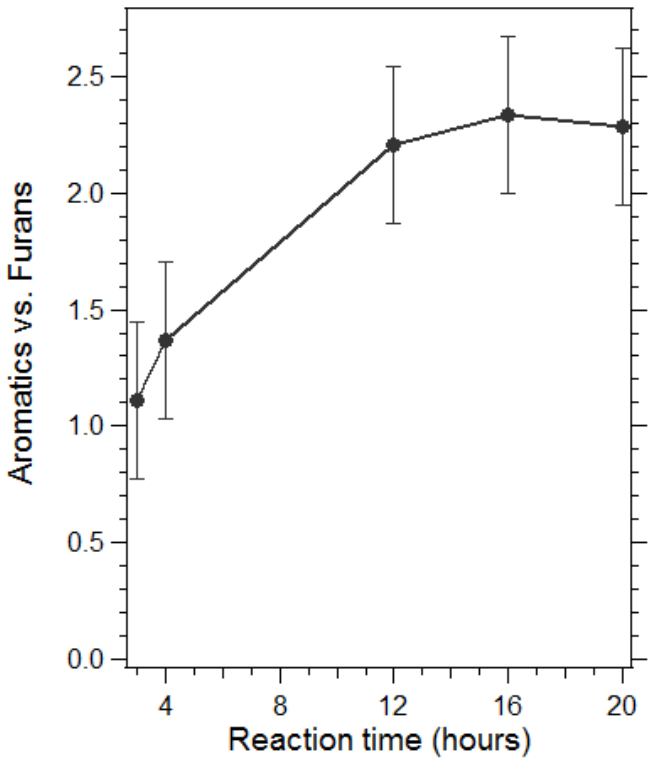

Figure 49. AMS aromatic vs. furan ions as a function of reaction time. Aromatics ions: C_6H_5, C_7H_7, C_9H_7, $C_{10}H_8$, $C_{11}H_{10}$, $C_{12}H_8$, $C_{14}H_8$, $C_{14}H_{10}$. Furan ions: C_6H_7O, $C_5H_3O_2$, $C_5H_4O_2$, $C_5H_5O_2$.

According to Brown et al., the structure of hydrochar indicates aldehyde-functionalized 2- and 3-ring aromatics based on the agreement with the simulated values, while the 1-ring aldehyde-functionalized arene differs in D band position by 140 cm^{-1}, G band position by 30 cm^{-1}. 1-ring arenes are believed to be incorporated in the structure of hydrochar based on the formation of aromatics such as 1,2,4-benzenetriol and 1,4- benzenediol [41].

The Raman Spectroscopy study by Brown et al. suggested the presence of 2- and 3-ring aldehyde-functionalized arenes in the structure of hydrochar [37], and the Raman section of this study indicated that the amount of 3-ring arenes increases with respect to the number of 2-ring arenes. The AMS ratio of 3-ring arenes to 2-ring arenes as a function of reaction time is shown in Figure 51, which appears to be decreasing with reaction time. The ratio increases from 3 to 4 hours, before decreasing sharply

afterwards. The decreasing 2-ring/3-ring pattern goes against the Raman method, which requires explanation.

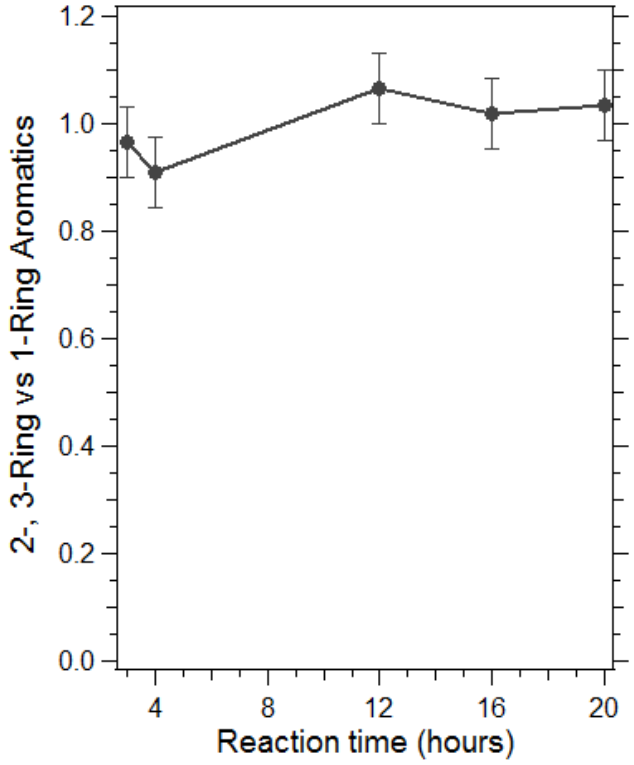

Figure 50. AMS 2- and 3-ring vs. 1-ring aromatic ions as a function of reaction time.

The simulated Raman prediction was based off aldehyde-functionalized 2- and 3-ring arenes, but the ions tracked are not aldehyde-functionalized, as they contain only carbon and hydrogen, and further, the organic compounds believed to introduce aromaticity to hydrochar (1,2,4 benzenetriol, 1,4 benzenediol)[41] are also not believed to be aldehyde-functionalized, but rather are alcohol-functionalized. So this indicates that either the Raman trends are not indicating an increased 3-ring/2-ring ratio, or the AMS method is not properly tracking the 3- and 2-ring arenes in hydrochar.

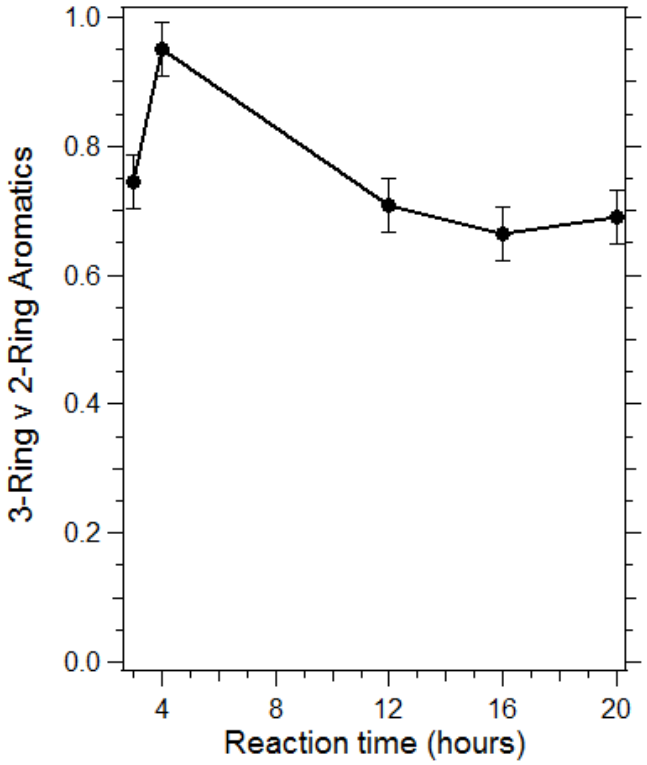

Figure 51. AMS 3-ring vs. 2-ring aromatics as a function of reaction time.

The trends shown in Figure 49, Figure 50, and Figure 51 can be compared with the Raman trends shown in Figure 31 and Figure 32, using the simulations by Brown et al. for the expected spectroscopic behavior of 1-, 2-, and 3-ring arenes and single furans [37]. The 1-ring (aldehyde-functionalized) arene G band position is 1603 cm^{-1}, while the 2-ring and 3-ring (aldehyde-functionalized) positions are 1571 cm^{-1} and 1558 ± 8 cm^{-1}, compared to the fitted position of 1584 cm^{-1}, which shifts to lower wavenumbers. If there is less 1-ring aromatics with increasing reaction time, the 1-ring arene contribution at higher wavenumbers will decrease, effectively red-shifting the position, which agrees with the trend in G band position. The D band positions for 1-, 2-, and 3-ring arenes (aldehyde-functionalized) are 1192, 1354, and 1360 ± 30 cm^{-1} respectively, while the fit position is 1333 cm^{-1}. The D band position for the 1-ring arenes is so far from the actual fit that any change in 1-ring arene content wouldn't change the position of the D band in hydrochar. However, if the relative amount of 2-ring and 3-ring aromatics increase relative to the amount of 1-ring aromatics, the D/G ratio would increase. This is because the 1-ring aromatics affect the size of

the (fit) G band, but not the D band, as it the 1-ring D band is over 100 cm-1 away. Further, the simulated D/G intensity of 0.26 for 1-ring (aldehyde-functionalized) is much less than the aldehyde-functionalized 2-ring or 3-ring arene values of 1.1 or 3.8 ± 0.5 respectively. The hydrochar D/G ratio increases from 0.56 to 0.57 from 4 to 12 hours, which agrees with the shift from 1-ring to 2- and 3-ring aromatics. The Kekulé band does not exist for 1-ring aromatics, so the Kekulé/G or Kekulé/D ratios should increase with increasing multi-ring arenes relative to single-ring arenes, and the Kekulé/G ratio does in fact increase from 0.31 to 0.34 from 4 to 12 hours. Given the large magnitude of changes in G band position (from 1571 cm^{-1} and 1558 ± 8) and D/G intensity ratio (from 1.1 to 3.8 ± 0.5) from 2-ring arene to 3-ring arenes, the change in the Raman spectra is more likely due to the relative decrease in single-ring arenes and increase in 2- and 3-ring arenes than an increase in average ring size between 2 and 3 rings.

The Raman analysis by Brown et al. can also provide insight into the effect of a decreasing furan content with a relatively increasing aromatic content. While the aldehyde-functionalized furan has G and D positions at 1584 ± 20 and 1342 ± 54 cm^{-1} respectively which are very close to the fit peak positions in the hydrochar, the K/G and D/G ratios of the furan are such that the furan mode (Kekulé mode for furan) is much larger than the D and G modes, and the Kekulé mode is located at 1500 cm^{-1}. If the Raman of hydrochar was sensitive to the change in the furan content, then a decrease would be seen at 1500 cm^{-1}. Since there is no change at this location, it is safe to conclude that the Raman is not sensitive to the change in the furan content.

If 2- and 3-ring arene content increases with reaction time (2- and 3- ring G positions of 1571 cm^{-1} and 1558 ± 8 cm^{-1} , and 2- and 3-ring D positions of 1354 and 1360 ± 30 cm^{-1}) which are at lower and higher positions than the aldehyde-functionalized furan, then the G and D band positions are expected to red-shift and blue-shift respectively. The G band position does red-shift from 4-hours (at 1584 cm^{-1}) to 1580 for 8-24 hours, while the D band position does not blue-shift, but weakly red shifts from 1333 to 1332 cm^{-1}. The G band position agrees while the D band position weakly disagrees. The D/G ratio for furan is

3.9 ± 3.5, while the D/G ratio for 2- and 3-ring aromatics is 1.1 and 3.8 ± 0.5. The actual D/G ratio of hydrochar is much lower, at 0.56, which indicates that furan and 3-ring arenes are not as prominent. If the furan content decreases with reaction time, the D/G ratio would decrease, indicating that furan content does not decrease appreciably with reaction time. The Furan mode (the Kekulé mode in arenes) has a position of 1497 ± 28 cm^{-1}, while the 2 and 3-ring arenes have Kekulé positions of 1439 and 1458 ± 20 cm^{-1} respectively. The blue-shift seen in Kekulé position with reaction time (from 1435 to 1438 cm^{-1}) would not be affected by a decrease in the Furan mode, which occurs at 1497 cm^{-1}, and further the closest band to the Furan mode, the G_L band at 1506 cm^{-1}, does not change in intensity with reaction time. The K/G intensity ratio of 19.5 ± 18.5 for furan is much larger than the 0.31 and 0.6 ± 0.1 seen for 2- and 3-ring arenes, and is much larger than the hydrochar K/G ratio of 0.31. A decreasing furan content decreases the K/G ratio, while the K/G ratio of hydrochar increases with reaction time.

With five independent Raman parameters for furan content, only two (G band position and D band position) agree with the hydrochar fitting, and the only trend that is consistent with a decreased furan content to a 2- and 3-ring arene content is the G band position trend. The G band position trend is also seen with increased 2- and 3-ring arene content relative to 1-ring arene content and increased 3-ring arene content with respect to 2-ring arene content. The increased arene content, relative to the furan is not represented by the Raman, which seems to be more sensitive to the aromatic content. The decrease in furan composition could be misinterpreted because of the strong decrease seen in the $C_5H_5O_2$ ion, and there could be additional furan peaks that are not properly attributed.

Conclusions

Mass Spectrometry shows good agreements with the IR, identifying furans, aromatics, alcohols, aliphatics, and ketones. The mass spectrometry agrees with the Raman Spectroscopy, showing the presence of 2- and 3-ring arenes, but disagrees with the Raman which does not indicate changes in the furan content. Mass spectrometry indicated the alcohol functionality decreases with reaction time, and the furan

content decreases relative to the aromatic content, which increases with reaction time. The mass spectrometry trends also indicate that the 2-ring and 3-ring arenes increase relative to the 1-ring arenes, and do not show a change in the ratio of 3-ring arenes to 2-ring arenes. The Raman Spectroscopy analysis by Brown et al. found the presence of 1-ring arenes unlikely due to the D and G band positions for both benzene and benzaldehyde, arguing instead for aldehyde-functionalized 2- and 3-ring arenes. Based on this analysis, the time trends in the G position, D/G intensity ratio, K position, and K/G intensity ratio indicated the average aromatic size is increasing between 2 and 3 rings. The Raman and mass spectrometry trends were found to be in agreement for the shift in aromatic content from 1-ring to more 2- and 3-ring. The Raman fitting was not sensitive to changes in the furan content, and a decrease in furan content with reaction (while seen in the mass spectrometry) was not consistent with the Raman parameters.

Conclusions

This characterization study of hydrochar chemistry as it forms with reaction time shows the material to change noticeably between reaction times of 4 and 8 hours. The elemental oxygen and hydrogen content decrease while the carbon content increases. IR Spectroscopy shows aliphatic, furan, and aromatic content, as well as alcohol and ketone functionality. The IR indicates changes between hydrochar prepared at 4 hours and 8-24 hours, with an increase to the C=C vibration and decreases to furan modes at 1515 cm^{-1} and 1030 cm^{-1}. Two unattributed minor bands disappear after 4 hours.

The Raman spectra of hydrochar indicates 2- and 3-ring aldehyde-functionalized arenes along with aldehyde-functionalized furans. With reaction time, the Raman spectra of hydrochar indicates increasing amounts of 3-ring aromatics relative to 2-ring aromatics.

Mass Spectrometry is applied to hydrochar for the first time, and is established as a reproducible technique. Mass Spectrometry identifies methyl groups, furan, and aromatic structures as well as alcohol and ketone functionality, consistent with the IR. In addition, the mass spectrometry also identifies 2- and 3-ring arenes which supports the Raman interpretation. The mass spectra changes with reaction time show a strong increase in the aromatic character relative to the furan and an increase in the 2- and 3-ring arene content of hydrochar relative to the 1-ring. The increase in multi-ring relative to single-ring arene content is consistent with the trends observed in the Raman. Further, the mass spectrometry shows the ratio of 2-ring to 3-ring arenes remains constant in the hydrochar with reaction time. The mass spectra contains multiple furan ions which, unlike the aromatic ions, show several different composition trends with reaction time, indicating different furan functionality types in the hydrochar which change with reaction time. The mass spectra also indicates the alcohol functionality decreases with reaction time.

The IR Spectroscopy, Raman Spectroscopy, and Mass Spectrometry techniques provide valuable insight into the structural and functional components of hydrothermal carbon. These insights can be applied to

understanding the underlying chemical properties responsibility for performance of hydrochar under different applications, such as aqueous heavy-metal adsorption. In such a case, the performance would be expected to depend on the hydrophilicity of the material. With reaction time, the methyl content of hydrochar increases, aromatic content increases while furans decrease, and hydroxyl and/or carbonyl content decreases. Methyl groups would decrease the hydrophilicity of hydrochar, while hydroxyl content may decrease the ability of the hydrochar to interact with and adsorb heavy metals. Selection of reaction conditions that increase the hydrophilicity and amount of acidic functional groups may improve adsorption performance, and the methods and insights developed can assess the changes to these functional groups and structures after processing conditions are applied to modify them.

Recommendations

Hydrochar Synthesis Methodology

Reproducible synthesis of hydrochar has proven to be surprisingly difficult. Hydrochar changes with reaction time, and it can change as a result of the heating and cooling profiles. In the preliminary stages of this study, hydrochars were prepared with a 10-11 hour cooling time and by a quenching run, where a large bucket was filled with water and ice. When the reaction time was complete, the oven was turned off and the reactor was placed in the bucket, cooling it down over the course of just a few minutes. The reactor was left closed for about half an hour, to allow it to depressurize. Then, the hydrochar was washed, filtered, and dried in the methods described. The hydrochars prepared by the two methods were tested by elemental analysis (just for the carbon fraction, courtesy of Leco, Inc.) and showed a lower elemental carbon percentage than the normally cooled materials. This held for chars prepared at different reaction times and of different sugar feedstock (xylose was also tried at this stage).

Raman Spectroscopy

Raman Spectra Quality

The Raman fitting method with variable G, D, and Kekulé peak positions is sensitive to the noise of the spectra. Standards were put in place so the signal strength would be sufficiently strong compared to the fluorescence, however the noise should have been filtered to a better degree. Line smoothing features were included in the LabSpec 6 software for the Raman Spectrometer (Horiba X-Plora, Horiba Scientific Inc.) but the setting should have been increased beyond a setting of 1.

Raman Fitting Method Verification

The Raman fitting method should be verified by additional studies, to see how well the fitting indicates molecular structures. Hydrochars prepared from xylose are believed to have greater aromatic content, while those prepared from HMF are expected to be more furanic in nature. The gap between the expected behavior of positions and intensity ratios can

Mass Spectrometry

Vaporizer Settings

The mass spectrometer used in this study, the Soot Particle Aerosol Mass Spectrometer (Aerodyne Research Inc.), is designed specifically to study carbon aerosol particles, with dual vaporizers for different carbon particles. The resistively heated tungsten conductively heats the incoming samples to 600 °C, which is enough heat for most organic matter. For black carbon, 600 °C is below the heat of vaporization, and this fraction will not be detected by the instrument (as it is not vaporized and will not ionize and enter the detector). To overcome this, an infrared laser is used to heat the particle and vaporize black carbon. In this study the laser and thermal vaporizer were used, and the effect of running with only one vaporizer was briefly examined. Using only the thermal vaporizer, the mass spectra was dominated by fragmentation products (CO, CO_2, C_2H_3O, H_2O, etc.). Using only the laser vaporizer (without heating the tungsten vaporizer the temperature remained at 250 °C) the Cx ions (C^+, C_3^+) were suppressed, but less CO_2 and H_2O formed. One effect that was not explored in depth in this study was the problem that hydrochars prepared at different reaction times might vaporize differently in the mass spectrometer because they have different properties. The 4-hour hydrochar is a light brown color, while the 3-hour hydrochar and hydrochars prepared with 8 hour or longer reaction times are dark brown. If the 4-hour hydrochar does not absorb the laser radiation and does not heat up like the other hydrochars, it may not show the same fragmentation products, or it instead shows more thermal decomposition products.

Application of Hydrochar for Adsorption of Aqueous Heavy-Metals

Hydrochar is a promising material for adsorption of heavy metals, and has shown strong performance, with adsorption capacities of 326 mg/g and 351 mg/g with simple modifications such as air-drying 24 and acrylic acid addition to the reaction respectively 23. These studies employed IR spectroscopy XPS, and 1-D NMR spectroscopy (between the two) to study the chemical composition of the material, and there was not a lot of insight into additional modification of the material to further increase performance. With the

methods developed in this study, there is much more chemical information available to understand the performance and how the material changes under performance conditions.

Appendix

Hydrochar Synthesis- Yield Data

Table 7. Hydrochar Synthesis Yield Data

Reaction Time [Hours]	Sample Date	Dry Char Mass, [g]	Initial Mass Glucose [g]	Mass yield %	Average Yield by Reaction Time
4	22-Apr	1.04	24.0	4.3%	2.4%
4	2-Jun	0.49	23.4	2.1%	
4	2-Sep	0.16	23.6	0.7%	
4	27-Sep	0.62	23.7	2.6%	
8	23-May	5.31	23.5	22.6%	22.7%
8	25-May	5.7	23.5	24.3%	
8	6-Jun	5.4	23.4	23.1%	
8	25-Oct	4.89	23.6	20.7%	
12	6-May	7.04	23.7	29.7%	30.7%
12	21-May	7.1	23.6	30.2%	
12	30-May	7.1	23.4	30.3%	
12	7-Jun	7.61	23.4	32.5%	

16	29-May	7.76	23.4	33.2%	34.5%
16	7-Oct	8.27	23.7	34.9%	
16	13-Oct	8.36	23.7	35.3%	
20	8-Mar^{-1}7	8.14	23.4	34.8%	34.8%
24	18-May	8.11	23.5	34.5%	35.5%
24	3-Jun	8.56	23.4	36.6%	
24	14-Sep	8.7	23.5	36.9%	
24	23-Sep	8.46	23.6	35.8%	
24	8-Nov	8.01	23.7	33.9%	
72	23-Mar^{-1}7	8.10	23.7	34.2%	34.2%

Reactor Heating and Cooling Profiles

Hydrochar heating and cooling profiles are shown in Figure 52 and Figure 53. The profiles were collected by strapping a thermocouple to the outside of the metal autoclave, and was held in place by a metal band. The oven control system has two input parameters: the desired temperature, and the max allowed temperature, which were set to 180 and 200 °C respectively. As shown from Figure 2, it takes about 1 hour to reach 160 °C, and 1.5 hours to reach 175 °C. This indicates that the effective reaction time is much lower than 4 hours, because of the slow heating time. Further, the amount of time spent at elevated temperatures below 180 °C is significant. This is also seen in Figure 3, the cooling profile is shown for 10 hours, as the autoclaves were removed from the oven between 10.5 and 11 hours.

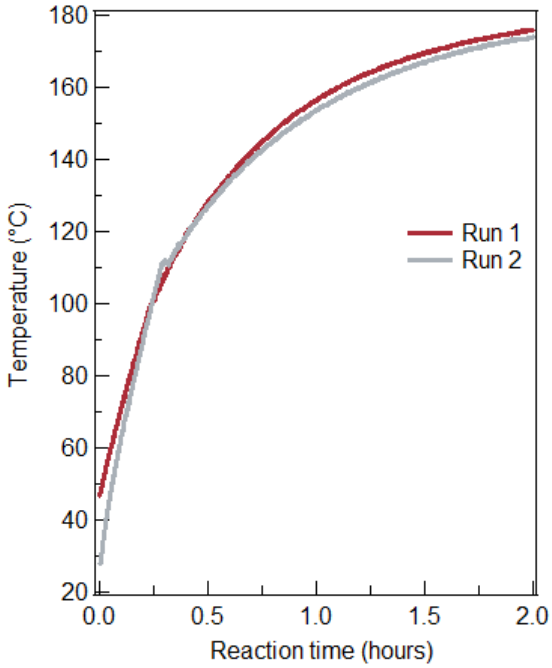

Figure 52. Heating profiles for hydrochar runs. The two lines represent two different reaction runs.

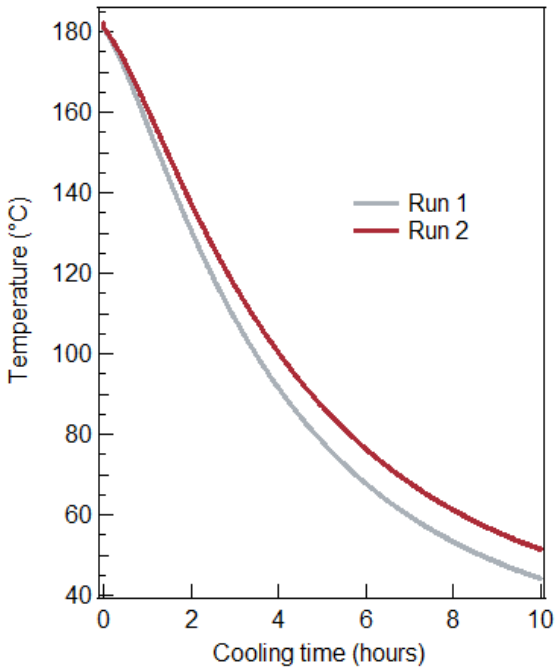

Figure 53. Cooling profiles following hydrochar runs. The two lines represent two different reaction runs.

Hydrochar Reactor

Figure 54. Autoclave (left) and teflon liner (right). The caps are shown next to the container. The Teflon liner cap is held in place by the autoclave cap, which is screwed in place using a hex key.

Figure 55. Teflon autoclaves used during hydrochar prep. The autoclave on the right was used for the vast majority of the hydrochar preps. 3-hour, 20-hour, and 72-hour synthesis time hydrochars were prepared using the autoclave on the left.

The hydrochar reactor was cleaned before each use. It was washed with soap and water, then rinsed with ethanol. It was also wiped using KimWipes and ethanol until no residue would show on the KimWipe. The reactor was then rinsed with DI water repeatedly, then dried with a Kimwipe.

Hydrochar Appearance

Figure 56. 4-hour hydrochar, after drying.

Hydrochars prepared at 4 hours were a light brown. When grinding this char, it seemed very sticky and was difficult to grind. In addition, this char appeared to be much denser than later chars, and was not a fine powder until ground, but still seemed to be sticky. By contrast, chars prepared at 8 hours and beyond appeared to be similar to each other, and different from the 4 hour char. They appeared to be darker than the 4 hour char and had very little resistance to grinding. Further, chars prepared after 8 hours seemed to form aerosols during handling, something the 4 hour char did not.

Elemental Analysis

Raw Elemental Data- Mass form

By mass, the majority of the hydrochar is carbon, at around 65%. About 25% is oxygen, with only about 4% hydrogen by mass. Pyrolyzed hydrochar appears to have much less hydrogen. Carbon black has the least amount of hydrogen and oxygen of the materials tested.

All materials are below 100% in the sum of the measured mass % of C, H, and O, with an average sum of 94 % for hydrochars and pyrochar. The significant lack of closure to 100% is not due to the presence of other elements, as the feedstocks (glucose, DI water) contain only carbon, hydrogen, and oxygen. Furthermore, at the temperature of the reaction, the gaseous oxygen and nitrogen present in the reactor would not react with the material. The closure in the mass % could be due to the lack of thermal stability of the material. The C & H % is found by combustion of the sample under oxygen gas at 990 °C into CO_2 and H_20, while the O % is determined by pyrolysis at 1000 °C. Since the material has a significant oxygen content and is not graphitized, it could form side products that are difficult to quantify. Likewise, the method of oxygen quantification is also a thermal degradation technique, using pyrolysis (under nitrogen atmosphere) to form CO. Carbon black, by comparison, has a better mass closure of 96%, perhaps because the material has a much better thermal stability and a lower O content, making for a better conversion to CO_2 or CO.

Table 8. Raw Elemental Analysis data. Reported on a mass basis.

HTC Rxn Time	Sample	Mass %O	Mass %C / %H	Mass %C/%H replicate
4	4hg 9/27	26.67	63.25 / 4.19	
8	8hg 10/25	27.66	64 / 4.12	

12	12hg S1 (5/21)	23.85	64.71 / 3.71	65.02 / 4.07
12	12hg S2 (5/06)	23.88	65.48 / 4.07	65.38 / 4.28
12	12hgS3 (6/07)	27.2	65.38 / 4.05	65.51 / 4.08
16	16hg 10/13	24.11	65.25 / 4.21	
24	24hg 6/03	24.38	64.63 / 4.13	
8	8hg 10/25 pyr.,500C, 10h	21.03	68.72 / 1.77	
N/A	Carbon Black, Regal Black 400(Cabot)	3.32	92.45 / 0.71	

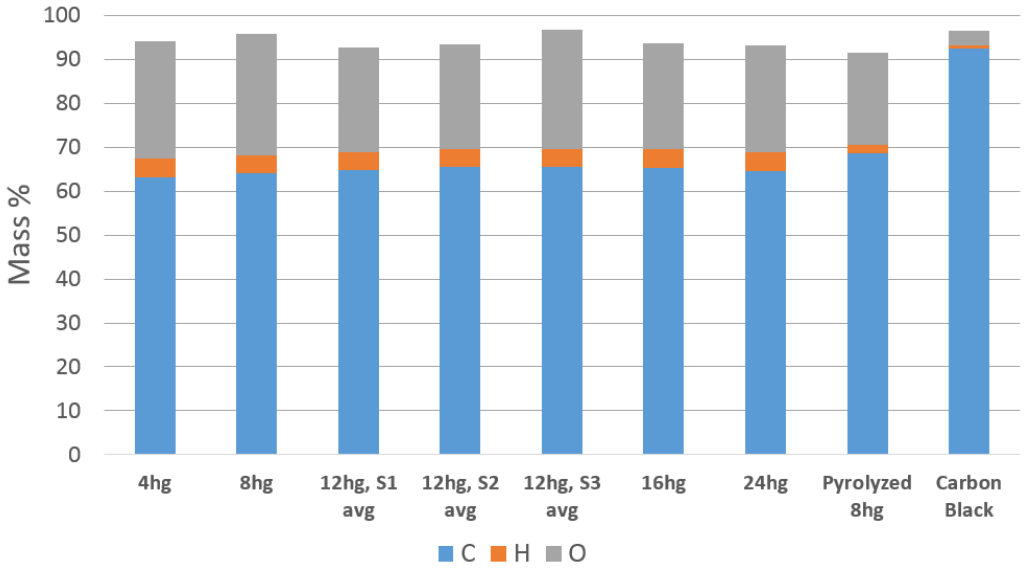

Figure 57. Bar Graph of Elemental Mass % C, H, and O raw data. C and H for the 12hg samples are the average of the two CH analyses.

Elemental Data Atomic %

Raw mass compositions were converted into atomic percentages as follows:

$$C\ at.\% = \frac{C\ mass\ \% * \left(\frac{1\ mol\ C}{12\ g\ C}\right)}{\left(C\ mass\ \% * \left(\frac{1\ mol\ C}{12\ g\ C}\right)\right) + \left(H\ mass\ \% * \left(\frac{1\ mol\ H}{1\ g\ H}\right)\right) + \left(O\ mass\ \% * \left(\frac{1\ mol\ O}{16\ g\ O}\right)\right)}$$

$$H\ at.\% = \frac{H\ mass\ \% * \left(\frac{1\ mol\ C}{12\ g\ C}\right)}{\left(C\ mass\ \% * \left(\frac{1\ mol\ C}{12\ g\ C}\right)\right) + \left(H\ mass\ \% * \left(\frac{1\ mol\ H}{1\ g\ H}\right)\right) + \left(O\ mass\ \% * \left(\frac{1\ mol\ O}{16\ g\ O}\right)\right)}$$

$$O\ at.\% = \frac{O\ mass\ \% * \left(\frac{1\ mol\ C}{12\ g\ C}\right)}{\left(C\ mass\ \% * \left(\frac{1\ mol\ C}{12\ g\ C}\right)\right) + \left(H\ mass\ \% * \left(\frac{1\ mol\ H}{1\ g\ H}\right)\right) + \left(O\ mass\ \% * \left(\frac{1\ mol\ O}{16\ g\ O}\right)\right)}$$

Table 9. Elemental Data Atomic Composition.

HTC Rxn Time	Sample	Atomic %O	Atomic %C / %H	%C/%H replicate (if applicable)
4	4hg 9/27	14.98	47.37 / 37.65	
8	8hg 10/25	15.46	47.70 / 36.84	
12	12hg S1 (5/21)	13.82	50.91 / 35.02	49.35 / 27.07
12	12hg S2 (5/06)	13.42	49.52 / 36.94	48.56 / 38.14
12	12hgS3 (6/07)	15.15	48.65 / 36.17	48.57 / 36.30

16	16hg 10/13	13.51	48.75 / 37.743	
24	24hg 6/03	13.80	48.79 / 37.41	
8	8hg 10/25 pyr.,500C, 10h	14.92	64.99 / 20.09	
N/A	Carbon Black, Regal Black 400(Cabot)	2.41	89.36 / 8.24	

IR Spectroscopy

Transmittance mode reproducibility

Spectral Reproducibility

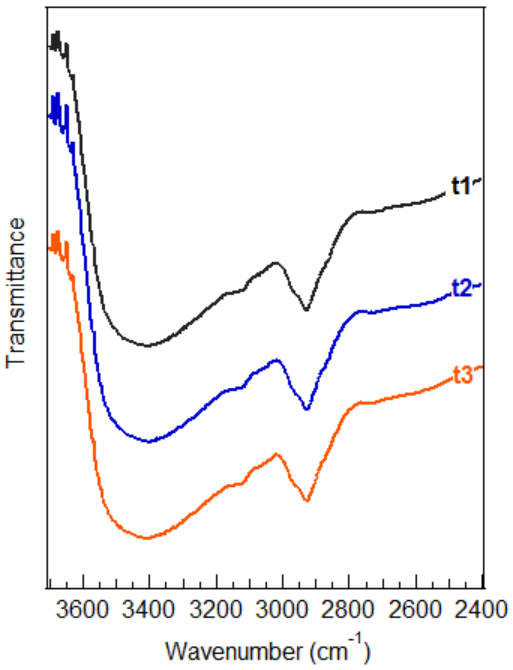

Figure 58. DRIFTs Spectra of 16hg collected on the same date of the same sample. Spectra were normalized by equal area under the curve and evenly spaced.

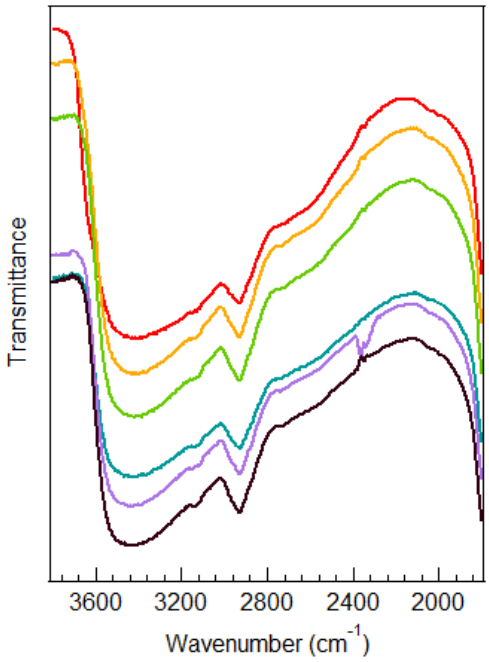

Figure 59. DRIFTS spectra of 4hg spectra collected at different times and temperatures in the DRIFTS, operating to dry the sample. Red: 50 °C, Orange 80 °C, Green 100 °C, Blue 120 °C, Purple 150 °C for 1 hour, Black 150 °C for 2 hours.

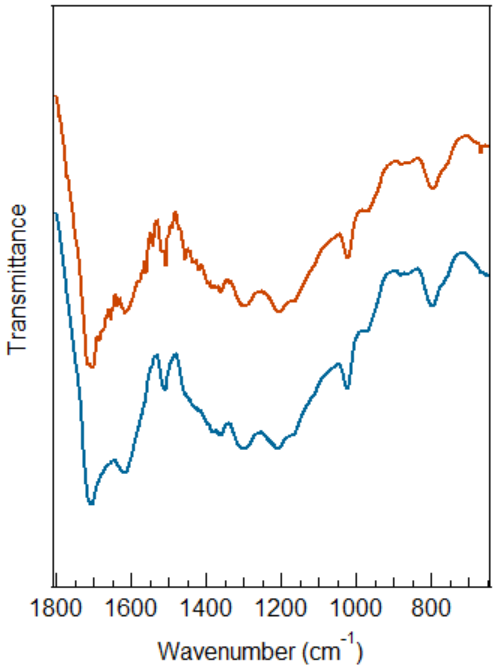

Figure 60. Transmittance mode IR spectra of 8hg, prepared from hydrochars prepared on different days. The spectra were not normalized by intensity.

Raman Spectroscopy

Spectra Selection Criteria

During the collection of Raman spectra of hydrochar, the hydrochar starts to fluoresce, resulting in an increasing background, which impacts the signal interpretation. The background needs to be subtracted from the spectra to give the Raman spectra that can be fit. The background subtraction assumes that the background follows that shape shown, so the fluorescence introduces uncertainty into the procedure, and increases with increasing fluorescence. To address this, a metric for the signal strength relative to the fluorescence is defined, which is termed here the signal to fluorescence, or S/F, and a cutoff is established. The calculation of the cutoff factor is shown in Figure 61 and expressed in the equation. The spectra used have a S/F ratio greater than or equal to 2.0.

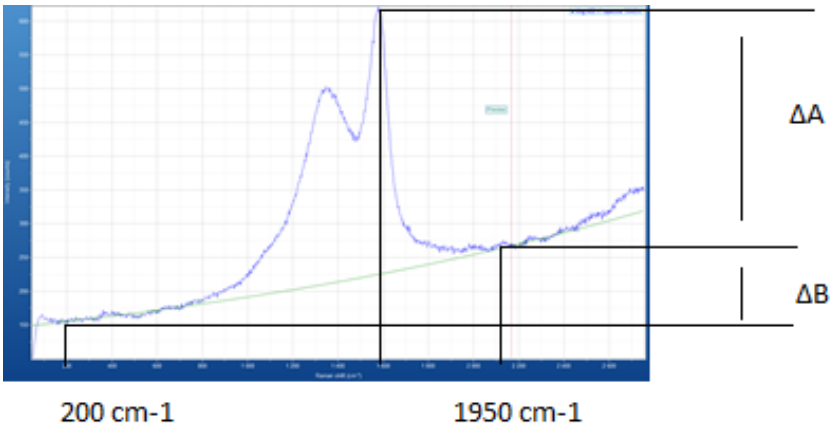

Figure 61. Raman Spectra showing how the Signal to Fluorescence (S/F) is calculated.

$$Signal\ to\ Fluorescence\ Ratio\ (S/F) = \frac{I_{max} - I_{1950\ cm^{-1}}}{I_{1950\ cm^{-1}} - I_{200\ cm^{-1}}} = \frac{\Delta A}{\Delta B}$$

Alternative Raman Fitting

Methods

The Raman fitting method ultimately used was one of several methods with variable Kekulé, D Band, and G Band positions. Here the methods are explained and shown with the results of the fitting. The variable fitting method 3, or V3, is the method shown in the results section, but is re-introduced here for clarity.

All methods fit the spectra using MagicPlot ver. 2.5 (Magic Plot Systems, LLC). A version of the software (MagicPlot Student) is available as a free download (http://magicplot.com). Gaussian peaks of fixed equal half-width half maxima (HWHM value of 47 was used) were used to fit the Raman spectra by least squares regression method over the range 1000-1750 cm^{-1}. The fit peaks are identified in Table 4 along with their respective positions.

Variable Method 1

Set all fit peak positions as shown in Table 4. All peak positions are to be fixed in this stage. After the first fitting, lock the fit area of the CH_2/CH_3 band and unlock the position of the Kekulé, which fits the Kekulé to position of best fit. Perform sum of least squares calculation. The resulting peak location of the Kekulé is then locked in place and the D Band position is allowed to vary in position. The spectra is refit, and the new D Band location is locked in place. After this, the G Band position is allowed to vary with the fitting, and the fitting is repeated. If the G-Resonance position does not fit for a positive value, delete the G-Resonance and restart the fitting from the beginning, with all bands at their original locations.

Variable Method 2

Fix all fit peak locations to the ones shown in Table 4. After the first fitting, the position of the G Band allowed to vary and the fitting is repeated. The resulting peak location of the G Band is then locked in place and the process is repeated with the Kekulé allowed to vary in position. The spectra is refit, and the new Kekulé location is locked in place. After this, the D Band position is allowed to vary with the fitting, and the fitting is repeated. This gives the final fit of the spectra.

Variable Method 3

Fix all fit peak locations to the ones shown in Table 4. After the first fitting, unlock the position of the G Band and repeat the fitting. The resulting peak location of the G Band is then locked in place and the process is repeated by varying the D Band position in the fitting. The spectra is refit, and the new D Band

location is locked in place. After this, the Kekulé position is allowed to vary with the fitting, and the fitting is repeated.

If any peaks are negative at this point, lock the area of the lowest peak to zero, reset the band positions, and repeat the fitting. If again, after the Kekulé position is allowed to vary and another peak is fit to a negative value, lock the area of the peak to zero, and unlock the first peak that was locked to zero, and repeat the fitting procedure. If a third time, after both the 1st peak and the 2nd peak were each individually set to a zero value and the system did not fit all positive peaks, lock both peaks to zero area. Repeat the fitting with all bands reset back to their original positions.

Results

Fit Area Percentage Evolution

Fit areas for the ring vibration modes are shown in Figure 62, Figure 63, and Figure 64. All of the trends appear to be similar in terms of peak area and trend shape. The V1 method shows the largest variability in the Kekulé and Asymmetric modes, which is understandable as the V1 method fits the Kekulé band first, while V2 and V3 fit it second and third respectively. In the V1 method, the G Band fit is higher than the V2 and V3, while the G-Resonance is zero at almost all values.

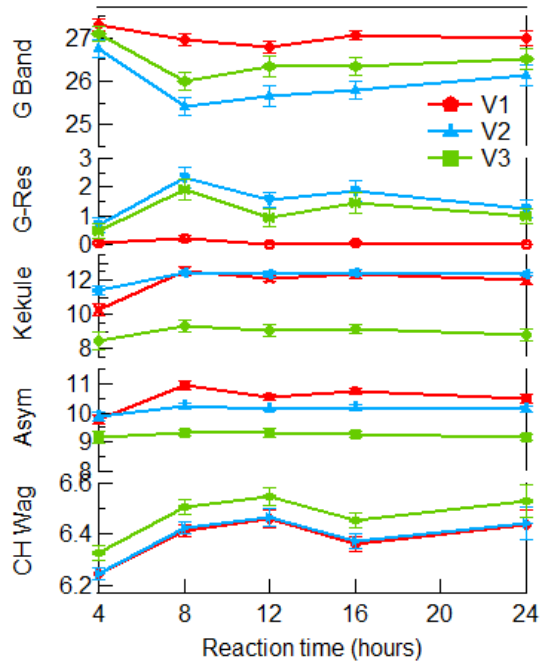

Figure 62. Comparison of the Raman peak area fit by three variable band position methods for ring vibration modes. The V1, V2, and V3 methods are displayed in red, blue, and green respectively.

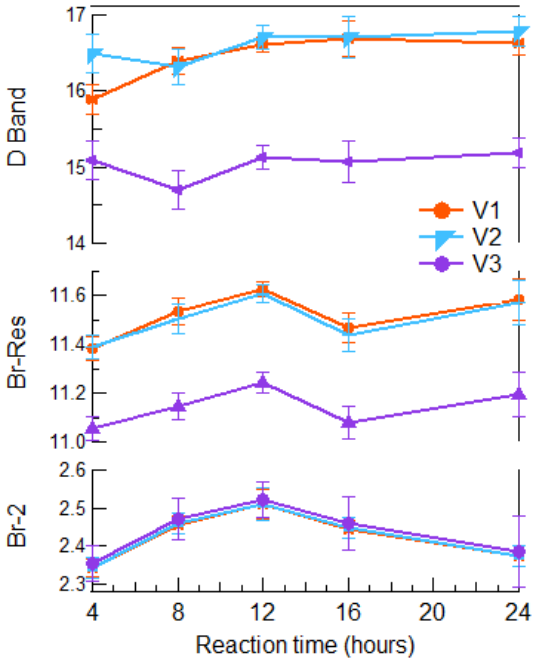

Figure 63. Comparison of the raman peak area fit by three variable band position methods for aromatic breathing modes. The V1, V2, and V3 methods are displayed in orange, blue, and purple respectively.

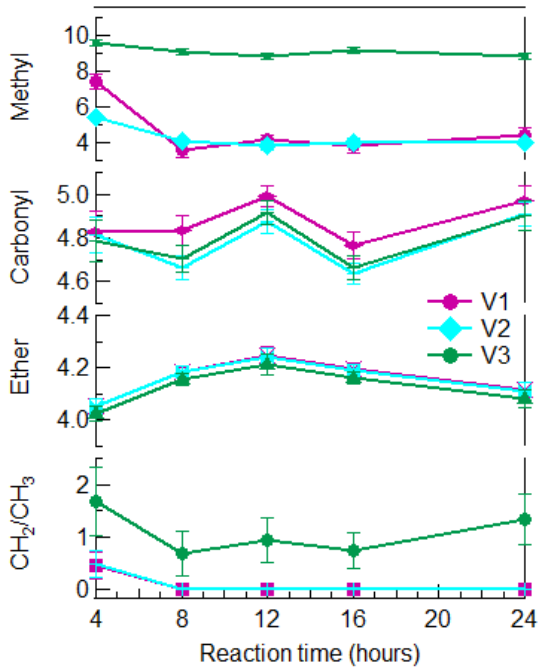

Figure 64. Comparison of the Raman peak area fit by three variable band position methods for functional group vibrational modes. The V1, V2, and V3 methods are displayed in fuchsia, blue, and green respectively.

Band Positions

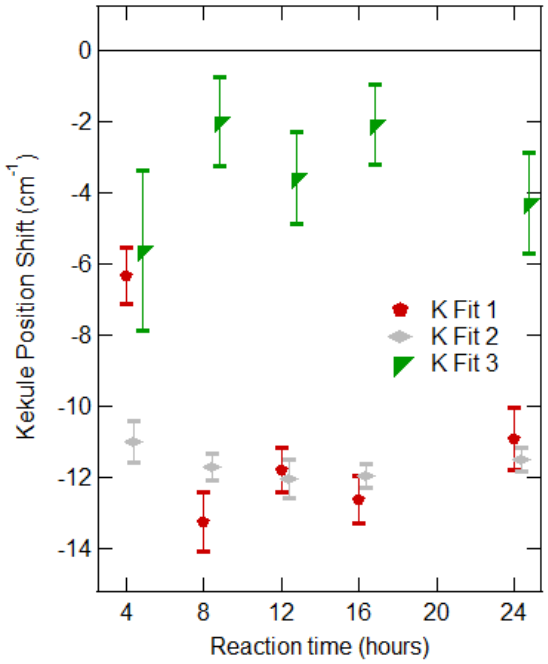

Figure 65. Comparison of the Kekulé band position shift for the three variable position fitting methods. The zero position of the Kekulé band is 1441 cm^{-1}.

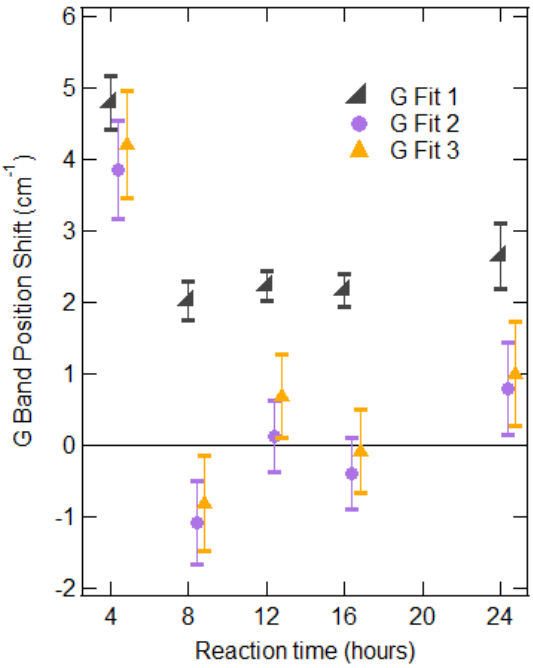

Figure 66. Comparison of the G band position shift for the three variable position fitting methods. The zero position of the G band is 1580 cm^{-1}.

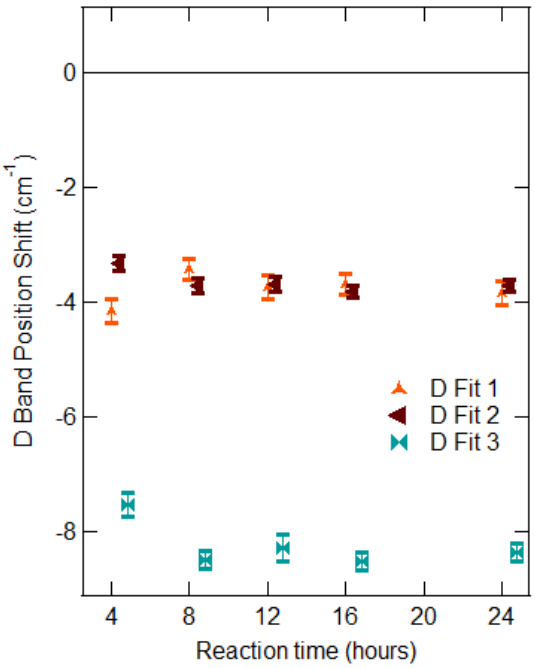

Figure 67. Comparison of the D band position shift for the three variable position fitting methods. The zero position of the D band is 1341 cm^{-1}.

Comparison of r^2 Values

Table 10. Average r^2 values for the three variable fitting methods. r^2 is the adjusted r^2 generated for the peak fitting of the raman spectra in MagicPlot. Not included is the standard deviation to the r^2 value, which ranged from 3E-4 to 5E-4.

Reaction Time (hr)	V1 r^2	V2 r^2	V3 r^2
4	0.9975	0.9972	0.9977
8	0.9977	0.9974	0.9977
12	0.9977	0.9974	0.9979
16	0.9979	0.9975	0.9977
24	0.9977	0.9973	0.9972

Application of Raman Fitting Method of Hydrochar to Pyrolyzed Hydrochar

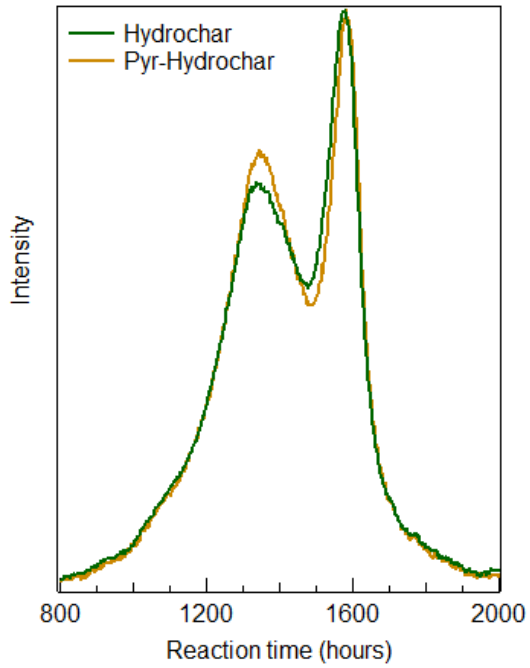

Figure 68. Average Raman spectra of 8-hour hydrochar and pyrolyzed 8-hour hydrochar. Spectra are normalized to have equal area under the curve from 1000-1750 cm^{-1}.

Reproducibility

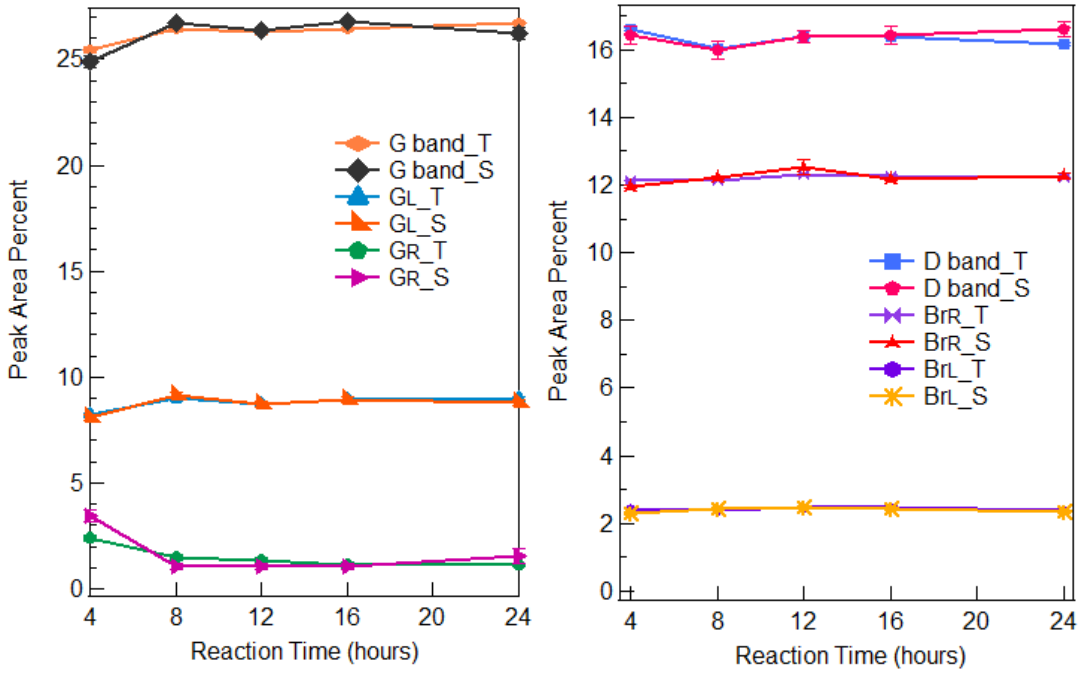

Figure 69. Raman Ring Vibration Modes using the Stationary Fitting Method comparing the set of 1 sample (15 spectra) per time point against 3-5 samples (45-75 spectra) per time point. These are the sample set (S) and full set (F). Full set is denoted by squares, the sample set is denoted by diamonds. From top to bottom: G Band, G-Resonance, Kekulé, Asymmetric, and C-H Wag.

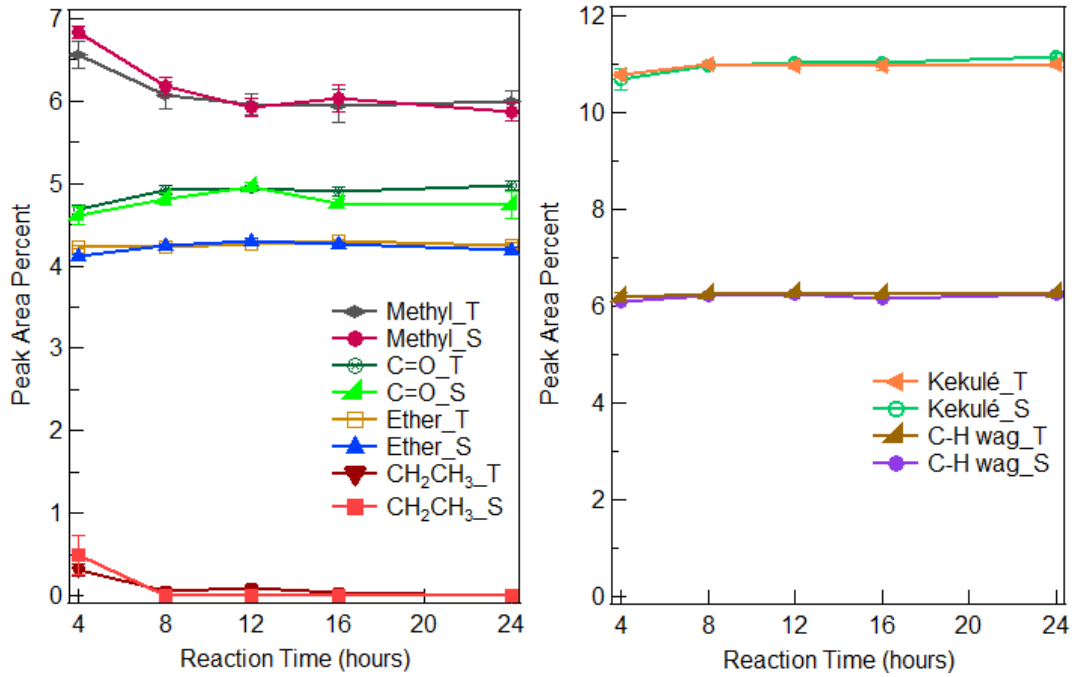

Figure 70. Raman Functional group vibration Modes using the Stationary Fitting Method comparing the set of 1 sample (15 spectra) per time point against 3-5 samples (45-75 spectra) per time point. These are the sample set (S) and full set (F). Full set is denoted by squares, the sample set is denoted by diamonds. From top to bottom: Methyl, Carbonyl, Ether, and CH_2/CH_3.

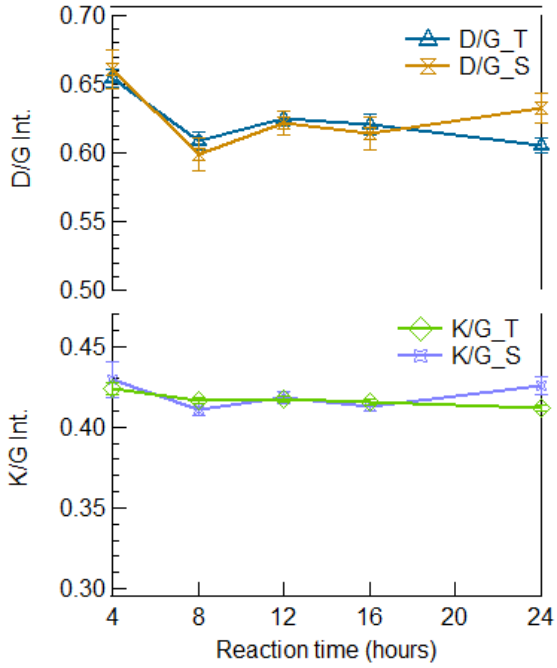

Figure 71. Raman Aromatic Breathing Modes fit using the Stationary Method, comparing the set of 1 sample (15 spectra) per time point against 3-5 samples (45-75 spectra) per time point. These are the sample set (S) and full set (F). Full set is denoted by squares, the sample set is denoted by diamonds. From top to bottom: D Band, Breathing-Resonance, Breathing mode L.

Calculation of the D/G and K/G Area Ratio Error Bars

The error bars for D/G and K/G area ratio (since K,D, and G have the same peak width, these are also the intensity ratios) had to be determined through a propagation of error equation, as error bars or standard deviations could not simply be divided. The propagation of error equation for a ratio x/y is the following:

$$\sigma_{\frac{x}{y}}^2 = \left(\frac{\partial\left(\frac{x}{y}\right)}{\partial x}\right)^2 \sigma_x^2 + \left(\frac{\partial\left(\frac{x}{y}\right)}{\partial y}\right)^2 \sigma_y^2$$

Where $\sigma_{x/y}^2$ is the variance of the ratio x/y, while σ_x^2 and σ_y^2 are the individual variances for x and y respectively. X and Y would be the average values for the peak areas, and σ_x^2 and σ_y^2 are simply the

standard deviations for the peak areas squared. Solving for $\frac{\partial\left(\frac{x}{y}\right)}{\partial x}$ and $\frac{\partial\left(\frac{x}{y}\right)}{\partial y}$ and taking the square root gives $\sigma_{\frac{x}{y}}$, the standard deviation.

$$\sigma_{\frac{x}{y}} = \sqrt{\left(\frac{1}{y}\right)^2 \sigma_x^2 + \left(\frac{-x}{y^2}\right)^2 \sigma_y^2}$$

Gas Sorption Surface Area Measurements

Surface areas were collected by gas sorption measurement using a Quantachrome. The hydrochar was first poured into the glass bulb, and dried overnight at 100 °C in an oven before outgassing at 120 °C for 25 hours on the gas sorption instrument under vacuum. Gas Sorption measurements were taken using nitrogen gas at 77K. The DFT method was applied to the P/P0 range of 0.05-0.3. Measurements are shown in Figure 72.

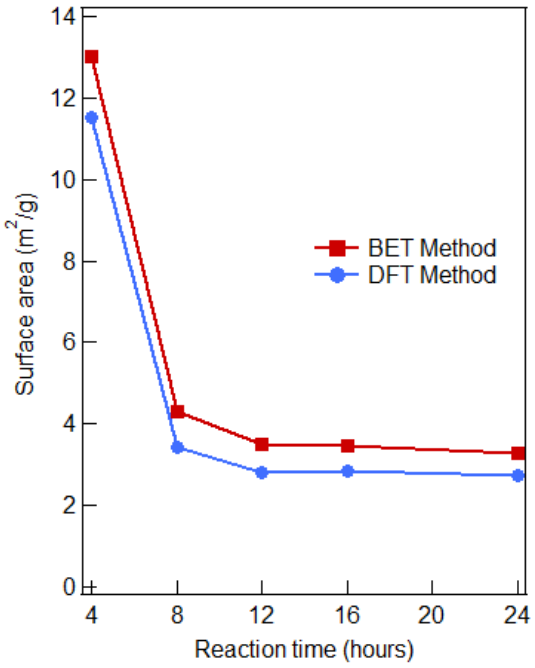

Figure 72. Surface Area of hydrothermal carbon plotted against the reaction time. The surface area is shown when calculated from the BET and DFT methods.

Table 11. Gas Sorption Surface Area Measurements and literature values for comparison. Unless stated otherwise, nitrogen gas was used for the measurement.

Type	Char Sampled	Sample Mass (g)	BET Method [m^2/g]	DFT Method [m^2/g]	DR Method [m^2/g]	Lit. Ref.
4hg-HTC	4/22 HTC	0.1685	13.03	11.531		
8hg	6/06 HTC	0.7481	4.287	3.445		
8hg	10/25 HTC					
12hg	05/30 HTC	0.6046	3.518	2.801		
16hg	10/13 HTC	0.8304	3.467	2.826		
24hg	9/14 HTC	0.8713	3.274	2.732		
HTC: Feed: Glucose Conc. 50g/L, T= 180°C, t=4hrs			<1			99
HTC: Feed: Glucose, C0= 0.3 Molar, T=190C, t=4hrs			13.9			66
HTC: Feed: walnut shell, sunflower stem, olive stone. Conc. 50g/L, T=220 °C, t=22hrs Outgas T,t: 250 °C, 4hrs			31 27 22			100

AC	Picachem HP^{-1}20	0.3859			1454	
AC	Norit SX^{-1}	0.3469			811	
AC	Picachem HP^{-1}20				2130	101
AC	Norit SX^{-1}				922	102

Scanning Electron Microscopy

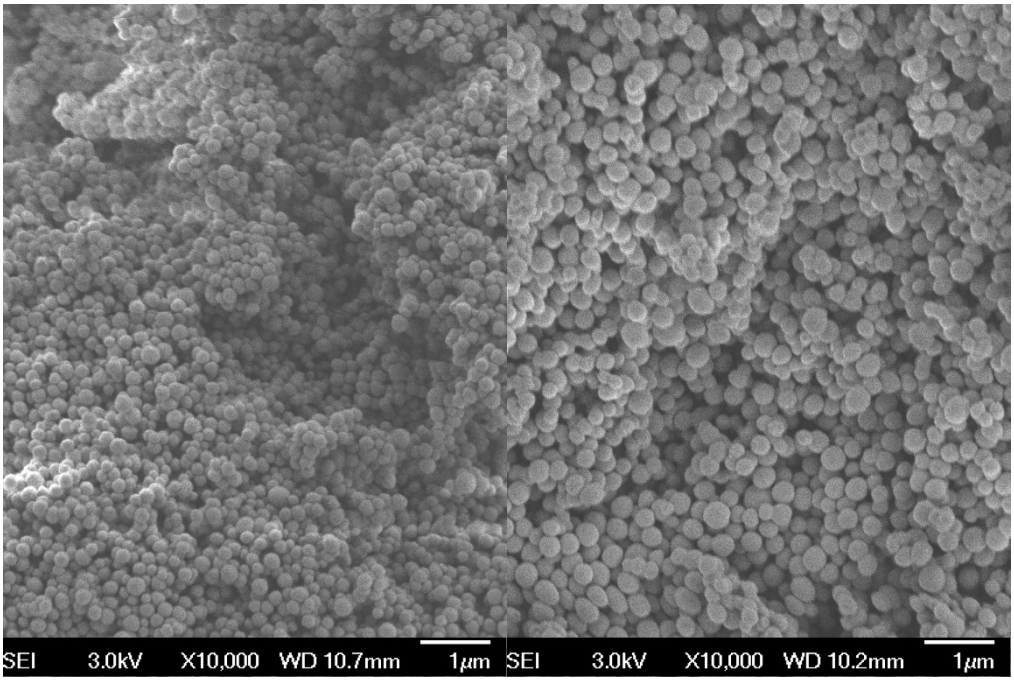

Figure 73. SEM image of a) 3-hour hydrochar b) 4-hour hydrochar.

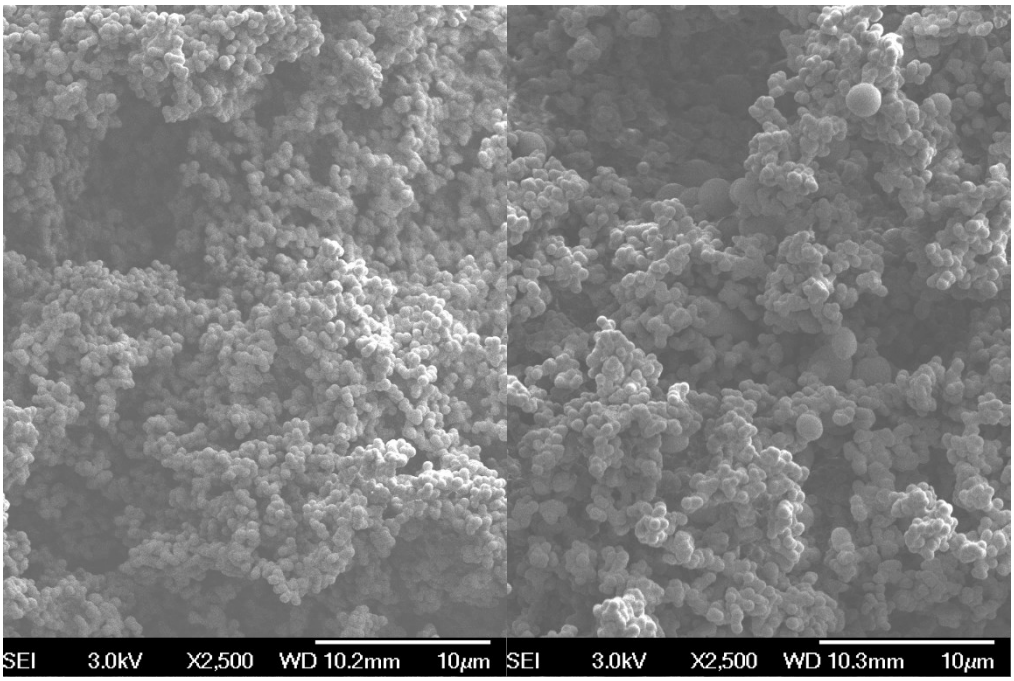

Figure 74. SEM image of a) 12-hour hydrochar b) 72-hour hydrochar.

Aerosol Mass Spectrometry

Fitting Procedure

The spectra is fit by the ion fragments from the ion table. At each m/z a combination of Gaussian type peaks are fit at their mass values in both the open and closed positions. These are subtracted against each other, giving the difference signal. This is shown in Figure 75, for the m/z=110 peak. The most prominent peak is $C_6H_6O_2$, followed by $C_2H_6O_5$, with much smaller peaks for $C_7H_{10}O$ and C_8H_{14}. Shown is the residual for the fit, which appears to be quite small.

The peak widths to fit the AMS spectra are determined by a line of best fit from peak widths measured for solo peaks. This is shown in Figure 76. At m/z=150, there is no overlap between the error bar and the fit line, indicating that high res fitting cannot be performed past m/z=150. In fact, the limit may be lower, at around m/z=120.

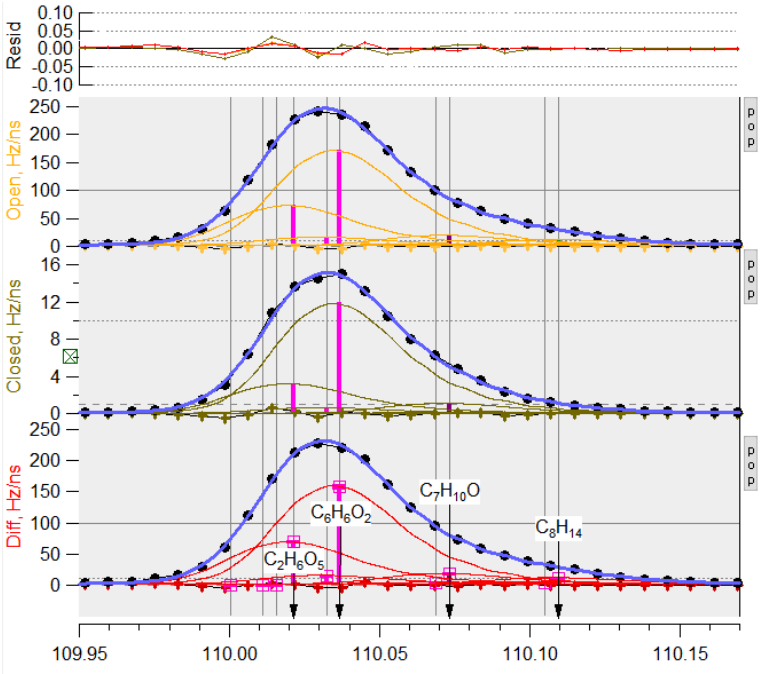

Figure 75. Fitting of AMS signal at m/z=110. The Closed signal is subtracted against the Open signal, giving the Difference (Diff) signal.

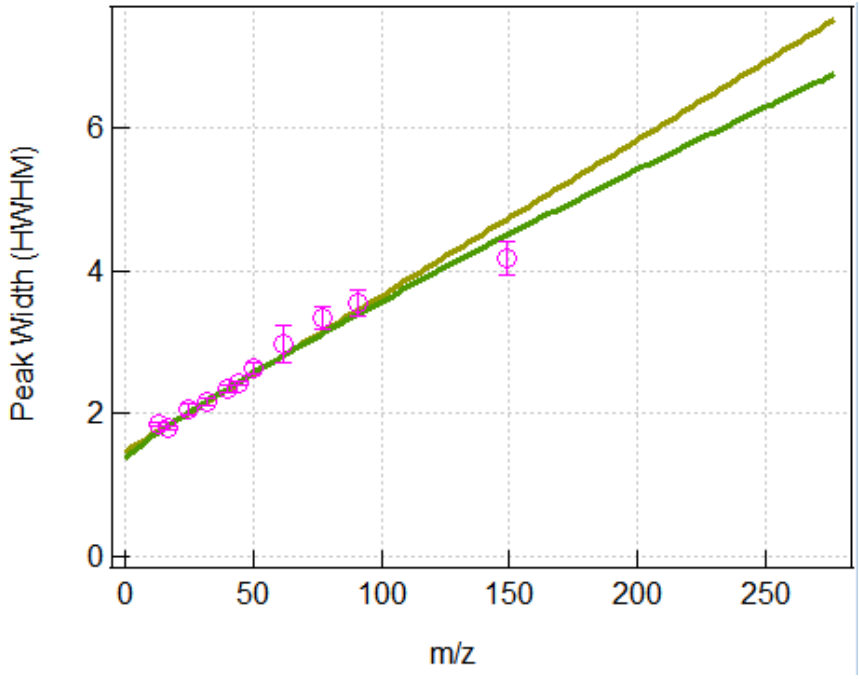

Figure 76. Peak width as a function of m/z. m/z was determined from isolated ions. The yellow line is the linear line of best fit to the data points, while the green curve is the quadratic line of best fit.

Residual Signals

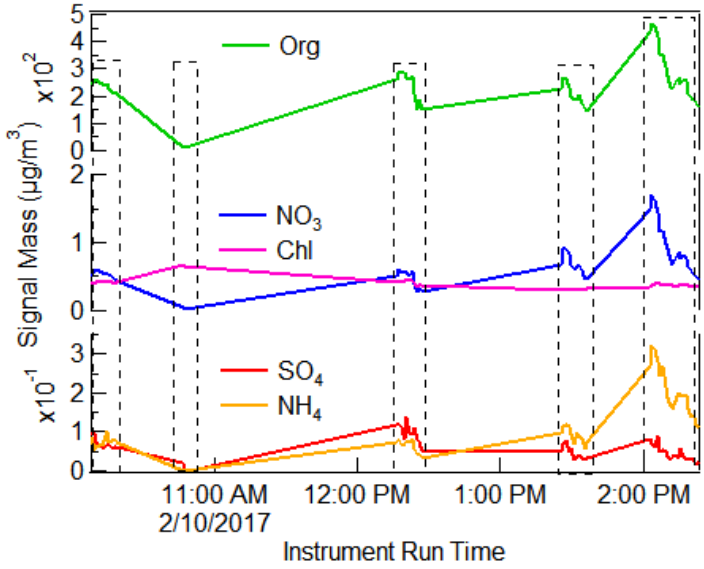

Figure 77. Sample AMS Ion Group Mass Loading during Run Time. Organic signal should be scaled by a factor of 100, while the sulfate and ammonia signals should be scaled by a factor of 0.1. Run on February 10th. Dashed sections indicate when instrument was collecting data.

The AMS instrument can quantify hundreds of mass signals, some occurring very near each other at the same AMU integer value. These signals primarily from the sample solid, but they can also come from trace impurities, such as any contaminant gases or residual solid in the system. The SP-AMS instrument, which is designed to quantitatively characterize atmospheric organic aerosols, arranges the mass signals into different groups, which may have more or less significance to each other depending on the nature of the particles being tested. For example, there is a signal associated with sulfate, which is a functionality seen in atmospheric organic aerosol particles, which combines the masses of atomic sulfur, SO, SO_2, etc. Again, such signals should be zero for the hydrochar, as the material was made using glucose and DI water, which do not contain any sulfur. These signals could be due to organic aerosols entrained in the system from previous use. The masses of these signals are shown in Figure 77. The NO_3 and Chlorine signals are about 2 orders of magnitude less than the Organic signal, and the SO_3 and NH_4 signals are an additional order of magnitude less significant than these. This indicates that the presence of non-hydrochar contaminants is

weak. The Chlorine signal is actually a misnomer for Argon, the carrier gas whose isotope values overlap with those of chlorine.

AMS Experiment Data and notes

AMS runs were performed on February 3rd, February 6th, February 10th, March 24th, March 31st, and April 19th. The sample loading system for purging the inlets and aerosolizing the hydrochar is operated by hand, and it was found that the amount of sample loaded in to the instrument widely varied. It was also found that the amount at times could make the software crash. It was suggested that the loading into the instrument (mass loading, or organic detected, in µg/m^3) should be in the range 200-800 µg/m^3. On the runs performed on April 19th, a strategy was implemented to give a more reliable mass loading, that was in the range of 20-100 µg/m^3, and that had an even mass loading with time.

Figure 78. AMS samples used for time trends. Given are the number of time points used, the minimum, maximum, and average mass loadings in µg/m^3.

Char Type	Char Batch	AMS Run	#Time Points	Avg (µg/m^3)	%Mass Cx	%Mass CH	%Mass CHO1	%Mass CHOgt1
3-hour	*	Apr20 t1	8	307.6	6.26%	39.28%	36.26%	18.20%
4-hour	9/27	Feb3 t2	31	167.8	10.57%	45.04%	34.64%	9.75%
12-hour	05/30	Apr20 t1-t4 Avg	27	213.3	9.66%	55.18%	23.12%	12.04%
16-hour	10/07	Apr20 t1	6	98.6	9.08%	53.78%	25.09%	12.05%
20-hour	*	Apr20 t1	6	405.9	9.20%	50.53%	27.87%	12.39%

Quantifying Uncertainty in AMS

To use the SP-AMS as a quantitative technique, it is necessary to identify and quantify the uncertainty present in the data. The mass loading varies significantly from run to run, and there is a mass range that is optimal for measuring the hydrochar. With low mass loadings, the effects of sample contamination from residual material could be more prominent. At high mass loadings, the channels could be saturated, meaning there is too much of a given ion for the reading to be accurate. The effects of cross-contamination are also uncertain, as non-negligible amounts of mass could be entrained in the 2-Liter volume, for example.

Table 12. Comparison of 12-hour hydrochar runs on Apr20. The number of runs, mass loading, composition of HO family, CO ion, CO_2 ion, and ion families Cx, CH, CHO1, and CHOgt1. The uncertainty is the confidence interval. The average of the four runs is included.

12hg 4/20 Runs	t1	t2	t3	t4	Avg
# Data Points	7	8	6	6	27
Total Mass Load Avg. (ug/m3)	50.4 ± 3.6	78.7 ± 4.0	745.5 ± 11.8	50.8 ± 4.2	231.4 ± 5.9
%HO family	30.4 ± 0.4	30.0 ± 0.4	35.3 ± 1.0	30.2 ± 0.3	31.5 ± 0.5
%CO	12.2 ± 0.1	12.0 ± 0.1	11.1 ± 0.1	12.0 ± 0.8	11.8 ± 0.3
$\%CO_2$	19.4 ± 0.2	18.6 ± 0.2	16.8 ± 0.4	19.6 ± 0.1	18.6 ± 0.2
Adjusted Tot. Mass Load Avg. (ug/m3)	19.2 ± 2.9	31.0 ± 3.7	273.5 ± 10.3	19.4 ± 3.0	85.7 ± 5.0
%Cx	9.5 ± 0.3	9.2 ± 0.2	10.3 ± 0.3	9.6 ± 0.3	9.7 ± 0.3
%CH	56.2 ± 0.3	55.6 ± 0.1	53.7 ± 0.2	54.8 ± 0.3	55.1 ± 0.2
%CHO1	22.2 ± 0.4	22.8 ± 0.2	24.1 ± 0.2	23.7 ± 0.2	23.2 ± 0.2
%CHOgt1	12.1 ± 0.2	12.3 ± 0.2	11.8 ± 0.1	11.9 ± 0.3	12.0 ± 0.2

Batch-to-batch Variability

Two different 12-hour hydrochar batches were run on the AMS to determine how sensitive the instrument is to the batch-to-batch variability, which was quantified by the Elemental Analysis and Raman spectroscopy methods. The 05/30 12-hour hydrochar batch was run on Apr20 on the AMS, while the 06/08 12-hour hydrochar batch was run on Feb10th on the AMS.

Table 13. AMS analysis of 12-hour hydrochar prepared from different batches. 12-hour hydrochar batch 06/08 was run on Feb10, while batch 05/30 was run on Apr20 with 4 trials, which were averaged together. The mass loading (total and adjusted total in ug/m3) are tabulated, along with the relative amounts of HO family ions, CO ion, and CO_2 ion, along with the significant ion families, Cx, CH, CHO1, and CHOgt1. Included are the confidence intervals.

	12hg 2/10 t1	12hg 4/20 t1-t4
# Data Points	10	27
Total Mass Load Avg. (ug/m3)	598.2 ± 17.5	231.4 ± 5.9
%HO family	13.0 ± 0.3	31.5 ± 0.5
%CO	42.6 ± 1.4	11.8 ± 0.3
%CO_2	8.5 ± 0.3	18.6 ± 0.2
Adjusted Tot. Mass Load Avg. (ug/m3)	214.1 ± 6.0	85.7 ± 5.0
%Cx	13.9 ± 0.2	9.7 ± 0.3
%CH	57.8 ± 0.1	55.1 ± 0.2

%CHO1	21.9 ± 0.1	23.2 ± 0.2
%CHOgt1	6.4 ± 0.1	12.0 ± 0.2

Bibliography

1. Huaman, R. N. E., and Tian Xiu Jun, Energy related CO 2 emissions and the progress on CCS projects: a review. *Renewable and Sustainable Energy Reviews* **2014,** *31*, 368-385.
2. Rosenzweig, C., David Karoly, Marta Vicarelli, Peter Neofotis, Qigang Wu, Gino Casassa, Annette Menzel et al., Attributing physical and biological impacts to anthropogenic climate change. *Nature* **2008,** *453* (7193), 353-357.
3. Comar, C. L., and L. A. Sagan, Health effects of energy production and conversion. *Annual Review of Energy* **1976,** *1* (1), 581-600.
4. Thornton, P. K., Polly J. Ericksen, Mario Herrero, and Andrew J. Challinor, Climate variability and vulnerability to climate change: a review. *Global change biology* **2014,** *20* (11), 3313-3328.
5. Renzoni, A., F. Zino, and E. Franchi, Mercury levels along the food chain and risk for exposed populations. *Environmental Research* **1998,** *77* (2), 68-72.
6. Markey, C. M., Macall A. Coombs, Carlos Sonnenschein, and Ana M. Soto, Mammalian development in a changing environment: exposure to endocrine disruptors reveals the developmental plasticity of steroid-hormone target organs. *Evolution & development* **2003,** *5* (1), 67-75.
7. Okedeyi, O. O., Simiso Dube, Omotayo R. Awofolu, and Mathew M. Nindi, Assessing the enrichment of heavy metals in surface soil and plant (Digitaria eriantha) around coal-fired power plants in South Africa. *Environmental Science and Pollution Research* **2014,** *21* (6), 4686-4696.
8. Al Zarooni, M., and Walid Elshorbagy, Characterization and assessment of Al Ruwais refinery wastewater. *Journal of hazardous materials* **2006,** *136* (3), 398-405.
9. Oliveira, D. P., Patricia A. Carneiro, Maureen K. Sakagami, Maria Valnice B. Zanoni, and Gisela A. Umbuzeiro, Chemical characterization of a dye processing plant effluent—identification of the mutagenic components. *Mutation Research/Genetic Toxicology and Environmental Mutagenesis* **2007,** *626* (1), 135-142.
10. George, C., Marcel Wagner, Martin Kücke, and Matthias C. Rillig, Divergent consequences of hydrochar in the plant–soil system: arbuscular mycorrhiza, nodulation, plant growth and soil aggregation effects. *Applied Soil Ecology* **2012,** *59*, 68-72.
11. Trent, V. A., Chemical analyses and physical properties of 12 coal samples from the Pocahontas field, Tazewell County, Virginia, and McDowell County, West Virginia. *US Geol. Surv., Bull.;(United States)* **1982,** *1528*.
12. Samanta, S. K., Om V. Singh, and Rakesh K. Jain, Polycyclic aromatic hydrocarbons: environmental pollution and bioremediation. *TRENDS in Biotechnology* **2002,** *20* (6), 243-248.
13. Kropp, K. G., and Phillip M. Fedorak, A review of the occurrence, toxicity, and biodegradation of condensed thiophenes found in petroleum. *Canadian journal of microbiology* **1998,** *44* (7), 605-622.
14. Ahmad Khan, H., Short Review: Benzene's toxicity: a consolidated short review of human and animal studies. *Human & experimental toxicology* **2007,** *26* (9), 677-685.
15. Litman, T., Transportation cost and benefit analysis. *Victoria Transport Policy Institute* **2009,** *31*.
16. Worrell, E., Lenny Bernstein, Joyashree Roy, Lynn Price, and Jochen Harnisch, Industrial energy efficiency and climate change mitigation. *Energy efficiency* **2009,** *2* (2).
17. Marafi, M., and A. Stanislaus, Spent catalyst waste management: A review: Part I—Developments in hydroprocessing catalyst waste reduction and use. *Resources, Conservation and Recycling* **2008,** *52* (6), 859-873.
18. Sevilla, M., and Antonio B. Fuertes, Chemical and structural properties of carbonaceous products obtained by hydrothermal carbonization of saccharides. *Chemistry–A European Journal* **2009,** *15* (16), 4195-4203.

19. Funke, A., and Felix Ziegler, Hydrothermal carbonization of biomass: a summary and discussion of chemical mechanisms for process engineering. *Biofuels, Bioproducts and Biorefining* **2010,** *4* (2), 160-177.
20. Liu, Z., Augustine Quek, S. Kent Hoekman, and R. Balasubramanian, Production of solid biochar fuel from waste biomass by hydrothermal carbonization. *Fuel* **2013,** *103*, 943-949.
21. Kruse, A., Axel Funke, and Maria-Magdalena Titirici, Hydrothermal conversion of biomass to fuels and energetic materials. *Current opinion in chemical biology* **2013,** *17* (3), 515-521.
22. Bargmann, I., Matthias C. Rillig, Andrea Kruse, Jörg-Michael Greef, and Martin Kücke, Effects of hydrochar application on the dynamics of soluble nitrogen in soils and on plant availability. *Journal of plant nutrition and soil science* **2014,** *177* (1), 48-58.
23. Demir-Cakan, R., Niki Baccile, Markus Antonietti, and Maria-Magdalena Titirici, Carboxylate-rich carbonaceous materials via one-step hydrothermal carbonization of glucose in the presence of acrylic acid. *Chemistry of Materials* **2009,** *21* (3), 484-490.
24. Chen, Z., Lijian Ma, Shuqiong Li, Junxia Geng, Qiang Song, Jun Liu, Chunli Wang et al, Simple approach to carboxyl-rich materials through low-temperature heat treatment of hydrothermal carbon in air. *Applied Surface Science* **2011,** *257* (20), 8686-8691.
25. Wu, Z. L., Pu Zhang, Ming Xuan Gao, Chun Fang Liu, Wei Wang, Fei Leng, and Cheng Zhi Huang, One-pot hydrothermal synthesis of highly luminescent nitrogen-doped amphoteric carbon dots for bioimaging from Bombyx mori silk–natural proteins. *Journal of Materials Chemistry B* **2013,** *1* (22), 2868-2873.
26. Ding, L., Zichen Wang, Yannan Li, Yalei Du, Hequn Liu, and Yupeng Guo, A novel hydrochar and nickel composite for the electrochemical supercapacitor electrode material. *Materials Letters* **2012,** *74*, 111-114.
27. Titirici, M.-M., Markus Antonietti, and Arne Thomas, A generalized synthesis of metal oxide hollow spheres using a hydrothermal approach. *Chemistry of Materials* **2006,** *18* (16), 3808-3812.
28. Sevilla, M., Antonio B. Fuertes, and Robert Mokaya, High density hydrogen storage in superactivated carbons from hydrothermally carbonized renewable organic materials. *Energy & Environmental Science* **2011,** *4* (4), 1400-1410.
29. Cakan, R. D., Maria-Magdalena Titirici, Markus Antonietti, Guanglei Cui, Joachim Maier, and Yong-Sheng Hu, Hydrothermal carbon spheres containing silicon nanoparticles: synthesis and lithium storage performance. *Chemical Communications* **2008,** *32*, 3759-3761.
30. Gao, F., Guanghua Shao, Jiangying Qu, Siyuan Lv, Yuqian Li, and Mingbo Wu, Tailoring of porous and nitrogen-rich carbons derived from hydrochar for high-performance supercapacitor electrodes. *Electrochimica Acta* **2015,** *155*, 201-208.
31. Sevilla, M., W. Gu, C. Falco, María-Magdalena Titirici, A. B. Fuertes, and G. Yushin, Hydrothermal synthesis of microalgae-derived microporous carbons for electrochemical capacitors. *Journal of Power Sources* **2014,** *267*, 26-32.
32. Baccile, N., Guillaume Laurent, Florence Babonneau, Franck Fayon, Maria-Magdalena Titirici, and Markus Antonietti, Structural characterization of hydrothermal carbon spheres by advanced solid-state MAS 13C NMR investigations. *The Journal of Physical Chemistry C* **2009,** *113* (22), 9644-9654.
33. Elaigwu, S. E., and Gillian M. Greenway, Chemical, structural and energy properties of hydrochars from microwave-assisted hydrothermal carbonization of glucose. *International Journal of Industrial Chemistry* **2016,** *7* (4), 449-456.
34. Kuster, B. F., and Hessel S. van der Baan, The influence of the initial and catalyst concentrations on the dehydration of D-fructose. *Carbohydrate research* **1977,** *54* (2), 165-176.
35. Kabyemela, B. M., Tadafumi Adschiri, Roberto M. Malaluan, and Kunio Arai, Glucose and fructose decomposition in subcritical and supercritical water: detailed reaction pathway, mechanisms, and kinetics. *Industrial & Engineering Chemistry Research* **1999,** *38* (8), 2888-2895.

36. Klingler, D., and H. Vogel, Influence of process parameters on the hydrothermal decomposition and oxidation of glucose in sub-and supercritical water. *The Journal of Supercritical Fluids* **2010,** *55* (1), 259-270.
37. Brown. Avery B., B. M., Geoffrey Tompsett, Russell Lewis, Nathaniel Deskins, and Michael Timko, Structural analysis of hydrothermal char and its models by density functional theory simulation of vibrational spectroscopy *Submitted to Carbon for Review*.
38. Ferrari, A. C., and Jf Robertson, Interpretation of Raman spectra of disordered and amorphous carbon. *Physical review B* **2000,** *61* (20).
39. O. Beyssac, B. G., J. P. Petitet, E. Froigneux, M. Moreau and J. N. Rouzaud,, On the characterization of disordered and heterogeneous carbonaceous materials by Raman spectroscopy. *Spectrochimica Acta Part A: Molecular and Biomolecular Spectroscopy* **2003,** *59* (10), 2267-2276.
40. Diakité, M., Andrea Paul, Christian Jäger, Judith Pielert, and Jan Mumme, Chemical and morphological changes in hydrochars derived from microcrystalline cellulose and investigated by chromatographic, spectroscopic and adsorption techniques. *Bioresource technology* **2013,** *150*, 98-105.
41. Chuntanapum, A., and Yukihiko Matsumura, Formation of tarry material from 5-HMF in subcritical and supercritical water. *Industrial & engineering chemistry research* **2009,** *48* (22), 9837-9846.
42. Li, X., Jun-ichiro Hayashi, and Chun-Zhu Li, FT-Raman spectroscopic study of the evolution of char structure during the pyrolysis of a Victorian brown coal. *Fuel* **2006,** *85* (12), 1700-1707.
43. Sadezky, A., Harald Muckenhuber, Hinrich Grothe, R. Niessner, and Ulrich Pöschl, Raman microspectroscopy of soot and related carbonaceous materials: spectral analysis and structural information. *Carbon* **2005,** *43* (8), 1731-1742.
44. Xiao, L.-P., Zheng-Jun Shi, Feng Xu, and Run-Cang Sun, Hydrothermal carbonization of lignocellulosic biomass. *Bioresource Technology* **2012,** *118*, 619-623.
45. Dinjus, E., Andrea Kruse, and Nicole Troeger, Hydrothermal carbonization–1. Influence of lignin in lignocelluloses. *Chemical engineering & technology* **2011,** *34* (12), 2037-2043.
46. Schuhmacher, J. P., F. J. Huntjens, and D. W. Van krevelen, Chemical structure and properties of coal. 26. Studies on artificial coalification. *Fuel* **1960,** *39* (3), 223-234.
47. Onasch, T. B., A. Trimborn, E. C. Fortner, J. T. Jayne, G. L. Kok, L. R. Williams, P. Davidovits, and D. R. Worsnop, Soot particle aerosol mass spectrometer: development, validation, and initial application. *Aerosol Science and Technology* **2012,** *46* (7), 804-817.
48. Román, S., J. M. V. Nabais, Carlos Laginhas, Beatriz Ledesma, and J. F. González, Hydrothermal carbonization as an effective way of densifying the energy content of biomass. *Fuel Processing Technology* **2012,** *103*, 78-83.
49. Xu, Q., Qifeng Qian, Augustine Quek, Ning Ai, Ganning Zeng, and Jiawei Wang, Hydrothermal carbonization of macroalgae and the effects of experimental parameters on the properties of hydrochars. *ACS Sustainable Chemistry & Engineering* **2013,** *1* (9), 1092-1101.
50. Zhu, X., Yuchen Liu, Chao Zhou, Shicheng Zhang, and Jianmin Chen, Novel and high-performance magnetic carbon composite prepared from waste hydrochar for dye removal. *Sustainable Chemistry & Engineering* **2014,** *2* (4), 969-977.
51. Kang, S., Xianglan Li, Juan Fan, and Jie Chang, Characterization of hydrochars produced by hydrothermal carbonization of lignin, cellulose, D-xylose, and wood meal. *Industrial & engineering chemistry research* **2012,** *51* (26), 9023-9031.
52. Lu, X., Perry J. Pellechia, Joseph RV Flora, and Nicole D. Berge, Influence of reaction time and temperature on product formation and characteristics associated with the hydrothermal carbonization of cellulose. *Bioresource technology* **2013,** *138*, 180-190.
53. Liu, F., Ruidong Yu, and Minghui Guo, Hydrothermal carbonization of forestry residues: influence of reaction temperature on holocellulose-derived hydrochar properties. *Journal of Materials Science* **2017,** *52* (3), 1736-1746.

54. Sevilla, M., and Antonio B. Fuertes, The production of carbon materials by hydrothermal carbonization of cellulose. *Carbon* **2009,** *47* (9), 2281-2289.
55. Latham, K. G., G. Jambu, S. D. Joseph, and S. W. Donne, Nitrogen doping of hydrochars produced hydrothermal treatment of sucrose in H2O, H2SO4, and NaOH. *ACS Sustainable Chemistry & Engineering* **2014,** *2* (4), 755-764.
56. Muthuraman, M., Tomoaki Namioka, and Kunio Yoshikawa, Characteristics of co-combustion and kinetic study on hydrothermally treated municipal solid waste with different rank coals: a thermogravimetric analysis. *Applied Energy* **2010,** *87* (1), 141-148.
57. Lu, X., Beth Jordan, and Nicole D. Berge, Thermal conversion of municipal solid waste via hydrothermal carbonization: comparison of carbonization products to products from current waste management techniques. *Waste management* **2012,** *32* (7), 1353-1365.
58. Berge, N. D., Kyoung S. Ro, Jingdong Mao, Joseph RV Flora, Mark A. Chappell, and Sunyoung Bae, Hydrothermal carbonization of municipal waste streams. *Environmental science & technology* **2011,** *45* (13), 5696-5703.
59. Lynam, J. G., Charles J. Coronella, Wei Yan, Mohammad T. Reza, and Victor R. Vasquez, Acetic acid and lithium chloride effects on hydrothermal carbonization of lignocellulosic biomass. *Bioresource technology* **2011,** *102* (10), 6192-6199.
60. Han, L., Kyoung S. Ro, Ke Sun, Haoran Sun, Ziying Wang, Judy A. Libra, and Baoshan Xing, New Evidence for High Sorption Capacity of Hydrochar for Hydrophobic Organic Pollutants. *Environmental Science & Technology* **2016,** *50* (24), 13274-13282.
61. Zhang, H., Fayu Zhang, and Qing Huang, Highly effective removal of malachite green from aqueous solution by hydrochar derived from phycocyanin-extracted algal bloom residues through hydrothermal carbonization. *RSC Advances* **2017,** *7* (10), 5790-5799.
62. Steinbeiss, S., G. Gleixner, and M. Antonietti, Effect of biochar amendment on soil carbon balance and soil microbial activity. *Soil Biology and Biochemistry* **2009,** *41* (6), 1301-1310.
63. Titirici, M.-M., and Markus Antonietti, Chemistry and materials options of sustainable carbon materials made by hydrothermal carbonization. *Chemical Society Reviews* **2010,** *39* (1), 103-116.
64. Timko, M. T., Alex R. Maag, Juan Mauricio Venegas, Brendan McKeogh, Zhengyang Yang, Geoffrey A. Tompsett, Simón Escapa, Joseph Toto, Erin Heckley, and Frederick T. Greenaway, Spectroscopic tracking of mechanochemical reactivity and modification of a hydrothermal char. *RSC Advances* **2016,** *6* (15), 12021-12031.
65. Guiotoku, M., Fabricio Augusto Hansel, Etelvino Henrique Novotny, and Claudia Maria Branco de Freitas Maia, Molecular and morphological characterization of hydrochar produced by microwave-assisted hydrothermal carbonization of cellulose. *Pesquisa Agropecuária Brasileira* **2012,** *47* (5), 687-692.
66. Li, M., Wei Li, and Shouxin Liu, Hydrothermal synthesis, characterization, and KOH activation of carbon spheres from glucose. *Carbohydrate research* **2011,** *346* (8), 999-1004.
67. Srokol, Z., Anne-Gaëlle Bouche, Anton van Estrik, Rob CJ Strik, Thomas Maschmeyer, and Joop A. Peters, Hydrothermal upgrading of biomass to biofuel; studies on some monosaccharide model compounds. *Carbohydrate Research* **2004,** *339* (10), 1717-1726.
68. Kuster, B. F., and Herman MG Temmink, The influence of pH and weak-acid anions on the dehydration of D-fructose. *Carbohydrate research* **1977,** *54* (2), 185-191.
69. Patil, S. K., and Carl RF Lund, Formation and growth of humins via aldol addition and condensation during acid-catalyzed conversion of 5-hydroxymethylfurfural. *Energy & Fuels* **2011,** *25* (10), 4745-4755.
70. Horvat, J., Branimir Klaić, Biserka Metelko, and Vitomir Šunjić, Mechanism of Levulinic Acid Formation in Acid Catalysed Hydrolysis of 2-Hydroxymethylfurane and 5-Hydroxymethylfurane-2-carhaldehyde. *Croatica Chemica Acta* **1986,** *59* (2), 429-438.

71. Karwa, S., Varun M. Gajiwala, Jacob Heltzel, Sushil KR Patil, and Carl RF Lund, Reactivity of levulinic acid during aqueous, acid-catalyzed HMF hydration. *Catalysis Today* **2016,** *263*, 16-21.
72. Promdej, C., and Yukihiko Matsumura, Temperature effect on hydrothermal decomposition of glucose in sub-and supercritical water. *Industrial & Engineering Chemistry Research* **2011,** *50* (14), 8492-8497.
73. Nagamori, M., and Toshitaka Funazukuri, Glucose production by hydrolysis of starch under hydrothermal conditions. *Journal of chemical technology and biotechnology* **2004,** *79* (3), 229-233.
74. Barbier, J., Nadège Charon, Nathalie Dupassieux, Anne Loppinet-Serani, Laure Mahé, Jérémie Ponthus, Marion Courtiade, Annie Ducrozet, Agnès Fonverne, and François Cansell, Hydrothermal conversion of glucose in a batch reactor. A detailed study of an experimental key-parameter: The heating time. *The Journal of Supercritical Fluids* **2011,** *58* (1), 114-120.
75. Naisse, C., Marie Alexis, Alain Plante, Katja Wiedner, Bruno Glaser, Alessandro Pozzi, Christopher Carcaillet, Irene Criscuoli, and Cornélia Rumpel, Can biochar and hydrochar stability be assessed with chemical methods? *Organic geochemistry* **2013,** *60*, 40-44.
76. Latham, K. G., Michela I. Simone, Wesley M. Dose, Jessica A. Allen, and Scott W. Donne, Synchrotron based NEXAFS study on nitrogen doped hydrothermal carbon: Insights into surface functionalities and formation mechanisms. *Carbon* **2017,** *114*, 566-578.
77. Falco, C., Fernando Perez Caballero, Florence Babonneau, Christel Gervais, Guillaume Laurent, Maria-Magdalena Titirici, and Niki Baccile, Hydrothermal carbon from biomass: structural differences between hydrothermal and pyrolyzed carbons via 13C solid state NMR. *Langmuir* **2011,** *27* (23), 14460-14471.
78. Falco, C., Niki Baccile, and Maria-Magdalena Titirici, Morphological and structural differences between glucose, cellulose and lignocellulosic biomass derived hydrothermal carbons. *Green Chemistry* **2011,** *13* (11), 3273-3281.
79. Wilson, E. B., John Courtney Decius, and Paul C. Cross, *Molecular vibrations: the theory of infrared and Raman vibrational spectra*. Courier Corporation: 2012.
80. El-Bassoussi, A. A., M. H. M. Ahmed, SM El Sayed, J. S. Basta, and E-SK Attia, Characterization of some local petroleum residues by spectroscopic techniques. *Petroleum Science and Technology* **2010,** *28* (5), 430-444.
81. Schwanninger, M., J. C. Rodrigues, H. Pereira, and B. Hinterstoisser, Effects of short-time vibratory ball milling on the shape of FT-IR spectra of wood and cellulose. *Vibrational Spectroscopy* **2004,** *36* (1), 23-40.
82. van Zandvoort, I., Yuehu Wang, Carolus B. Rasrendra, Ernst RH van Eck, Pieter CA Bruijnincx, Hero J. Heeres, and Bert M. Weckhuysen, Formation, molecular structure, and morphology of humins in biomass conversion: influence of feedstock and processing conditions. *ChemSusChem* **2013,** *6* (9), 1745-1758.
83. van Zandvoort, I., Eline J. Koers, Markus Weingarth, Pieter CA Bruijnincx, Marc Baldus, and Bert M. Weckhuysen, Structural characterization of 13 C-enriched humins and alkali-treated 13 C humins by 2D solid-state NMR. *Green Chemistry* **2015,** *17* (8), 4383-4392.
84. Patil, S. K., Jacob Heltzel, and Carl RF Lund, Comparison of structural features of humins formed catalytically from glucose, fructose, and 5-hydroxymethylfurfuraldehyde. *Energy & Fuels* **2012,** *26* (8), 5281-5293.
85. Ishimaru, K., Toshimitsu Hata, Paul Bronsveld, Dietrich Meier, and Yuji Imamura, Spectroscopic analysis of carbonization behavior of wood, cellulose and lignin. *Journal of materials science* **2007,** *42* (1), 122-129.
86. Ferraro, J. R., K. Nakamoto, and Chris W. Brown, *Introductory raman spectroscopy*. Second Edition ed.; Academic Press: 2003.

87. Meuzelaar, H. L., Jacek P. Dworzanski, Neil S. Arnold, William H. McClennen, and David J. Wager, Advances in field-portable mobile GC/MS instrumentation. *Field Analytical Chemistry & Technology* **2000,** *4* (1), 3-13.
88. McLafferty, F. W. T., František, *Interpretation of Mass Spectra*. 4th Edition ed.; University Science Books: 1993.
89. Canagaratna, M. R., J. T. Jayne, J. L. Jimenez, J. D. Allan, M. R. Alfarra, Qi Zhang, T. B. Onasch et al, Chemical and microphysical characterization of ambient aerosols with the aerodyne aerosol mass spectrometer. *Mass Spectrometry Reviews* **2007,** *26* (2), 185-222.
90. Willis, M. D., A. K. Y. Lee, T. B. Onasch, E. C. Fortner, L. R. Williams, A. T. Lambe, D. R. Worsnop, and J. P. D. Abbatt, Collection efficiency of the soot-particle aerosol mass spectrometer (SP-AMS) for internally mixed particulate black carbon. *Atmospheric Measurement Techniques* **2014,** *7* (12), 4507-4516.
91. Meier, R. J., On art and science in curve-fitting vibrational spectra. *Vibrational spectroscopy* **2005,** *39* (2), 266-269.
92. Socrates, G., *Infrared and Raman characteristic group frequencies: tables and charts*. 2004.
93. Fuertes, A. B., M. Camps Arbestain, M. Sevilla, Juan Antonio Maciá-Agulló, S. Fiol, R. López, R. J. Smernik, W. P. Aitkenhead, F. Arce, and Felipe Macìas, Chemical and structural properties of carbonaceous products obtained by pyrolysis and hydrothermal carbonisation of corn stover. *Soil Research* **2010,** *48* (7), 618-626.
94. Bradley, M., Curve fitting in Raman and IR spectroscopy: basic theory of line shapes and applications. Thermo Fisher Scientific: 2007.
95. Corbin, J. C., B. Sierau, M. Gysel, M. Laborde, A. Keller, Jin Kim, Andreas Petzold, T. B. Onasch, Ulrike Lohmann, and A. A. Mensah, Mass spectrometry of refractory black carbon particles from six sources: carbon-cluster and oxygenated ions. *Atmospheric Chemistry and Physics* **2014,** *14* (5), 2591-2603.
96. S.E. Stein, d., Mass Spectra. In *NIST Chemistry WebBook, NIST Standard Reference Database Number 69*, National Institute of Standards and Technology, Gaithersburg MD, 20899: (retrieved June 2017).
97. Yu, L., Camillo Falco, Jens Weber, Robin J. White, Jane Y. Howe, and Maria-Magdalena Titirici, Carbohydrate-derived hydrothermal carbons: a thorough characterization study. *Langmuir* **2012,** *28* (33), 12373-12383.
98. Luijkx, G. C., Fred van Rantwijk, and Herman van Bekkum, Hydrothermal formation of 1, 2, 4-benzenetriol from 5-hydroxymethyl-2-furaldehyde and D-fructose. *Carbohydrate research* **1993,** *242*, 131-139.
99. Aydıncak, K., Tuğrul Yumak, Ali Sınağ, and Bekir Esen, Synthesis and characterization of carbonaceous materials from saccharides (glucose and lactose) and two waste biomasses by hydrothermal carbonization. *Industrial & Engineering Chemistry Research* **2012,** *51* (26), 9145-9152.
100. Roman, S., JM Valente Nabais, Beatriz Ledesma, J. F. González, Carlos Laginhas, and M. M. Titirici, Production of low-cost adsorbents with tunable surface chemistry by conjunction of hydrothermal carbonization and activation processes. *Microporous and Mesoporous Materials* **2013,** *165*, 127-133.
101. Timko, M. T., Jin An Wang, James Burgess, Peter Kracke, Lino Gonzalez, Cherno Jaye, and Daniel A. Fischer, Roles of surface chemistry and structural defects of activated carbons in the oxidative desulfurization of benzothiophenes. *Fuel* **2016,** *163*, 223-231.
102. Nijkamp, M. G., J. E. M. J. Raaymakers, A. J. Van Dillen, and K. P. De Jong, Hydrogen storage using physisorption–materials demands. *Applied Physics A: Materials Science & Processing* **2001,** *72* (5), 619-623.

Copyright Acknowledgments

"Reprinted from Carbon, 47/9, Sevilla, M. and Fuertes, A.B., The production of carbon materials by hydrothermal carbonization of cellulose, 2281-2289, Copyright (2009), with permission from Elsevier."

Reprinted (adapted) with permission from (Baccile, N., Laurent, G., Babonneau, F., Fayon, F., Titirici, M. M., & Antonietti, M. (2009). Structural characterization of hydrothermal carbon spheres by advanced solid-state MAS 13C NMR investigations. The Journal of Physical Chemistry C, 113(22), 9644-9654.). Copyright (2009) American Chemical Society.

Reprinted (adapted) with permission from (Chuntanapum, A., & Matsumura, Y. (2009). Formation of tarry material from 5-HMF in subcritical and supercritical water. *Industrial & engineering chemistry research*, *48*(22), 9837-9846.). Copyright (2009) American Chemical Society.

"Reprinted from Carbon, 114, Latham, K. G., Simone, M. I., Dose, W. M., Allen, J. A., & Donne, S. W. , Synchrotron based NEXAFS study on nitrogen doped hydrothermal carbon: Insights into surface functionalities and formation mechanisms, 566-578, Copyright (2017), with permission from Elsevier."

"Reprinted (figure) with permission from (Ferrari, A.C., & Robertson, J., Carbon, 61, 14095, 2000. Copyright (2000) by the American Physical Society."